Numerical solutions of steady axisymmetric potential flows

by

Alexander Doak MSc

A thesis submitted in conformity with the requirements

for the degree of Doctor of Philosophy

Department of Mathematics

Faculty of Mathematical & Physical Sciences

University College London

October, 2019

Disclaimer

I, Alexander Doak, confirm that the work presented in this thesis is my own. Where information has been derived from other sources, I confirm that this has been indicated in the thesis.

Signature ____________________

Date ____________________

Abstract

This thesis is primarily concerned with steady axisymmetric potential flow problems. The flows are characterised by an interface between two immiscible fluids that is unknown a priori. This difficulty is overcome by mapping the flow domains to a potential space, where the interface is fixed onto an isoline of the Stoke's streamfunction. A numerical finite difference scheme, attributed to Woods [94] and Jeppson [52], is then used. The thesis is organised as follows. In chapter 2, we discuss the basic equations used throughout the thesis. In chapter 3, we revisit the classical problem of two-dimensional plane bubbles. Novel two-dimensional solutions are also presented. In chapter 4, we compute axisymmetric Taylor bubbles, and discuss the solution selection procedure. Comparisons with the solution space of the two-dimensional Taylor bubble are made. In chapter 5, we compute travelling wave solutions on a ferrofluid jet. The surrounding fluid is non-magnetisable, and we compute solutions under both the assumption that this fluid is a passive gas, and that it is of equal density to that of the ferrofluid. In chapter 6, we discuss ways in which the models of this thesis could be extended in future work. Chapter 7 is a conclusion.

This thesis was completed under the supervision of ***Professor Jean-Marc Vanden-Broeck***.

Impact statement

The work in this thesis concerns potential flow models, a field of mathematics that dates back two hundred years. The models considered are primarily axisymmetric: buoyancy driven Taylor bubbles rising in a tube, and modifications to the classical Rayleigh-Plateau instability, using magnetic fields.

Over the course of the PhD the results found have been published in a variety of journals. The articles published are Doak and Vanden-Broeck [31], Doak and Vanden-Broeck [32], Doak and Vanden-Broeck [33], and Gao et al. [40]. As well as being published in peer-reviewed journals, the results have been presented at a variety of different conferences. These conferences were both based in the UK (BAMC Surrey 2017, BAMC St Andrews 2018), and abroad, including workshops in China (Sanya 2019) and Austria (Vienna, 2018). International workshops of this kind strengthen the connectivity of the global research communities. The numerical method used in this thesis can be applied to a variety of new problems, such as flow exiting a cylindrical pipe onto a flat plate, which we hope to investigate in the future. Furthermore, the results from the ferrofluid model in chapter 5 motivate new experiments, where it would be interesting to see additional parameter ranges tested.

The models in this thesis enjoy a variety of industrial applications. Taylor bubbles are naturally occurring phenomena in many two-phase flows. They play an important role in Strombolian eruption of volcanoes. Furthermore, they have applications in the energy industry, where they occur in nuclear cooling systems, and in both refining and extracting oil and gas (they can cause blockage in extraction and transportation, with reported losses as high as 50%). The understanding of this phenomena helps develop practical methods to remove this inefficiency, for example through the use of slug catchers.

Meanwhile, the stabilisation of liquid jets has important applications in printing and agricultural sprays, where it is desirable to create a stable column of fluid. On the other hand, varying the parameters of destabilisation (increasing or decreasing the wavenumber of the dominant unstable mode) allows one to vary droplet size in a droplet generator. Furthermore, in experimental fluid dynamics, it can sometimes be difficult to vary physical parameters such as surface tension. One can instead electrify a conductor or alternatively magnetise a ferrofluid, in order to consider flow regimes in different parameter spaces and with different stability properties. Further understanding of the mathematical approximations of physical processes is key to both industrial and experimental development.

Acknowledgments

First, I would like to thank Professor Jean-Marc Vanden-Broeck for his tutorship, support, and friendship over the past 5 years.

I also must thank Dr Tao Gao, who consistently injects enthusiasm into both my own research and collaborative projects.

I am also indebted to Professor Zhan Wang, who hosted me during a research trip to Beijing.

This project would not have been possible without my parents and sister, whose patience and kindness still surpasses expectation.

Finally, my thanks to Phil, Richard, Emma, Chris, Hannah, George, Gabriel, Cressida, Daniel, Lorna, and Rachel, for their support through the highs and lows, to the UCL maths department, the KLB collective, and everyone who has helped shape the last four years.

Alexander Doak, *University College London*, October 2019

To my family

Contents

List of Tables

List of Figures

Chapter 1

Introduction

Potential flow theory concerns fluid flows in which the vector field $\boldsymbol{u}$ can be expressed as the gradient of a scalar potential, ϕ, called the velocity potential. Such a representation of the velocity field exists under the assumption that the flow is irrotational. Kelvin's circulation theorem states that a velocity field of an inviscid and barotropic fluid which is initially irrotational remains irrotational for all time. Hence, like the contents of this thesis, much of potential flow theory concerns incompressible flow of inviscid fluids, although such assumptions are not required for the existence of ϕ. For the sake of convenience, we will refer to problems which include the above three assumptions as 'potential flow'.

All the models considered in this thesis also fall into the category of 'interfacial flows'. These problems consider the flow of two immiscible fluids, between which there exists an infinitesimally thin boundary. This boundary is unknown a priori, must be found as part of the solution, and may move for time dependent models. Because the interface is an additional unknown, as well as a standard kinematic boundary condition on the interface, we also require a dynamic boundary condition. For potential flow, this condition is a continuity of pressure, evaluated using Bernoulli's equation. When the density of one of the fluids is deemed negligible, it is the case that the hydrodynamics in the denser fluid decouples from that of the lighter fluid. Models in which such assumptions are made are referred to in the literature as free surface problems.

Early breakthroughs on free surface potential flows concerned two-dimensional steady models, in which all external forces and surface tension are ignored. Such flows are referred to as free streamline problems. The constant pressure condition implies the magnitude of the velocity is constant along the free streamline. The additional assumption that the flow is two-dimensional allows the velocity field to be expressed in terms of a streamfunction ψ. The velocity potential and streamfunction are harmonic conjugates. These harmonic potentials lend themselves to the use of the powerful toolbox of complex analysis. Furthermore, if the flow is steady, the initially unknown free streamline is fixed to an equipotential of ψ. Hence, early works by Kirchhoff [54], Planck [69], Love [58], Zhukovsky [96], and Hopkinson [48], to name only a few, made use of hodograph transformations, conformal mapping techniques and reflection principles to solve (analytically) fully nonlinear problems.

When additional forces are included in the model (gravity and surface tension being common examples), the continuity of pressure condition has additional terms, denying the ability to use reflection principles. Early works considered perturbative expansions in small parameters, solving for the velocity potential ϕ as a function of displacement and time. Perhaps the most famous example is the theory of gravity waves, pioneered by Stokes [78]. An exact solution to capillary waves was later found by Crapper [23]. With the invention and subsequent increased accessibility of computers, a wealth of numerical treatments of two-dimensional free surface problems arose. Many of these methods made use of complex analysis. Series truncation methods, based upon conformal mappings and the power series representation of analytic functions, and boundary integral methods, which make use of Cauchy's integral formula, have been used to compute solutions for free surface and internal water waves, cavitating flows, rising bubbles, and so on. For a review, see Vanden-

Broeck [87].

The treatment of axisymmetric potential free surface flows is (in general) more difficult than that of two-dimensional problems. The assumption of axisymmetry means that the irrotationality of the velocity vector implies the existence of a Stokes streamfunction. Like the two-dimensional streamfunction, its isolines are everywhere tangential to the velocity vector. However, neither ψ nor ϕ are harmonic, and hence the mapping from the potential space (ϕ, ψ) to the physical space is no longer conformal. Despite this, the mapping is still useful since, for steady problems the free surface maps onto a line of constant ψ in the potential space. Woods [94] and then later Jeppson [52] derived the equations of motion for the radial coordinate r as a function of ϕ and ψ, and proposed a finite difference discretisation as a template to provide numerical solutions to steady axisymmetric potential flows. This formulation has since been used by a variety of authors to compute cavitating flow past a disk and sphere (Brennen [17]), a free streamline jet impacting a flat plate (Turenne and Fiset [79]), seepage through a homogeneous porous medium (Jeppson [51]) and contraction in a wind tunnel (Woods [94]). Furthermore, it has been used to numerically compute models related to this thesis, which are axisymmetric Taylor bubbles (Doak and Vanden-Broeck [32]), and axisymmetric capillary waves (Vanden-Broeck et al. [90]) in the presence of electric (Grandison et al. [44]) and magnetic (Blyth and Părău [13], Doak and Vanden-Broeck [33]) fields.

We begin by considering two-dimensional Taylor bubbles, often called plane bubbles. Plane bubbles are large bubbles which rise at a constant velocity through a denser medium, bounded by two parallel horizontal plates. The width of the bubble is almost that of the distance between the plates, such that a thin film forms down the side of the bubble. We consider bubbles whose length is much larger than its width, where it has been found that both the rise speed and the shape of the profile near the apex become independent of the length of the bubble (Collins [22]). This motivates an infinite model (a model where the bubble is taken to be infinitely long, avoiding mathematical difficulties of bubble closure and a turbulent wake). We are interested in a regime where viscosity and surface tension are negligible, such that the constant pressure condition on the interface becomes a balance between inertia and buoyancy. Garabedian [41] provided analytical evidence that, given a value of the channel width and gravity, the solution is not unique. Instead, one must also fix the velocity of the bubble, which can vary between zero and some critical value. This is contradictory to the experiments of Collins [22] and Maneri and Zuber [60], who found that, for sufficiently low viscosity and large bubble length, the non-dimensional rise velocity (given by the Froude number F, defined in chapter 2) is unique. Improving upon the work of Birkhoff and Carter [11], a numerical series truncation method performed by Vanden-Broeck [80] confirmed Garabedian's claim that there exists a family of solutions for F in a range between $(0, F_C)$, where F_C is a critical value. All the solutions considered up until this point are smooth, that is the interior angle at the apex of the bubble is 180^0. Vanden-Broeck also found that, for $F > F_C$, there exist a family of cusped bubbles, whose interior angle at the apex is zero. Such solutions have never been seen experimentally, and are considered nonphysical. It was also shown by Garabedian [42] and Modi [64] that it is possible there exists pointed plane bubbles, whose interior angle is given by 120^0. Vanden-Broeck [82] demonstrated that the $F = F_C$ bubble has such behaviour.

However, this is not the full story. Despite our interest in regimes with negligible surface tension, it is found that the inclusion of surface tension allows a unique smooth bubble in the range $F \in (0, F_C)$ to be selected. Vanden-Broeck [81] demonstrated that, for a fixed value of the non-dimensionalised surface tension (the inverse Weber number α^{-1}, defined in chapter 2), the angle at the apex of the bubble continually varies on the rise speed F. The infinite and continuous set of smooth bubbles $F \in (0, F_C)$ becomes an infinite discrete set $F \in \{F_1, F_2, F_3, \cdots\}$, where F_i is dependent upon α^{-1}. Furthermore, it is found that, as $\alpha^{-1} \to 0$, all the branches of smooth bubbles $F_i \to F^*$. Hence, a unique surface tension free smooth bubble has been selected by including surface tension, and taking the limit as it goes to zero. It is found that there is good agreement between F^* and the experimental value. This discussion is continued at greater length in chapter 3.

As well as plane bubbles, we also discuss a novel model of two-dimensional flow exiting a pipe onto a wedge. It is found that plane bubbles are a particular case of this formulation. This generalisation also extends to flows exiting a pipe onto a flat plate, a model which received a more recent numerical treatment based (also) upon series truncation methods by Christodoulides and Dias [21]. An improvement to the series used by Christodoulides and Dias is proposed, where an additional singularity, which was previously not considered, is removed.

In chapter 4, we consider axisymmetric Taylor bubbles. Figure 1.1 is a picture of an axisymmetric Taylor bubble taken from the paper by Davies & Taylor [26]. It is found that the solution space of axisymmetric Taylor bubbles has many similarities with the solution space of plane bubbles. We find that again there exists a critical value F_C, such that there exists a smooth surface tension free solution for $F \in (0, F_C)$. This is in agreement with the findings of Levine and Yang [57], who numerically solved a boundary integral formula based upon the Green's function method. As well as solutions with zero surface tension, Levine and Yang also computed solutions with surface tension. However, they only present results for F_1, the primary branch of smooth solutions with surface tension. We use the finite difference scheme of Woods [94] and Jeppson [51] to compute these solutions, as well as the higher order branches $F_2, F_3 \cdots$. These branches are found to be monotonically increasing functions of α^{-1}. Although we are unable to compute the branches for $\alpha^{-1} < 0.006$, we conjecture that all these branches approach a unique value F^* as $\alpha^{-1} \to 0$. We also compute the $F = F_C$ solution with zero surface tension. This bubble is a pointed bubble, with an

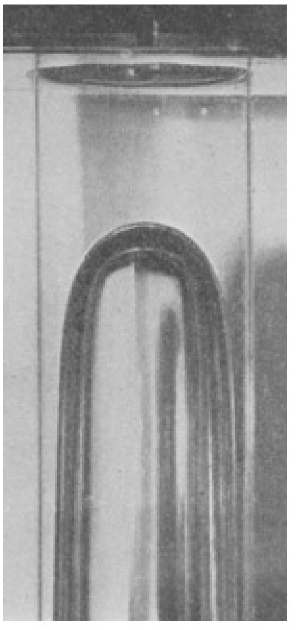

Figure 1.1: Figure 8 in Davies and Taylor [26].

interior angle of approximately 130^0. The local behaviour at the apex was derived by Garabedian [42]. It is worth noting that a similar finite difference scheme was used by Vanden-Broeck [83] to compute solutions with zero surface tension. However, this method failed to regulate the singularity at the apex of the bubble, and hence fails to converge upon mesh refinement. A suitable treatment of the singularity is presented in our numerical scheme. We also modify the finite difference scheme to compute plane bubbles. Good agreement with the results from chapter 3 provides a check on our numerical method.

Arguably the first axisymmetric free surface model was that of Rayleigh [73]. Rayleigh provided a mathematical explanation for the Plateau-Rayleigh instability (first shown experimentally by Plateau [70]), a capillary driven instability which causes axisymmetric columns of fluid to break into droplets. Experimental and theoretical work by Arkhipenko et al. [6] and Bashtovoi and Krakov [8] demonstrated that the azimuthal magnetic field induced by a current carrying wire could stabilise a column of ferrofluid coating the wire. Ferrofluids are synthetic fluids which exhibit superparamagnetic behaviour. This stabilisation allows for the existence of axisymmetric ferrohydrodynamic solitary waves, which were discovered in the more recent experiments of Bourdin et al. [15]. These experiments were motivated in part by the weakly nonlinear theory of Rannacher and Engel [72], who derived a Korteweg-de Vries (KdV) equation for the model. Fully nonlinear computations of solitary waves on a ferrofluid jet were then performed by Blyth and Părău [13], who made use of the finite difference scheme described above. However, all of the papers referenced above assume that the density of the surrounding fluid is negligible. In the experiments, to remove the effects of buoyancy, the ferrofluid is surrounded in a non-magnetisable fluid of equal density. We modify the numerical method to allow for the inclusion of the effect of the flow field in the surrounding fluid. A detailed discussion of the solution space for this model is described in chapter 5. Periodic, solitary and generalised solitary waves are computed.

The thesis is organised as follows. In chapter 2, we discuss the basic equations used in the models contained in the thesis. In chapter 3, we recompute plane bubble solutions, as well as flow exiting a pipe and hitting a wedge. In chapter 4, we compute axisymmetric Taylor bubbles. In chapter 5, we compute travelling wave solutions on a ferrofluid jet. Chapter 6 is a discussion about future work. Chapter 7 is a conclusion.

Chapter 2

Basics of fluid mechanics

2.1 Governing equations

In this project we consider irrotational flow of an incompressible and inviscid fluid. Incompressibility states that the density of the fluid, ρ, is constant, while inviscid states that the viscous coefficient, μ, is equal to zero. These assumptions are often made when considering the flow of water and other fluids of low viscosity. An inviscid incompressible flow is governed by the Euler equation,

$$\frac{D\boldsymbol{u}}{Dt} = -\frac{1}{\rho}\nabla p + \boldsymbol{F}, \tag{2.1}$$

where $\boldsymbol{u}$ is the velocity vector, ∇p is the pressure gradient, $\boldsymbol{F}$ is the external force per unit mass, and the operator $\frac{D}{Dt}$, commonly known as the material derivative, is defined as

$$\frac{D}{Dt} = \frac{\partial}{\partial t} + \boldsymbol{u} \cdot \nabla. \tag{2.2}$$

We will consider steady (time independent) models in two-dimensional Cartesian coordinates (x, y), and steady axisymmetric models in cylindrical polar coordinates (x, θ, r). Throughout this work, the external forces are conservative: in chapter 3 and 4, we consider gravity, while in chapter 5, we ignore gravity but consider magnetic forces. In general, we write $\boldsymbol{F} = \nabla L$.

Conservation of mass flux for an incompressible fluid gives rise to the continuity equation,

$$\nabla \cdot \boldsymbol{u} = 0. \tag{2.3}$$

As stated earlier, we also assume the flow to be irrotational, which states that

$$\nabla \times \boldsymbol{u} = \boldsymbol{0}. \tag{2.4}$$

Since $\boldsymbol{u}$ is a conservative vector field, we can write

$$\boldsymbol{u} = \nabla \phi, \tag{2.5}$$

for a scalar potential ϕ which we call the velocity potential of the flow. It follows from (2.3) that ϕ satisfies Laplace equation,

$$\nabla \cdot \boldsymbol{u} = 0 \implies \nabla \cdot (\nabla \phi) = \nabla^2 \phi = 0. \tag{2.6}$$

On walls and free surfaces, the kinematic boundary condition states that particles on the boundary remain on the boundary. For fixed walls, this reduces to the condition that the normal component of velocity on the boundary is equal to zero. Denoting $\widehat{\boldsymbol{n}}$ as the unit normal to the boundary, we find that

$$\boldsymbol{u} \cdot \widehat{\boldsymbol{n}} = 0. \tag{2.7}$$

For an interface given by $z = \eta(x, y, t)$, where (x, y, z) is some coordinate system, the condition takes the form

$$\frac{D(\eta - z)}{Dt} = 0.$$

2.1.1 Bernoulli equation

This thesis concerns problems referred to in literature as interfacial flows, a sub category of the larger field of free boundary problems. The models are characterised by a boundary between two immiscible fluids, which is unknown a priori and must be found as part of the solution. This requires an additional boundary condition, in this instance given by the Bernoulli equation. Following Batchelor [9], we substitute the vector identity

$$(\boldsymbol{u} \cdot \nabla)\boldsymbol{u} = \frac{1}{2}\nabla(\boldsymbol{u} \cdot \boldsymbol{u}) + (\nabla \times \boldsymbol{u}) \times \boldsymbol{u}$$

into (2.1), and using (2.4) we get

$$\frac{1}{2}\nabla\left(|\boldsymbol{u}|^2\right) = -\frac{1}{\rho}\nabla p + \nabla L.$$

Taking the pressure gradient and the gravitational force to one side and integrating gives

$$\frac{1}{2}\rho q^2 + p - \rho L = B, \tag{2.8}$$

where B is the Bernoulli constant, and $q = |\boldsymbol{u}|$. Consider two immiscible fluids, and denote the values of unknowns with a subscript 1 for the first fluid and a subscript 2 for the second fluid (i.e. fluid 2 has density ρ_2). Satisfying (2.8) on the interface in both fluids, one can show

$$\frac{1}{2}\left(q_1^2 - \rho q_2^2\right) + \frac{p_1 - p_2}{\rho_1} - (L_1 - \rho L_2) = B, \tag{2.9}$$

where $\rho = \rho_2/\rho_1$. We allow the velocities $\boldsymbol{u}_1$ and $\boldsymbol{u}_2$ to be different on the interface (resulting in a vortex sheet), but enforce continuity of pressure. Continuity of pressure is given by the Young-Laplace equation, which reads

$$p_1 - p_2 = T\kappa = T\left(\frac{1}{R_1} + \frac{1}{R_2}\right) \tag{2.10}$$

where T is the surface tension, κ is the mean curvature and R_1 and R_2 are the principal radii of curvature, counted positive when the centres of curvature lie inside fluid 1. Substituting equation (2.10) into (2.9) give us

$$\frac{1}{2}\left(q_1^2 - \rho q_2^2\right) + \frac{T}{\rho_1}\kappa - (L_1 - \rho L_2) = B, \tag{2.11}$$

When the density of the second fluid is negligible, we set $\rho_2 = 0$, drop the subscripts, and write

$$\frac{1}{2}q^2 + \frac{T}{\rho}\kappa - L = B. \tag{2.12}$$

2.1.2 Nondimensionalised Bernoulli equation

In all the chapters that follow, we will nondimensionalise the problem to reduce the number of variable free parameters. Consider the case when the second fluid has negligible density, and the external force $\boldsymbol{F}$ is taken to be gravity, acting in the x-direction ($L = gx$). Taking U as the reference velocity and H as the reference length, equation (2.12) becomes

$$\frac{1}{2}q^2 - \frac{1}{F^2}x + \frac{1}{\alpha}\kappa = \widetilde{B}. \tag{2.13}$$

where we have defined the two non-dimensional constants F (the Froude number) and α (the Weber number) as

$$F = \frac{U}{\sqrt{gH}}, \tag{2.14}$$

$$\alpha = \frac{\rho U^2 H}{T}. \tag{2.15}$$

2.2 Two-dimensional flow

Taking standard Cartesian coordinates (x, y, z), in two-dimensional flow we assume that the problem is invariant in the z direction. Hence, there are only two free spacial parameters, (x, y). We take $\boldsymbol{u} = (u, v)$ to be the velocity vector in (x, y). Equation (2.3) gives

$$u_x + v_y = 0, \tag{2.16}$$

where subscripts denote differentiation with respect to that variable. We see that this is automatically satisfied by a function ψ defined by

$$\psi_x = -v, \qquad \psi_y = u. \tag{2.17}$$

Here, ψ is the streamfunction. If we consider two points in the flow domain, A and B, we find that

$$\psi(B) = \psi(A) + \int_{\vec{AB}} u \, \mathrm{d}y \; - \; v \, \mathrm{d}x. \tag{2.18}$$

Hence, ψ is a path independent measure of flux in between two points. We see from equation (2.4) that ψ satisfies the Laplace equation. Furthermore, we have that

$$\psi_x = -\phi_y, \qquad \psi_y = \phi_x, \tag{2.19}$$

where ϕ, the velocity potential, is defined by $\nabla\phi = \boldsymbol{u}$. These are the Cauchy-Riemann equations. Therefore, the function

$$f = \phi + i\psi, \tag{2.20}$$

commonly referred to as the complex potential, is an analytic function of $z = x + iy$. This allows us to use a number of techniques from the theory of analytic functions. In particular, any analytic function $f(z)$ has its real and imaginary parts satisfy the

Laplace equation. Hence, it suffices to find an analytic function $f(z)$ that satisfies the given boundary conditions to solve these types of fluid problems.

Differentiating (2.20) with respect to z gives us the complex velocity, an analytic function of z given by

$$\frac{df}{dz} = \xi(z) = u(z) - iv(z). \tag{2.21}$$

2.2.1 Series truncation methods

Here we will briefly explain a process used to solve many two-dimensional free surface problems. The idea is to conformally map the flow from the f-plane to some auxiliary t-plane via an analytic function $f(t)$. By the f-plane, we mean the flow domain in the (ϕ, ψ) space. In the f-plane, the free surface is fixed onto a line $\psi =$ constant, in effect reducing the complexity of the problem by fixing the free surface to a known boundary. Generally, circles, semi-circles and quarter-circles are desirable geometries for the t plane. We then seek to find ξ as an analytic function of t, such that the relevant boundary conditions are satisfied. One would be tempted to write ξ as a power series in t, that is

$$\xi = \sum_{n=0}^{\infty} a_n t^n. \tag{2.22}$$

However, such a series will only converge if all leading order singularities have been removed for the desired radius of convergence (say we have mapped the flow domain onto the interior of the unit circle, then all the singularities for $t \leq 1$ must be removed). Hence, we instead write

$$\xi = G(t) \sum_{n=0}^{\infty} a_n t^n, \tag{2.23}$$

where $G(t)$ contains all the singularities of ξ. We then truncate the series after a finite number of terms, say N, and satisfy the relevant boundary conditions at various mesh-points on the boundary such that the number of unknowns matches the number of equations. This produces a system of M unknowns with M equations, which can be solved via Newton's method.

This procedure has been widely used for a large number of free surface flows. For an in depth review, see Vanden-Broeck [87].

2.3 Axisymmetric flow

An axisymmetric flow in cylindrical coordinates (x, θ, r) is a flow that is independent of θ (i.e. $\partial_\theta = 0$). We shall define the velocity vector $\boldsymbol{u}$ as

$$\boldsymbol{u} = (u, 0, v), \qquad \text{in } (x, \theta, r). \tag{2.24}$$

Therefore, the flow defined in three dimensions can again be reduced to a problem with two free spatial variables.

Analogous to the two-dimensional stream function, we wish to find a scalar function ψ whose gradient is normal to the direction of the velocity field. The Stokes stream function for axisymmetric flow is defined such that lines of constant ψ form streamtubes, that is $\nabla\psi \cdot \boldsymbol{u} = 0$. Taking $\boldsymbol{u} = \nabla \times (\psi/r)\widehat{\boldsymbol{e_\theta}}$ gives us the relations

$$\frac{\psi_x}{r} = -v \qquad \frac{\psi_r}{r} = u, \tag{2.25}$$

where $\widehat{\boldsymbol{e_\theta}}$ is the unit vector in the azimuthal direction. From this definition, we see that

$$\nabla\psi \cdot u = \psi_x u + \psi_r v = -ruv + ruv = 0, \tag{2.26}$$

which is the desired property of ψ. Notice that ψ automatically satisfies (2.3):

$$\nabla \cdot (u, 0, v) \quad = \quad \partial_x u + \frac{1}{r}\partial_r (rv),$$

$$= \partial_x \left(\frac{\psi_r}{r} \right) + \frac{1}{r} \partial_r \left(-\psi_x \right) = 0. \tag{2.27}$$

Furthermore, assuming the flow is steady, the kinematic boundary condition on fixed walls and free surfaces again reduces to $\psi =$ constant. If we consider two arbitrary points A and B in the flow domain, it follows from (2.25) that

$$\psi(B) = \psi(A) + \int_{\vec{\boldsymbol{AB}}} ru \, \mathrm{d}r \; - \; rv \, \mathrm{d}x. \tag{2.28}$$

Therefore, the difference in the values of the stream function between two points is the flux of fluid crossing a line connecting the two points divided by 2π. As with the two-dimensional stream function, this integral is path independent as $\boldsymbol{u}$ is a conservative field. Unlike the two-dimensional stream function (2.17), the axisymmetric stream function does not satisfy the Laplace equation. The θ component of (2.4) gives

$$u_r - v_x = 0 \implies \partial_r \left(\frac{1}{r} \frac{\partial \psi}{\partial r} \right) + \partial_z \left(\frac{1}{r} \frac{\partial \psi}{\partial x} \right) = 0 \implies \psi_{rr} - \frac{1}{r} \psi_r + \psi_{xx} = 0. \tag{2.29}$$

We need to find the curvature κ in the dynamic boundary condition (2.13). Parameterising the free surface as $r = \eta(x)$, we find

$$\kappa = \frac{1}{r(1 + \eta_x^2)^{1/2}} - \frac{\eta_{xx}}{(1 + \eta_x^2)^{3/2}}. \tag{2.30}$$

In the chapter to follow, we will discuss two-dimensional bubbles, called plane bubbles.

Chapter 3

Two-dimensional Taylor Bubbles

In the following two chapters, we will consider the classical problem of a long bubble rising in a tube. In this chapter, we will consider the problem in two-dimensional geometry, while in the following chapter we will consider the axisymmetric model. A three-dimensional visualization of both of these models is shown in figure 3.1.

3.1 Introduction

Since the experiments of Dumitrescu [34], it has been known that large volumes of air can rise steadily through a denser medium in the form of a finger-shaped bubble. This unchanging headform has a radius close to that of the tube, such that there is a thin jet of fluid around the outer edges of the finger. Such bubbles are often referred to as Taylor bubbles or slugs. Many authors have performed experiments on this type of flow, in both channel (i.e. two-dimensional) geometry (Collins [22]; Maneri and Zuber [60]), frequently referred to as plane bubbles, and axisymmetric geometry (most famously Davies and Taylor [26]; Zukoski [97], and for a review, Viana et al. [91]).

It has been found that the rise velocity U is independent of both the length of the bubble and viscous effects, under the condition that the Reynolds number Re, given

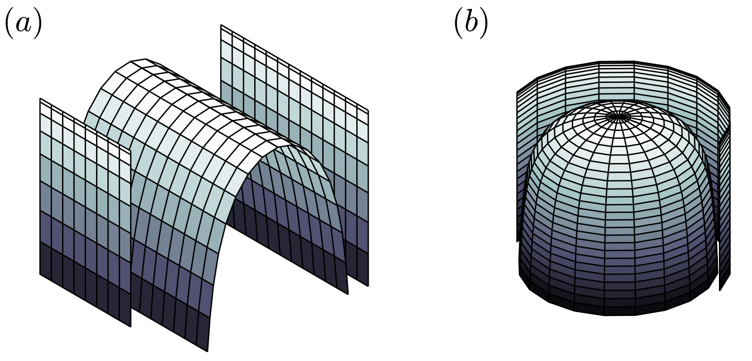

Figure 3.1: A three-dimensional visualization of a plane bubble (figure (a)) and an axisymmetric Taylor bubble (figure (b)) .

by $Re = \rho HU/\widehat{\mu}$, is sufficiently large ($Re > 200$). Here, ρ and $\widehat{\mu}$ are the density and dynamic viscosity of the fluid through which the bubble is travelling and H the tube radius. This justifies an inviscid and infinite model, in which we take the bubble to extend indefinitely down the tube. We take the density of air to be negligible compared to that of the heavier fluid, which we assume to be incompressible. Due to the inviscid nature of the problem, we consider the flow to be irrotational.

The problem is characterised by two dimensionless constants, the Froude number,

$$F = \frac{U}{\sqrt{gH}}, \tag{3.1}$$

and the Weber number

$$\alpha = \frac{U^2 H\rho}{T}, \tag{3.2}$$

where g is the acceleration of gravity, and T the surface tension.

In the following two chapters, we consider a regime characterised by negligible surface tension. It has been found in experiments that, for a given Weber number, the Froude number is uniquely determined. Therefore, one would hope that the mathematical model described in this chapter admits a unique solution F when surface tension is neglected. However, this is known not be the case. A unique zero surface tension solution cannot be obtained without the inclusion of surface tension

	$F < F_C$	$F = F_C$	$F > F_C$
μ	$\pi/2$	$2\pi/3$	π

Table 3.1: A table for the value of μ when $T = 0$.

in the equations. Below, we describe the solution space of the plane bubbles, and the solution selection procedure.

Plane bubbles have been the subject of many investigations, where most authors make use of conformal mapping techniques. Denoting μ as the angle between the central streamline and the free surface (see figure 3.2), we define *smooth* bubbles as those with $\mu = \pi/2$. Bubbles with $\mu = \pi$ are called *cusped* bubbles, while solutions with any other value of μ we refer to as *pointed* bubbles. In experiments, cusped and pointed bubbles are never seen, so such solutions are considered nonphysical. Garabedian [41] demonstrated analytically that, for $T = 0$, smooth plane bubble solutions are not uniquely defined in F, but instead there exists a continuum $F \in (0, F_C)$ for which such solutions exist. Using a heuristic energy argument, he claimed the only physically significant solution is the one given by $F = F_C$, and found that $F_C > 0.334$. Vanden-Broeck [80] later showed numerically that $F_C \approx 0.51$. He confirmed that all solutions with $F < F_C$ are smooth bubbles, and furthermore showed that solutions with $F > F_C$ are cusped bubbles. Modi [64] and Garabedian [42] both stated there could also exist zero surface tension pointed bubbles with $\mu = 2\pi/3$. Such a solution does exist, and was found by Vanden-Broeck [82], who showed that $F = F_C$ is the only value for which this is the case. Table 3.1 summarises the zero surface tension solution space.

Taking non-zero values of surface tension, Vanden-Broeck [81] found that, for any given value of α, there exists an infinite discrete set of smooth bubbles $F_1(\alpha), F_2(\alpha), \cdots$. These solutions are bounded above by $F^* \approx 0.318$, and it was found that as $\alpha^{-1} \to 0$, these solution branches collapsed to the value F^*. This mechanism by which a unique solution F^* to the $T = 0$ problem is found by including surface tension in the sys-

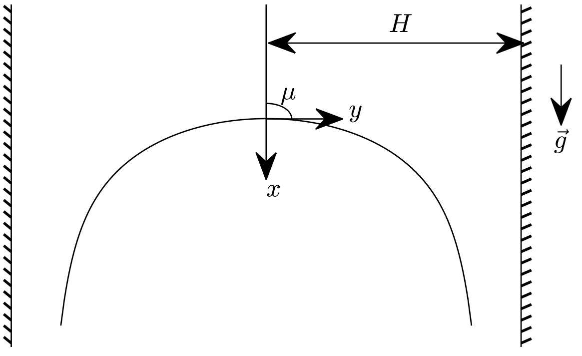

Figure 3.2: Configuration of a plane bubble.

tem, and then taking the limit as surface tension goes to zero, is called solution selection. A similar mechanism was used to select a unique solution for viscous Saffman-Taylor fingering (McLean and Saffman [61]). It is known to be associated with exponentially small terms in the surface tension (Vanden-Broeck [85]). This challenged Garabedian's claim that the physically significant solution was the $F = F_C$ solution. Collins [22] found that the experimental value for negligible surface tension is given by $F_e \approx 0.35$.

In this chapter, we will repeat the numerical method used by Vanden-Broeck [81], and recompute the known results above. This will be helpful in describing the solution space in the following chapter, where many qualitative similarities between the two-dimensional and axisymmetric problem are found. We also present a novel generalisation of the method to allow us to compute flows exiting a pipe onto a wedge with an interior angle $2(\pi - \beta)$. The flow configuration is shown in figure 3.3. This problem was considered in the case when the wedge is a flat plate ($\beta = \pi/2$) by Christodoulides and Dias [21]. When $\beta = \pi$, this problem is equivalent to that of the plane bubble, as shown in the following section.

3.2 Formulation

We will first consider the more general problem of flow from a pipe onto a wedge. We choose Cartesian coordinates, with x pointing in the direction of gravity, and the origin placed at the tip of the wedge. Flow comes in via a two-dimensional pipe of width $2H$ at $x \to -\infty$, where the fluid travels with constant velocity U in the positive x direction. We take H as the reference length and U the reference velocity. The flow separates where the pipe ends with separation angle μ. Below the pipe lies a wedge, placed such that the tip lies beneath the middle of the pipe. There exists a central streamline which meets the wedge at a stagnation point. The angle between the central streamline and the wedge is given by β, and the wedge is at a nondimensional distance W in the x-direction below the end of the pipe. The flow configuration is shown in figure 3.3.

We will assume the flow is incompressible and irrotational, and hence, following the discussions in section 2.2, we can write the velocity field in terms of two harmonic potentials, the velocity potential ϕ and the streamfunction ψ. Without loss of generality, we choose $\phi = 0$ at the tip of the wedge and $\psi = 0$ on the central streamline. We denote the velocity potential of ϕ at the separation point as ϕ_C. In our scaling, the wall at $y = 1$ and free surface are given by $\psi = 1$. We also define the complex potential $f = \phi + i\psi$. When solving this problem, we will conformally map the flow domain to some auxiliary t-plane with preferable geometry. Following the discussions in chapter 2, it will then suffice to find $\xi = u - iv$ as an analytic function of t, satisfying the relevant boundary conditions, where u and v are the x and y component of the velocity respectively.

The nondimensionalised Bernoulli equation (2.13) on the free surface (denoted $x = \eta(y)$) is given by

$$q^2 - \frac{2}{F^2}x + \frac{2}{\alpha}\kappa = B, \qquad \text{for } x = \eta(y), \tag{3.3}$$

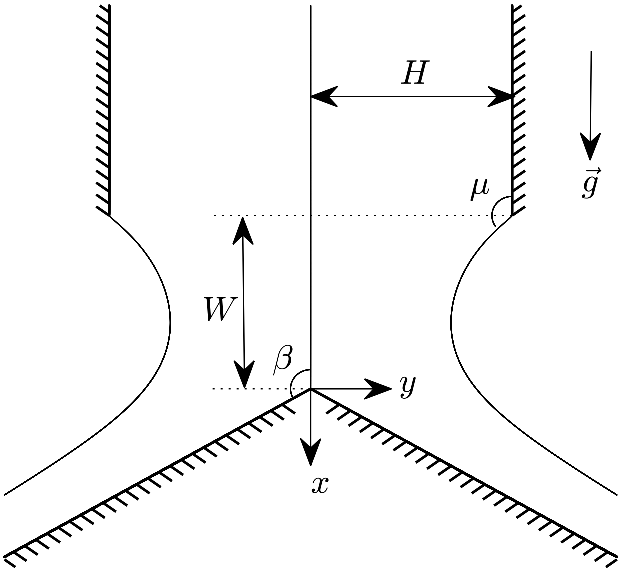

Figure 3.3: Flow configuration in the z-plane

where F is the Froude number, given by (3.1), and α the Weber number, given by (3.2).

Due to the symmetry of the problem about the line $y = 0$, we can restrict our attention to the problem in $0 \leq \psi \leq 1$ ($y \geq 0$). Recalling that x points in the direction of gravity, the boundary conditions in the z-plane are

$$\arg(\xi) = 0, \qquad \text{for } \arg(z) = -\pi, \tag{3.4}$$

$$\arg(\xi) = 0, \qquad \text{for } x \in (-\infty, -W],\ y = 1, \tag{3.5}$$

$$\arg(\xi) = \beta - \pi, \qquad \text{for } \arg(z) = \pi - \beta, \tag{3.6}$$

$$q^2 - \frac{2}{F^2}\eta(y) + \frac{2}{\alpha}\kappa = B, \qquad \text{for } x = \eta(y). \tag{3.7}$$

For the case of $\beta = \pi$, this problem becomes that of flow exiting a pipe. The central streamline $\psi = 0$ no longer hits a wedge, but becomes a line of symmetry. Since we are dealing with inviscid potential flow, we can take this line of symmetry to be a wall. Furthermore, we can use the symmetry about the streamline $\psi = -1$, as shown in figure 3.4. Viewed this way, we see that this problem is then equivalent to that of a plane bubble, shown in figure 3.2. The separation angle μ is now the angle between

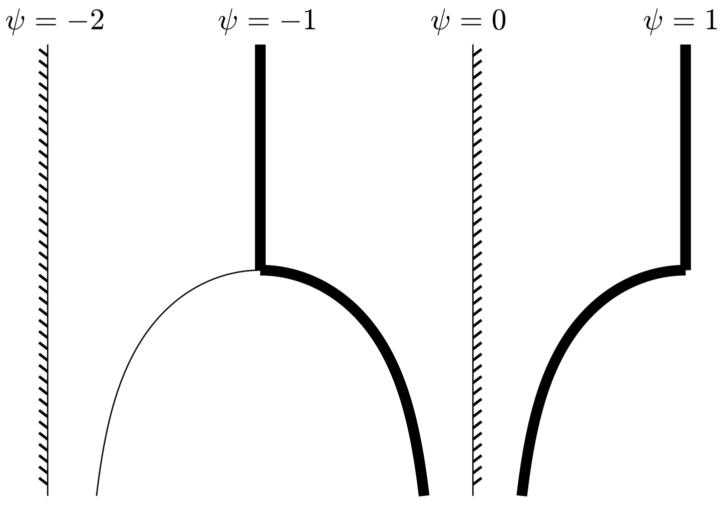

Figure 3.4: The boundaries of figure 3.3 with $\beta = \pi$ are shown in bold. Taking the central streamline as a boundary, and reflecting across the streamline $\psi = -1$, we see this configuration is equivalent to that of a plane bubble.

the central streamline and the bubble surface. This problem was solved numerically both when $\alpha^{-1} = 0$ (i.e. no surface tension) and with finite α in a sequence of papers by Vanden-Broeck ([80], [81], [82]). The main results of these papers are repeated at the end of this chapter, since they offer insight into the solution space for the axisymmetric analogue of this problem (see chapter 4).

When $\beta = \pi/2$, this problem becomes that of flow exiting a pipe onto a flat plate. This was solved numerically when $\alpha^{-1} = 0$ by Christodoulides and Dias [21]. We will provide a modification to their numerical scheme to solve the more general problem with arbitrary β. However, first, we will present an exact solution to this problem, under the assumption that both gravity and surface tension are negligible ($F \to \infty, \alpha \to \infty$).

3.3 Free streamline solution

Problems in which all external forces are ignored are often referred to as free streamline problems. In such cases, the continuity of pressure condition (3.7) on a free surface becomes

$$q = \text{constant}, \qquad \text{on} \quad x = \eta(y), \tag{3.8}$$

where q is the magnitude of the velocity vector. Free streamline flows were very popular in the late 19th and early 20th century, since they could often be solved analytically using conformal mapping techniques. A review can be found in the books by Birkhoff and Zarantonello [12] and Gurevich [46]. We will present an exact solution to the flow configuration shown in figure 3.5, using a method devised by Love [58]. The method was modified by Hopkinson [48] to allow for internal singularities, and revisited recently by Eggers and Smith [36]. We restrict our attention to $0 \leq \psi \leq 1$, using symmetry to take $\psi = 0$ as a solid boundary. Throughout this section, points A, B, C and D will refer to the points as shown in figure 3.5 (A is the flow upstream, B where the two walls meet, C the separation point and D is downstream). We note that the configuration shown in figure 3.5 is the same as that shown in figure 3.3, but with $\mu = \pi$. No other value of μ is possible, since if $\mu < \pi$, then the value of q at the separation point C is zero, while if $\mu > \pi$, then it is infinite. This can be shown by noting that the local behaviour at the separation point is flow inside a corner with interior angle μ, which is given by

$$f \sim z^{\pi/\mu}, \qquad \xi \sim z^{\pi/\mu - 1}. \tag{3.9}$$

From this, one can see that as $z \to 0$, $|\xi| \to \infty$ if $\mu > \pi$, while if $\mu < \pi$, $\xi \to 0$. In either case, equation (3.8) cannot be satisfied.

The method involves conformally mapping the problem on to an auxilliary t-plane, which we take to be the upper half-plane, such that all boundaries map onto the real axis. The t-plane is shown in figure 3.6. This mapping is found by guessing a complex potential $f(t)$ which will give us the desired properties of the flow. Full details can be found in Hopkinson [48], but for this problem, we take $f(t)$ to be a

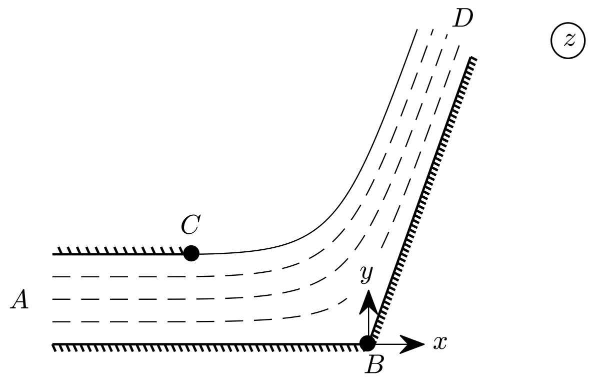

Figure 3.5: Flow configuration in the z-plane. Dashed curves are streamlines.

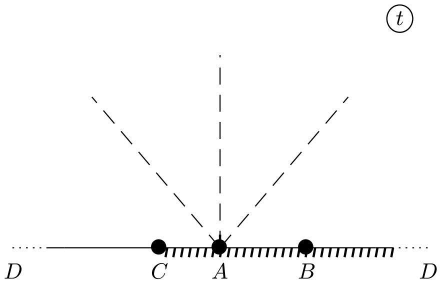

Figure 3.6: Flow configuration in the t-plane.

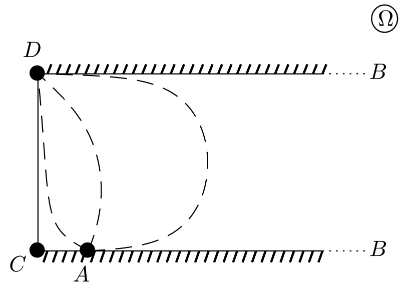

Figure 3.7: Flow configuration in the Ω-plane.

point source at the point $t = 0$, given by

$$f(t) = \frac{1}{\pi} \log t. \tag{3.10}$$

Equation (3.10) has the property that $\psi = 0$ for $t \in \Re^+$, while $\psi = 1$ for $t \in \Re^-$. Hence, the streamline ABD is mapped onto the positive real axis, while the streamline ACD is mapped onto the negative real axis in the t-plane. Since we have a free constant in the mapping (the mapping $t'(z) = at(z)$ for $a \in \Re \backslash \{0\}$ is conformal if the mapping $t(z)$ is conformal), without loss of generality, we choose $t = 1$ at the point B, and $t = -d$ for the point C, where $d \in \Re^+$. The constant d is a free parameter of the problem. It is found that decreasing d increases the height of the pipe relative to the point B (the value W in figure 3.3).

To find the mapping $z(t)$, we integrate the following identity

$$\frac{dz}{dt} = \frac{dz}{df}\frac{df}{dt} = e^{\Omega}\frac{df}{dt} \tag{3.11}$$

Hence, to find $z(t)$, it is left to find the function dz/df, which can be done by considering the function Ω, given by

$$\Omega = \log\frac{dz}{df} = \log\frac{1}{q} + i\theta, \tag{3.12}$$

where $\xi = qe^{-i\theta}$. It can be seen from equation (3.8) that the real contribution to Ω is constant along the free streamline, and likewise from equations (3.4)-(3.6) that the imaginary contribution is constant along a straight wall. Hence, we have that $d\Omega/dt \in \Re$ along walls, and $d\Omega/dt \in \Im$ on the free surface. Recalling that x points in the direction of the flow in the pipe, the vertical walls AB and AC are mapped onto the horizontal line $\theta = 0$ in the Ω-space, while the wall BD is a horizontal line given by $\theta = \pi - \beta$. The free streamline maps onto the vertical line connecting C and D. Finally, we note that at B there is a stagnation point (for all values of $\beta \neq \pi$). We see from equation (3.12) that $\Re(\Omega) \to \infty$ when $q \to 0$, and hence B is mapped to the point at infinity in the Ω-space. The whole Ω-space is a semi-infinite strip, where the points A, B, C and D map to

$$A: \quad \Omega(0) = 0, \tag{3.13}$$

$$B: \quad \lim_{t\to 1}\Omega(t) = +\infty, \tag{3.14}$$

$$C: \quad \Omega(-d) = -\log q_C, \tag{3.15}$$

$$D: \quad \lim_{|t|\to\infty}\Omega(t) = -\log q_C + (\pi - \beta)i, \tag{3.16}$$

where q_C is the value of q at the point C, and is hence the value of the constant in equation (3.8). It is later found as a function of the free parameter d. The

Ω-space is shown in figure 3.7. The function $\Omega(t)$ can be derived by finding the Schwarz-Christoffel mapping from the Ω-space to the t-space. Since there are no internal singularities or zeros of df/dz, equation (3.12) implies the same can be said of $d\Omega/dt$, and hence the mapping is conformal. The Schwarz-Christoffel mapping of a triangle with nodes C, D and B, and interior angles $\pi/2, \pi/2$ and 0 onto the upper half-plane is given by

$$\Omega(t) = \int^t \frac{L_1}{\sqrt{s+d}\,(s-1)}\,\mathrm{d}s, \tag{3.17}$$

where L_1 is an unknown constant. Integration of equation (3.17) gives

$$\Omega(t) = -L_3 \tanh^{-1}\left(\sqrt{\frac{t+d}{1+d}}\right) + L_2. \tag{3.18}$$

where $L_3 = L_1/\sqrt{d+1}$. The constants L_2, L_3 and q_C can be found by noting that the points A, C, and D are given in both spaces by equations (3.13), (3.15), and (3.16) respectively. Evaluating (3.18) at C gives

$$L_2 = -\log(q_C). \tag{3.19}$$

Furthermore, evaluating (3.18) at D gives

$$L_3 = 2\left(1 - \frac{\beta}{\pi}\right). \tag{3.20}$$

Finally, evaluating equation (3.18) at A gives

$$\log q_C = -2\left(1 - \frac{\beta}{\pi}\right)\tanh^{-1}\left(\sqrt{\frac{d}{d+1}}\right). \tag{3.21}$$

Combining all of the above, we find

$$\Omega(t) = 2\left(\frac{\beta}{\pi} - 1\right)\left[\tanh^{-1}\left(\sqrt{\frac{t+d}{d+1}}\right) - \tanh^{-1}\left(\sqrt{\frac{d}{d+1}}\right)\right]. \tag{3.22}$$

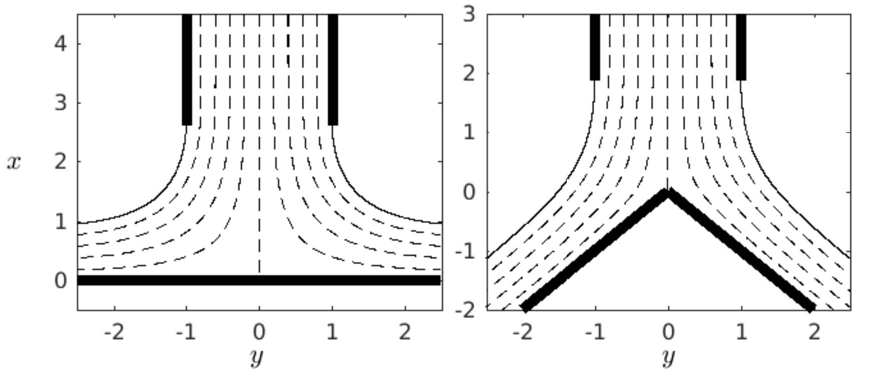

Figure 3.8: Some free streamline solutions for $d = 0.01$ and $\beta = \pi/2$, $3\pi/4$ for the figure on the left and right respectively.

Hence, we have found $\Omega(t)$. Substituting this into equation (3.11), we have an identity we can integrate to find $z(t)$. The integration can be done analytically when $\beta \in \{\pi/2, \pi\}$. For all other values of β, the integration must be done numerically, as described below.

To plot a streamline $\psi = \bar{\psi}$, we truncate ϕ below by $a < 0$ and above by $b > 0$. We then discretise ϕ with N equally spaced points, given by

$$\phi_I = a + (b-a)\frac{(I-1)}{N-1}, \qquad I = 1, 2, \cdots, N. \tag{3.23}$$

We can then use equation (3.10) to find the corresponding points t_I, given by

$$t_I = \exp\left(\pi(\phi_I + \bar{\psi})\right). \tag{3.24}$$

We must choose $|a|$ to be sufficiently large such that the flow at ϕ_1 is far away from the separation point C, and is given by a uniform stream $z = f$. We can then write $z(t_1) = \bar{\psi} i$. It is left to integrate equation (3.11) via the trapezoidal rule. Denoting $g(t) = e^{\Omega}/\pi t$, we find

$$z(t_{I+1}) = z(t_I) + (t_{I+1} - t_I)\left[g(t_I) + g(t_{I+1})\right]. \tag{3.25}$$

The method above allows us to plot streamlines of the flow in the z-space. Some typical solutions are shown in figure 3.8. The boundaries are given by the bold lines, internal streamlines by dashed curves, and the free surface is the solid curve.

In the following section, we will describe a numerical method to find solutions to the problem shown in figure 3.3, with the inclusion of gravity and surface tension.

3.4 Inclusion of gravity and surface tension

In this section, we will present a numerical series truncation method used to compute fully nonlinear solutions to the system of equations (3.4)-(3.7), for finite values of F and α. For a review of series truncation methods applied to steady potential flow, see §3 of Vanden-Broeck [87]. This chapter will follow closely the work of Vanden-Broeck ([80], [81]), who solved this problem for $\beta = \pi$ with surface tension and gravity, and Christodoulides and Dias [21], who likewise devised a method to find solutions with gravity for $\beta = \pi/2$.

The method once again involves conformally mapping the flow domain to an auxiliary t-plane. This time we choose the t-plane to be a unit semi-circle (in the upper half-plane). Given that the flow domain in the f-space is given by an infinite strip $0 \leq \psi \leq 1$, the mapping from f to t is found to be

$$f(t) = \frac{1}{\pi} \log \left(\frac{4t}{(1-t)^2} \right) - \phi_C. \tag{3.26}$$

The constant ϕ_C is the value of ϕ at the separation point. All the walls map onto the real axis: the wall AB maps to $t \in [0, t_B]$, the wall BD to $t \in [t_B, 1]$ and the wall AC maps to $t \in [-1, 0]$. The constant t_B is a free parameter of the problem, similar to the constant d in the previous section. The free surface maps onto the curve $t = e^{i\sigma}$ for $\sigma \in [0, \pi]$. The flow domain in the f-space and t-space are shown in figures (3.9)

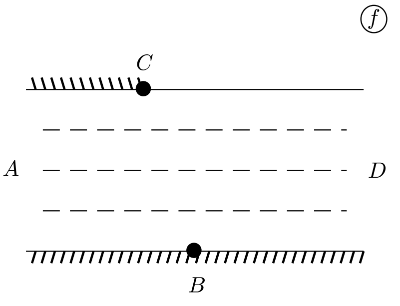

Figure 3.9: Flow configuration in the f-plane. Dashed curves are streamlines.

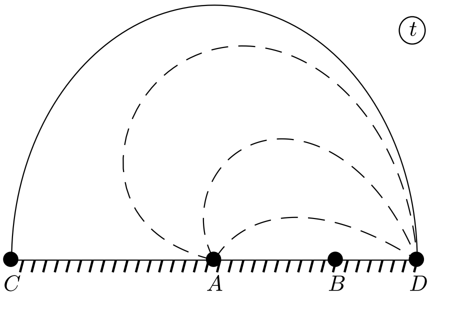

Figure 3.10: Flow configuration in the t-plane. Dashed curves are streamlines.

and (3.10) respectively.

Following the discussions of section 2.2.1, we wish to express ξ as a power series t. To ensure this series converges, we must remove all the singularities of $\xi(t)$ in $\{t : |t| \leq 1, \Im(t) \geq 0\}$. The first singularity we will consider comes from the separation point C ($t = -1$). The flow here behaves like the flow in a corner of angle μ (see figure 3.3). Using equations (3.9) and (3.26), one finds the singular behaviour

$$\xi \sim (t+1)^{2-2\mu/\pi}, \qquad \text{as } t \to -1. \tag{3.27}$$

It is known that when ignoring surface tension, only three values of μ can satisfy (3.7): $\mu = \pi/2$, $2\pi/3$ and π (see Vanden-Broeck [87] §3). When surface tension is also included, any value of μ is permissible.

Next, we consider the singularity at the tip of the wedge B ($t = t_B$). Similar to equation (3.27), the leading order singular behaviour is that of flow in a corner of interior angle β. Again, using equations (3.9) and (3.26) , one finds

$$\xi \sim (t - t_B)^{1-\beta/\pi}, \qquad \text{as } t \to t_B. \tag{3.28}$$

The final singularity is associated with the flow in the far-field D ($t = 1$). The singularity has two possible behaviours, depending on the value of β, as shown in the following section.

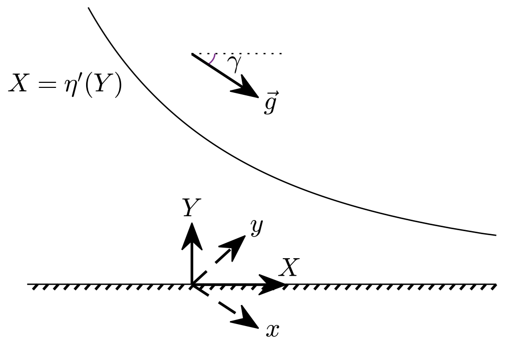

Figure 3.11: Flow in the far-field, as described in section 3.4.1.

3.4.1 Asymptotic behaviour in the far-field ($\beta \neq \pi/2$)

Consider the dynamic boundary condition on the free surface (3.7)

$$\frac{1}{2}(u^2+v^2) - \frac{1}{F^2}x + \frac{1}{\alpha}\kappa = B, \quad \text{for } x = \eta(y). \tag{3.29}$$

If $\beta \neq \pi/2$, then $x \to \infty$ as we move further along the wall, and thus we must balance the x term in (3.29) with the inertial term (it makes little physical sense to balance it with infinite curvature). It will be beneficial to consider a new set of Cartesian coordinates, (X, Y), where X is parallel to the wall BD, and Y is perpendicular to X. Denote the velocity in the coordinates (X, Y) as $\vec{U} = (U, V)$. Gravity acts at an angle $-\gamma$ to the direction X, where $\gamma = \pi - \beta$. We denote the free surface $X = \eta'(Y)$. Figure 3.11 shows the far-field in the transformed coordinates. As with the original coordinates, we can describe the velocity vector $\vec{U}$ in terms of a velocity potential Φ and a streamfunction Ψ. The complex potential $\widehat{F} = \Phi + i\Psi$ in these new coordinates is related to $f = \phi + i\psi$ via the rotation

$$\widehat{F}(z) = e^{i(\pi-\beta)} f(z). \tag{3.30}$$

Equation (3.29) in these coordinates gives

$$\frac{1}{2}(U^2+V^2)-\frac{1}{F^2}X\cos(\pi-\beta)+\frac{1}{\alpha}\kappa=B, \qquad \text{for } X=\eta'(Y). \tag{3.31}$$

Due to conservation of flux, we require that the width of the fluid between the wall and the free surface must become infinitesimally small. Therefore, we expect that the $U >> V$ in this region, and hence leading order balance gives that

$$U=\left(\frac{2\cos(\pi-\beta)}{F^2}X\right)^{1/2}, \quad \text{as } X\to\infty. \tag{3.32}$$

Noting that $\Phi_X=\Psi_Y=U$, we can integrate the above to give

$$\Phi=\left(\frac{2\cos(\pi-\beta)}{F^2}\right)^{1/2}\frac{2}{3}X^{3/2}, \tag{3.33}$$

$$\Psi=\left(\frac{2\cos(\pi-\beta)}{F^2}\right)^{1/2}X^{1/2}Y, \tag{3.34}$$

and hence $\widehat{F}$ is given by

$$\widehat{F}=\left(\frac{8\cos(\pi-\beta)}{9F^2}\right)^{1/2}\left(X^{3/2}+\frac{3i}{2}X^{1/2}Y\right). \tag{3.35}$$

Denoting $Z=X+iY$, we have that for large values of X,

$$Z^{3/2}=X^{3/2}\left(1+i\frac{Y}{X}\right)^{3/2}\sim X^{3/2}+\frac{3i}{2}X^{1/2}Y. \tag{3.36}$$

We can see from equations (3.35) and (3.36) that $\widehat{F}$ has the asymptotic behaviour

$$\widehat{F}\sim Z^{3/2}, \quad \text{as } X\to\infty. \tag{3.37}$$

Recall that f is related to F by a multiplicative constant (see equation (3.30)). The same is clearly true for z and Z. Noting that the far-field is mapped to $t=1$ in the

t-plane, we can conclude that

$$f \sim z^{3/2}, \quad \text{as } t \to 1. \tag{3.38}$$

Hence, the complex velocity ξ has the asymptotic behaviour

$$\xi \sim z^{1/2} \sim f^{1/3}. \tag{3.39}$$

To the author's knowledge, this singular behaviour was first discussed by Birkhoff and Carter [11]. Using equation (3.26), we find that

$$\xi \sim (-\log(1-t))^{1/3}. \tag{3.40}$$

Therefore, we have found the leading order singular behaviour of $\xi(t)$ in the far-field downstream when $\beta \neq \pi/2$. Next, we will consider the behaviour when $\beta = \pi/2$.

3.4.2 Asymptotic behaviour in the far-field ($\beta = \pi/2$)

When $\beta = \pi/2$, the flow downstream ($y \to \infty$) approaches either a uniform stream of depth H_f and velocity U_f travelling in the positive y direction, or a periodic train of waves. Our method only allows us to compute solutions for which ξ is single valued at $t = 1$, and hence we cannot compute solutions for which the far-field has a train of waves. Since we have taken the channel width and velocity upstream (i.e. flow from the pipe) as the reference length and velocity respectively, conservation of flux gives us that $H_f = 1/U_f$. We can calculate the Froude number downstream F_f and Weber number downstream α_f in relation to F and α (see equations (3.1) and

(3.2)) via the identities

$$F_f = U_f^{3/2} F, \qquad \alpha_f = U_f \alpha. \tag{3.41}$$

We linearise the flow about a uniform stream in the far-field to find the asymptotic behavior of $\xi(t)$. The complex potential of a uniform stream with velocity U_f travelling in the positive y direction is given by $f = -iU_f z$. We consider a small perturbation to this uniform stream by writing

$$\phi(x, y) = U_f y + \widehat{\phi}(x, y), \tag{3.42}$$

$$\xi(x, y) = U_f + \widehat{\xi}(x, y), \tag{3.43}$$

$$\eta(y) = -H_f + \widehat{\eta}(y), \tag{3.44}$$

where $|\widehat{\phi}|$, $|\widehat{\xi}|$, $|\widehat{\eta}|$ and their derivatives are assumed to be small. Substituted into the governing equation and boundary conditions, the linearised system is

$$\widehat{\phi}_{xx} + \widehat{\phi}_{yy} = 0, \qquad \text{for } -H_f < x < 0, \tag{3.45}$$

$$\widehat{\phi}_x = 0, \qquad \text{on } x = 0, \tag{3.46}$$

$$\widehat{\phi}_x - U_f \widehat{\eta}_y = 0, \qquad \text{on } x = -H_f, \tag{3.47}$$

$$U_f \widehat{\phi}_y + \frac{1}{F^2}\widehat{\eta} - \frac{1}{\alpha}\widehat{\eta}_{yy} = 0, \qquad \text{on } x = -H_f. \tag{3.48}$$

We differentiate (3.48) with respect to y and combine it with (3.47) to eliminate $\widehat{\eta}$ from the free surface boundary conditions,

$$\widehat{\phi}_{yy} + \frac{1}{U_f^2 F^2}\widehat{\phi}_x - \frac{1}{\alpha U_f^2}\widehat{\phi}_{xyy} = 0 \quad \text{on } y = 0. \tag{3.49}$$

We solve this linear system of equations by separation of variables. We write

$$\widehat{\phi} = X(x)Y(y), \tag{3.50}$$

and substitute this into (3.45), which when re-arranged gives

$$-\frac{X''}{X} = \frac{Y''}{Y} = \pi^2\lambda^2 U_f^2. \tag{3.51}$$

Here $\pi^2\lambda^2 U_f^2$ is the separation constant and X'' denotes d^2X/dx^2. The boundary condition (3.46) becomes

$$X'(0) = 0. \tag{3.52}$$

Solving (3.51), we obtain the general solution

$$\widehat{\phi} = C \exp\left(-\pi\lambda U_f y\right) \cos\left(\pi\lambda U_f x\right), \tag{3.53}$$

where C is an arbitrary constant. We ignore the $\exp(\pi\lambda U_f)$ term since we want $\widehat{\phi}$ to remain bounded as $y \to -\infty$. This solution satisfies (3.49) if

$$\pi\lambda - \tan(\pi\lambda)\left(\frac{1}{F_f^2} - \frac{1}{\alpha_f}\pi^2\lambda^2\right) = 0. \tag{3.54}$$

Equations (3.43) and (3.53) give that, up to first order,

$$\xi = U_f + (\widehat{\phi}_x - i\widehat{\phi}_y) = U_f + C\pi\lambda i \exp\left(U_f \pi\lambda i(x+iy)\right). \tag{3.55}$$

Since $f \approx -iU_f z$, we have that $\phi \to \infty$ as $y \to \infty$. Therefore, (3.55) implies that

$$\xi \approx U_F + A\exp\left(-U_f\pi\lambda\phi\right), \quad \text{as } \phi \to \infty, \tag{3.56}$$

where $A = C\pi\lambda i$.

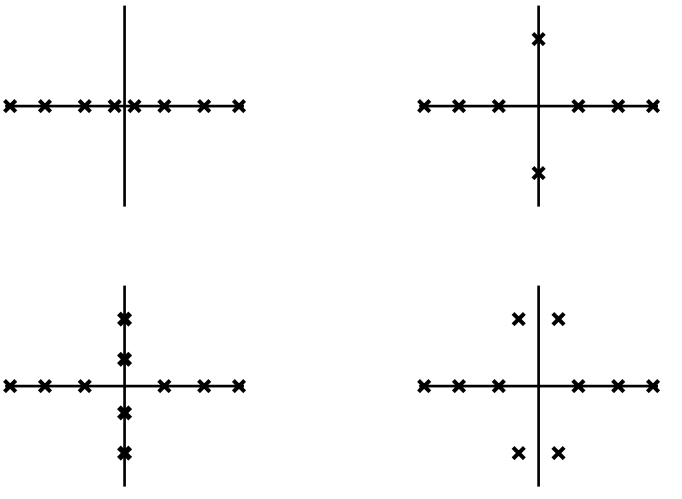

Figure 3.12: The four potential root configurations of equation (3.54). Top left is case I, top right case II, bottom left case III, and bottom right case IV.

The roots λ of equation (3.54) tells us about the behaviour of the flow in the far-field. This equation is the dispersion relation of periodic gravity-capillary waves. The roots are symmetric about the imaginary axis: the roots which satisfy $\Re(\lambda) > 0$ correspond to solutions which approach a uniform stream, while roots with negative real part blow up, and are hence ignored. Purely imaginary roots correspond to a far-field with a periodic wavetrain with wavenumber $|\lambda|\pi$. Given a value of F_f and α_f, there are four potential configurations of the roots λ, as shown in figure 3.12. There always exist infinitely many real roots. Complex and imaginary roots come in conjugate pairs. There is either no imaginary or complex roots (case I), one purely imaginary conjugate pair (case II), two purely imaginary conjugate pairs (case III), or two complex conjugate pairs (case IV). The magnitude of the real part of the complex roots is always less than that of the first positive real root.

When surface tension is taken to be zero, then we have case I when $F_f > 1$. The far-field approaches a flat surface, and the leading order singularity is given by the first positive real root $\lambda \in (0, 1/2)$. It is sufficient to remove the singularity associated with just the aforementioned $\lambda \in (0, 1/2)$ to obtain convergence of the numerical method. When $F_f < 1$, we have case II. The leading order behaviour is given by the imaginary roots, and corresponds to a far-field with a periodic wave-train. Hence, when the flow in the far-field is subcritical, for zero surface tension one would expect to see linear surface water waves.

Now let us assume that surface tension is nonzero. We find it useful to define the nondimensional Bond number τ as

$$\tau = \frac{T}{\rho g H^2} = \frac{F^2}{\alpha}. \tag{3.57}$$

The Bond number downstream is given by $\tau_f = U_f^2 \tau$. When $F_f > 1$, we have case II. When considering $F_f < 1$, there are a variety of possible configurations. First, if $\tau_f > 1/3$, then we have case I. If $\tau_f < 1/3$, then for a given α_f, there exists a critical value $\widetilde{F_f}$ such that when $\widetilde{F_f} < F_f < 1$ we have case III. The far-field is given by a periodic wave-train of two different modes. This is higher mode resonance, often referred to as Wilton ripples. When $F < \widetilde{F_f}$, we have case IV. In this circumstance, the flow approaches a uniform stream. The leading order singularities are the two complex roots with positive real parts, and the far-field has infinitesimal oscillations.

In the following section, we will describe the series representations of $\xi(t)$ used for the different flow configurations discussed in this section.

3.4.3 Power series representation of $\xi(t)$

In the previous section, we found all the leading order singularities of $\xi(t)$ in the flow domain. We have two representations of ξ, depending on the value of β. When $\beta \neq \pi/2$, consider a representation of $\xi(t)$ as follows:

$$\xi = \frac{(-\log C(1-t))^{1/3}}{(-\log C)^{1/3}} \left(\frac{t_B - t}{t_B}\right)^{1-\beta/\pi} (t+1)^{2-2\mu/\pi} \exp\left(\sum_{n=1}^{\infty} a_n t^n\right), \tag{3.58}$$

	$F = 0.3$		$F = 1.5$	
Coefficient	S1	S2	S1	S2
a_{200}	10^{-6}	10^{-5}	10^{-7}	10^{-5}
a_{1000}	10^{-9}	10^{-6}	10^{-9}	10^{-6}
a_{2000}	10^{-15}	10^{-7}	10^{-16}	10^{-7}

Table 3.2: Table comparing the order of the coefficients a_n for the series (3.59) (denoted S1), and the series (3.60) (denoted S2) for two values of F. Both solutions have $t_B = 0.97$.

where C is a fixed constant satisfying $0 < C < 0.5$, such that ξ is purely real on the line $t \in [-1, t_B]$. It can be seen that (3.58) satisfies the singular behaviour (3.27), (3.28), and (3.40), and that $\xi(0) = 1$. This series, with $\beta = \pi$, was used by Vanden-Broeck ([80], [81], [82]) and Daripa [25]. If $\beta = \pi/2$, then we instead take

$$\xi = \left(\frac{t_B - t}{t_B}\right)^{1-\beta/\pi} (t+1)^{2-2\mu/\pi} \exp\left(-A + A(1-t)^{2\lambda} + \sum_{n=1}^{\infty} a_n t^n\right), \qquad (3.59)$$

where A and λ are unknown, and have to be found as part of the solution. The constant λ is taken to be the root of (3.54) with the smallest positive real part. This series was used by Christodoulides and Dias [21]. However, they did not include the term $\exp(A(1-t)^{2\lambda})$ in their expansion, and instead used the series representation

$$\xi = \left(\frac{t_B - t}{t_B}\right)^{1-\beta/\pi} (t+1)^{2-2\mu/\pi} \exp\left(\sum_{n=1}^{\infty} a_n t^n\right). \qquad (3.60)$$

We found that, truncating the series after a sufficient number of coefficients, their results agree within graphical accuracy with those computed using the series (3.59). However, the coefficients a_n decay at a much slower rate without this new exponential term, as shown in table 3.2. This demonstrates that the singularity is important to remove for the convergence of the series.

We truncate both series after N terms. When $\beta \neq \pi/2$, this results in $N + 1$ unknowns $(a_1, \cdots, a_N, \mu)$. The free surface in the t-plane is given by $t = e^{i\sigma}$. We differentiate Bernoulli's equation (3.29) with respect to σ, resulting in

$$uu_\sigma + vv_\sigma + \frac{1}{\pi F^2}\frac{u}{u^2+v^2}\cot\frac{\sigma}{2} - \frac{\pi}{\alpha}\frac{\partial}{\partial\sigma}\left[\frac{uv_\sigma - vu_\sigma}{(u^2+v^2)^{1/2}}\tan\frac{\sigma}{2}\right] = 0. \tag{3.61}$$

We discretise σ into $N+1$ equally space points, given by

$$\sigma_I = \pi\frac{(I-1/2)\pi}{N+1}, \qquad I = 1, \cdots, N+1. \tag{3.62}$$

We then satisfy equation (3.61) at each meshpoint σ_I. This gives us $N+1$ equations for $N+1$ unknowns, which are solved via Newton's method. When $\beta = \pi/2$, we have two additional unknowns, A and λ. Therefore, we satisfy equation (3.61) at $N+2$ equally spaced points in σ, given by

$$\sigma_I = \frac{(I-1/2)\pi}{N+2}, \qquad I = 1, \cdots, N+2. \tag{3.63}$$

We also satisfy equation (3.54), where F_f is calculated using equation (3.41), and U_f can be found by evaluating (3.59) at $t = 1$. Hence, we have obtained $N+3$ equations for $N+3$ unknowns, a system which can be solved numerically using Newton's method.

Thus concludes the formulation and the numerical method. In the following section, we will show the results.

3.5 Results

The following three subsections discuss the results for when $\beta = \pi/2$ (flow onto a plate), $\beta \in (\pi/2, \pi)$ (flow onto a wedge), and when $\beta = \pi$ (plane bubbles).

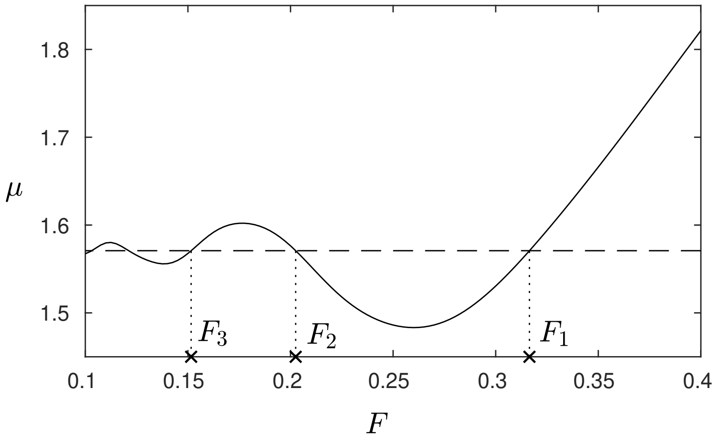

Figure 3.13: A plot of μ as a function of F for $\alpha = 5$. The dashed line is at $\mu = \pi/2$. Values of F_1, F_2 and F_3 are demonstrated graphically.

3.5.1 Plane bubbles: $\beta = \pi$

We begin by discussing the results when $\beta = \pi$, where we use the series representation (3.58) for ξ. The following results are found in Vanden-Broeck ([80], [81], [82]), and are repeated here since they will be required in the following chapter. First, consider the case when $T = 0$. For each value of F, there is a unique solution. As previously explained, there exists a critical value of the Froude number, $F_C \approx 0.51$, such that for $F < F_C$, the bubbles are smooth, while if $F > F_C$, we have cusped bubbles (see table 3.1). The $F = F_C$ solution is the unique pointed bubble, with $\mu = 2\pi/3$. In the experiments of Collins [22], plane bubbles in a regime with a large Re and α were found to have a unique Froude number, given by $F_e \approx 0.35$. The model without surface tension emits an infinite continuous set of possible smooth bubbles. Surface tension can be included to select a unique solution, as described below.

When surface tension is included, the angle μ now has a continuous dependence on the Froude number F. The dependency is shown for $\alpha = 5$ in figure 3.13. As α is increased, the amplitude and frequency of the oscillations about the line $\mu = \pi/2$ decrease and increase respectively. The figure demonstrates the sequence of values F_1, F_2, $\cdots$ for which the $\alpha = 5$ branch intersects the curve $\mu = \pi/2$. As we vary

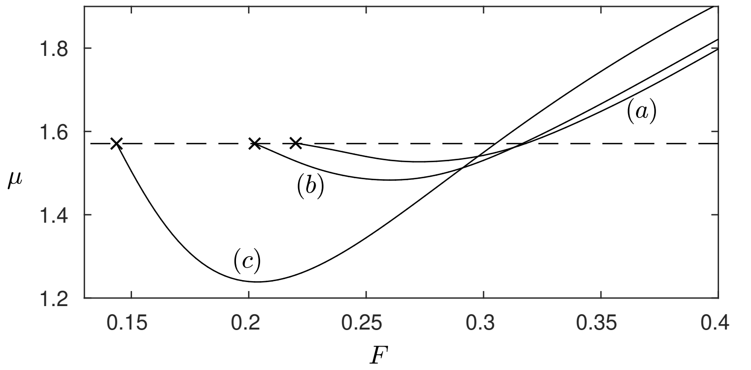

Figure 3.14: A plot of μ as a function of F for (a) $\alpha = 10$, (b) $\alpha = 5$ and (c) $\alpha = 1$. The dashed line is at $\mu = \pi/2$. Each solution branch has been truncated at the second intersection $F_2(\alpha)$. As α increases, the value of $F_2(\alpha)$ monotonically increases (i.e. $F_2(10) > F_2(5) > F_2(1)$).

α, the values of F where the intersections occur increase (see figure 3.14, where this is demonstrated for F_2). Let us denote $F_1(\alpha)$ as the largest value of F where the curves intersect for a given α, $F_2(\alpha)$ as the second largest such value, and so on. These branches $F_i(\alpha)$ are branches of smooth bubbles, and are monotonically increasing with α. As $\alpha \to \infty$, all of these branches converge onto a single value, $F = F^*$. It is found that $F^* \approx 0.318$. The mechanism by which a unique solution is chosen from a possible set of solutions, by including surface tension (or other forces), and taking said forces to zero, is known as solution selection. We conjecture that the same solution selection mechanism occurs for axisymmetric Taylor bubbles, as discussed in the chapter 4. We will compare the results of this section to the results for plane bubbles found using the numerical scheme derived in the following chapter as a check on the numerical method.

3.5.2 Flow onto a wedge: $\beta \in (\pi/2, \pi)$

Now we will vary the angle β, such that the model becomes the flow from a pipe onto a wedge. The flow in the far-field has the same singular behaviour as the bubbles (see section 3.4.1), and hence we again express ξ as (3.58). For a fixed β, we now have two free parameters, F and t_B. Increasing t_B results in raising the

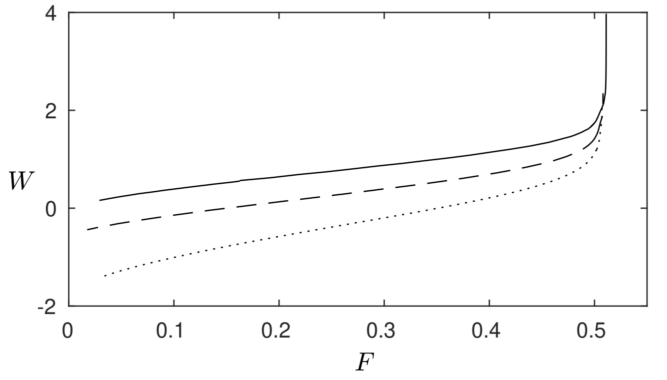

Figure 3.15: Value of F_C for varying W. The solid curve is for $\beta = \pi/2$, dashed curve $\beta = 2\pi/3$ and dotted curve $\beta = 5\pi/6$.

pipe further away from the wedge (i.e. the value of W increases). When surface tension is ignored, we again see a critical value F_C, where the solutions have the properties given in table 3.1. It is now the case that F_C has dependence on t_B (and hence W). As W becomes larger, F_C has a finite limiting value. The dotted and dashed curves in figure 3.15 show the dependence of F_C on W for $\beta = 2\pi/3$ and $\beta = 5\pi/6$ respectively. Streamlines to typical solutions are shown in figure 3.16 for $\beta = 2\pi/3$ and $t_B = 0.96$. The bold lines in the figure correspond to solid boundaries, the dashed curves interior streamline, and the solid curve the free surface. Figure (a) has $F > F_C$, figure (b) $F = F_C$, and figure (c) $F < F_C$. The crosses in figure 3.16(a) is the free streamline solution derived in section 3.3. Since the solution in figure 3.16(a) is for $F = 20$, one would expect reasonable agreement with the free streamline solution ($F \to \infty$). It can be seen the agreement is very good near the separation point. However, as one moves further along the profile, the solutions start to deviate, due to the different singular behaviour downstream (the free streamline solution approaches a uniform stream, as opposed to the behaviour (3.40)). This is shown in figure (d), where we have plotted the flow further downstream for the $F = 20$ solution.

When surface tension is included, similar results to the plane bubble are found. One finds the separation angle μ has a continuous dependence on F. For a given α, the value of μ oscillates about $\pi/2$ for values of $F < F_C$. Meanwhile, when $F \to \infty$,

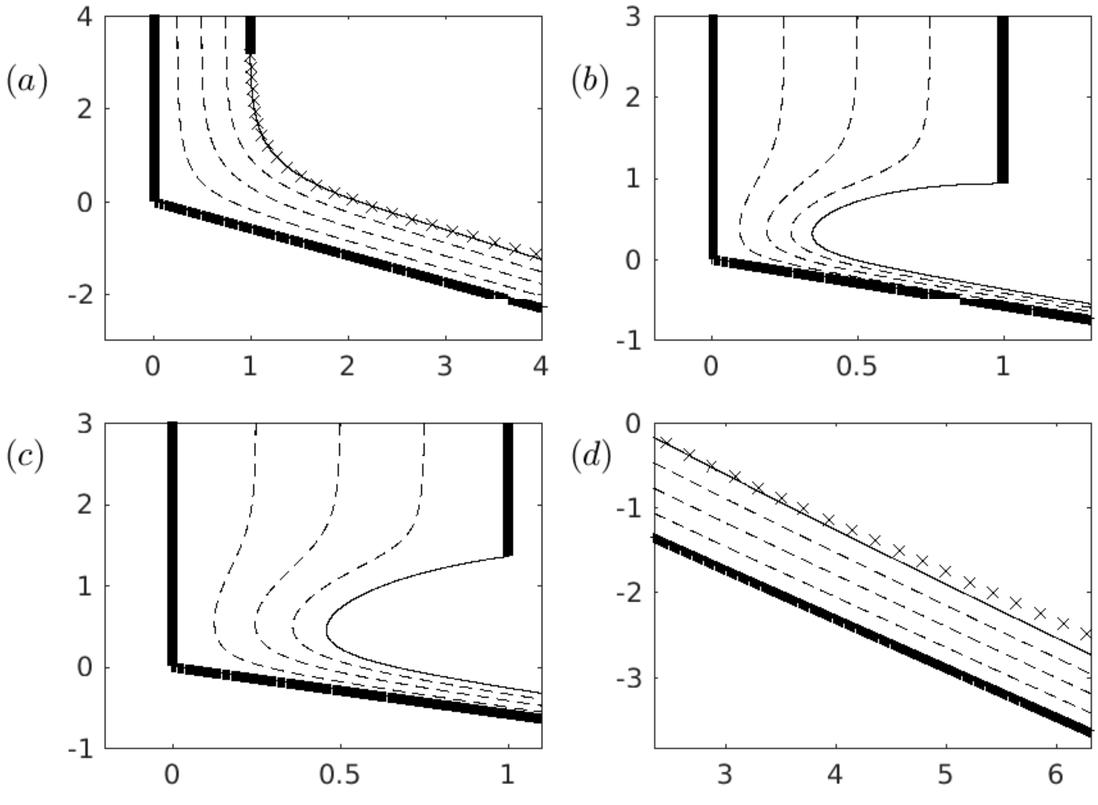

Figure 3.16: Solutions for $t_B = 0.96$, $\alpha^{-1} = 0$, and (a) $F = 20$, (b) $F = F_C(t_B) = 0.4970$ and (c) $F = 0.3$. The crosses in figure (a) is the corresponding $F \to \infty$ solution. Figure (d) shows the far-field of figure (a). Only half a solution ($0 \leq \psi \leq 1$) is shown: the central streamline is taken to be a wall.

$\mu \to \pi$. This is shown in figure 3.17, where the relation between F and μ is shown for $\alpha = 5$ and $\alpha = 20$ (here, $t_B = 0.96$ and $\beta = 2\pi/3$). One could again use the solution selection procedure to find a unique solution to the zero surface tension problem with a separation angle of $\mu = \pi/2$. However, there is no clear physical significance to the selected solution.

3.5.3 Flow onto a plate: $\beta = \pi/2$

Finally, we consider the case when the wedge is replaced by a flat plate. First, consider the case when $T = 0$. The following results are found in Christodoulides and Dias [21]. We used the series representation (3.59) for ξ, while Christodoulides and Dias used (3.60). The improved convergence of the coefficients of the series

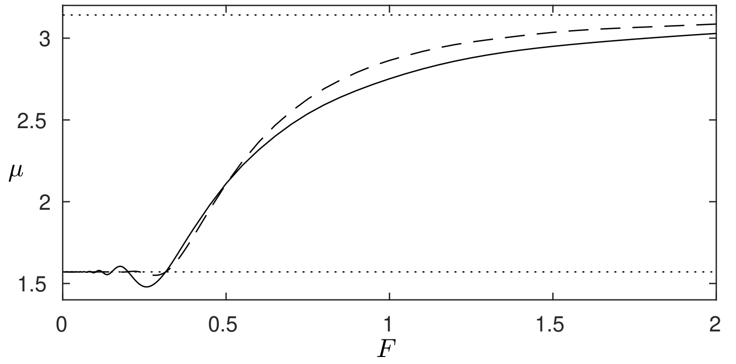

Figure 3.17: Relationship between μ and F for $\alpha = 5$ (solid curve) and $\alpha = 20$ (dashed curve). The dotted lines are $\mu = \pi/2$ and $\mu = \pi$.

when including this additional term has already been discussed. For a fixed value of F and t_B, a unique solution is found. Following the discussion of section 3.4.2, all these solutions are characterised by $F_f > 1$. As with the flows from a pipe onto a wedge, there exists critical Froude number F_C, dependent on t_B, such that table 3.1 describes the gravity free solution space. The dependency between F_C and W is shown by the solid curve in figure 3.15. They also differentiated between regimes where the free surface is 'squeezed' (where the interface $x = \eta(y)$ is not single valued), and those where it is immediately deflected along the plate . For example, from the solutions for flow onto a wedge, in figures 3.16b and 3.16c, the profiles are squeezed, while the profile from figure 3.16a is not. They found the boundary between these two regimes occurs for $F < F_C$.

When surface tension is included, as it stands, we are yet to obtain satisfactory convergent results. We wish to investigate this in the near future, and the possibility of finding such results is discussed in chapter 6.

3.6 Conclusion

In this chapter, we have repeated the calculations of Vanden-Broeck [80], and described the solution space of plane bubbles. We modified the series used by Christodoulides and Dias [21] to improve the convergence of the coefficients for flow impacting a flat plate. We found novel solutions for flow impacting a wedge, and good agreement was found between the free streamline solution and solutions with large values of the Froude number. In the following chapter, we will investigate axisymmetric Taylor bubbles.

Chapter 4

Axisymmetric Taylor Bubbles

In the previous chapter, we discussed the solution space of plane bubbles bounded by two horizontal plates. In this chapter, we will present a numerical scheme used to compute axisymmetric Taylor bubbles rising in a tube. A three-dimensional visualization of the flow is found in figure 3.1b. The results of this chapter can be found in Doak and Vanden-Broeck [32].

4.1 Introduction

It has long been believed that the solution space of axisymmetric Taylor bubbles exhibits similar behaviour to that of plane bubbles. Levine and Yang [57] computed axisymmetric Taylor bubbles using a boundary integral method. They showed that for $T = 0$, there again exists a continuum of solutions $F \in (0, F_C)$ for which the bubble is smooth. It was found that $F_C \approx 0.7$. In this chapter, we show the solution for $F = F_C$ is a pointed bubble with an interior angle of approximately 130^0 (i.e $\mu \approx 115^0$). Similar to the two-dimensional problem, $F = F_C$ is the only value for which we find pointed bubbles with zero surface tension. A local behaviour at the apex of this solution is given by Garabedian [42]. The inclusion of surface tension again reduces the continuous set of smooth bubbles to an infinite discrete set

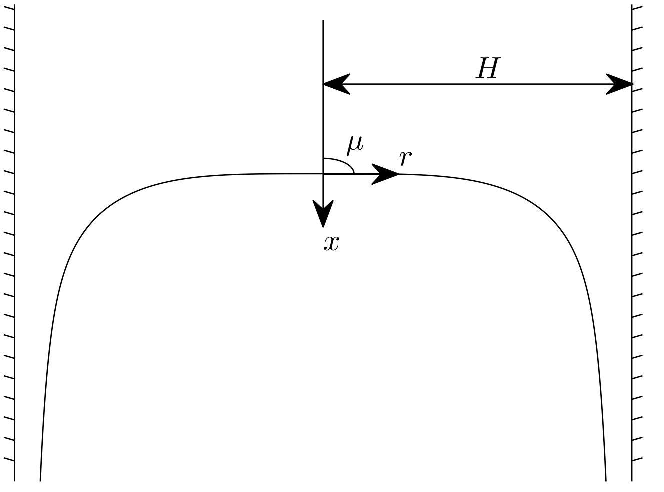

Figure 4.1: Formulation of the problem in the (x, r) space.

$F_1, F_2, \cdots$, where $F_i > F_{i+1}$. As with plane bubbles (see section 3.5.1), the branches F_i have dependence on α. Levine & Yang computed the primary branch $F_1(\alpha)$, and showed that $F_1(\alpha) \to F^* \approx 0.49$ as $\alpha^{-1} \to 0$. This is in excellent agreement with experiments: Viana et al. [91], making use of data collected from a wide range of previously performed experiments, obtain the experimental value $F_e \approx 0.48$ in a regime characterised by large Reynolds number Re and large Weber number α. Levine & Yang also computed a small number of solutions on the branches F_2 and F_3, but did not compute solutions on these branches for small surface tension. In this chapter, we present a numerical scheme capable of computing solutions on the higher order branches $F_2(\alpha), F_3(\alpha), \cdots$. We were unable to compute solutions for $\alpha > 160$. Despite this, similarities between the two-dimensional and axisymmetric solution spaces lead us to conjecture that these higher order solution branches approach F^* as $\alpha^{-1} \to 0$.

The formulation of the problem follows a numerical approach to solving axisymmetric flows first proposed by Woods [94], and later independently by Jeppson [52]. We map the flow domain to an infinite strip by taking the velocity potential ϕ and Stokes streamfunction ψ as independent variables. We then discretise the space and solve the equations via finite differences. Due to the stagnation point singularity at the apex of the bubble, a solution with the same local behaviour as the bubble at the singular point is derived, and a function splitting procedure, previously adopted by a variety of authors (Brennen [16], Southwell [77], Woods [95]), is used to allow for accurate approximation of derivatives. A discussion on the relative errors associated with approximating derivatives with the function splitting method is presented in appendix A.

The chapter is organised as follows. In section 4.2, we formulate the problem. In section 4.3, we present a finite difference scheme used to solve the problem for smooth bubbles, along with an explanation of the function splitting procedure used to regulate the singularity at the apex of the bubble. In section 4.4, we present results for the smooth bubbles. In section 4.5, we describe a method used to compute the $F = F_C$ axisymmetric bubble. Section 4.6 is a conclusion to the chapter.

4.2 Formulation

Consider an axisymmetric bubble rising vertically with constant velocity U through a fluid at rest in a tube of radius H. We take standard cylindrical coordinates (x, θ, r), where we choose x to point in the direction of gravity, and $r \in [0, H]$ to be the radial distance from the central streamline $r = 0$. We take the origin to be at the apex of the bubble and to travel with the bubble such that the problem is steady. In this frame of reference, the background flow at $x \to -\infty$ is a uniform stream in the positive x direction with velocity U . We take H as the reference length and U as the reference velocity. The formulation in the (x, r) space is shown in figure 4.1.

We again consider irrotational flow of an inviscid and incompressible fluid. Therefore, there exists a velocity potential ϕ and Stokes streamfunction ψ given by

$$u = \phi_x = \frac{\psi_r}{r}, \qquad v = \phi_r = -\frac{\psi_x}{r}, \tag{4.1}$$

where u and v are the velocities in the x and r directions respectively, and subscripts denote partial differentiation. Without loss of generality, we take $\phi = 0$ at the apex and $\psi = 0$ on the free surface. Integration of (4.1) at $x \to -\infty$ gives

$$\psi \to \frac{r^2}{2}, \qquad \text{as} \quad x \to -\infty. \tag{4.2}$$

Therefore, the wall is given by $\psi = 1/2$.

On the free surface, as well as $\psi = 0$, we must satisfy the Bernouilli equation (2.12). This is given by

$$q^2 - \frac{2}{F^2}x + \frac{2}{\alpha}\kappa = \text{constant}, \tag{4.3}$$

where q is the magnitude of the velocity, F and α are given by (3.1) and (3.2), and $\kappa = R_1^{-1} + R_2^{-1}$ is the mean curvature of the free surface, where the principle radii of curvature, R_1 and R_2, are counted positive when the centers of curvature lie inside the fluid.

Even though the mapping from the (r, x) to the (ϕ, ψ) space is not conformal, we still find the mapping beneficial. The domain in the (ϕ, ψ) space is the infinite strip $\Omega_\phi = \{\psi \in [0, 1/2], -\infty < \phi < \infty\}$. The approach to the problem follows the work of Woods [94]. We seek r as a function of the independent variables (ϕ, ψ). The key benefit to working in the potential space as opposed to the physical space is that the free surface is fixed to the positive ϕ-axis $(\psi = 0, \phi > 0)$.

The mapping from the (x, r) to the (ϕ, ψ) space produces the relations

$$x_\phi = \frac{1}{2}f_\psi, \qquad x_\psi = -\frac{f_\phi}{2f}, \tag{4.4}$$

where $f = r^2$. Woods derived a governing equation for $f(\phi, \psi)$, given by

$$\frac{f_{\phi\phi}}{f} - \left(\frac{f_\phi}{f}\right)^2 + f_{\psi\psi} = 0. \tag{4.5}$$

Furthermore, it can be shown that

$$q = 2\left(\frac{f_\phi^2}{f} + f_\psi^2\right)^{-1/2}, \tag{4.6}$$

$$\kappa = -\frac{f_\psi q}{2\sqrt{f}} + \frac{q^3}{4\sqrt{f}}\left[f_\psi f_{\phi\phi} - f_\phi f_{\phi\psi} - \frac{1}{2}\frac{f_\psi f_\phi^2}{f}\right]. \tag{4.7}$$

Making use of (4.4), we find it beneficial to differentiate Bernouilli's equation (4.3) with respect to ϕ in order to remove the x term. This gives us

$$qq_\phi - \frac{1}{2F^2}f_\psi + \frac{1}{\alpha}\kappa_\phi = 0. \tag{4.8}$$

The boundary conditions on the central streamline and the wall $f = 1$ can be written as

$$f(\phi, 0) = 0, \qquad \phi < 0, \tag{4.9}$$

$$f(\phi, 1/2) = 1, \qquad \forall\phi, \tag{4.10}$$

respectively. Finally, (4.2) gives us the upstream condition

$$f \to 2\psi, \qquad \text{as} \quad \phi \to -\infty. \tag{4.11}$$

This completes the formulation of the problem. It is left to find f as a function of the independent variables (ϕ, ψ) such that it satisfies (4.5), (4.8), (4.9), (4.10) and (4.11).

In the following section, we will present a finite difference scheme used to solve this system.

4.3 Finite difference scheme

We truncate the infinite strip Ω_ϕ to a finite domain $\Omega_T = \{\psi \in [0, 1/2], \phi \in [-\phi_1, \phi_2]\}$, where ϕ_1 and ϕ_2 are positive real numbers. We must ensure when computing solutions that we truncate far enough both up and downstream such that the solution becomes invariant to truncating the domain further. This is explained in greater detail in section 4.4.

We found it beneficial to perform two coordinate transforms,

$$\phi = \begin{cases} -s^2, & \text{if } \phi < 0, \\ s^2, & \text{if } \phi \geq 0, \end{cases} \tag{4.12a}$$

$$\psi = t^2, \tag{4.12b}$$

to condense meshpoints near the crest and free surface. Using the chain rule, we see that

$$f_\psi = \frac{1}{2t} \ f_t, \tag{4.13a}$$

$$f_{\psi\psi} = \frac{1}{4t^2} \ \left(f_{tt} - \frac{f_t}{t} \right), \tag{4.13b}$$

with similar formula for derivatives with respect to ϕ. We discretise Ω_T with M points in s and N points in t as follows

$$\begin{aligned} s_i &= -Ah + (i-1)h, \qquad & i = 1, \cdots, M, \\ t_j &= \frac{1}{\sqrt{2}} \frac{j-1}{N-1}, \qquad & j = 1, \cdots, N, \end{aligned} \tag{4.14}$$

where $A < M$ is a positive integer, chosen such that there are sufficient points upstream and downstream. From equation (4.14), we can see that

$$\phi_1 = -\left(Ah\right)^2, \qquad \phi_2 = \left((M - A - 1)h\right)^2. \tag{4.15}$$

This choice of discretisation produces MN unknowns: f evaluated at each meshpoint $f(s_i, t_j) = f_{i,j}$. Therefore, we require MN equations. We note that the meshpoints are uniformly spaced in s and t with differences

$$\begin{aligned} \Delta s = s_{i+1} - s_i = h, \\ \Delta t = t_{j+1} - t_j = \frac{1}{\sqrt{2}} \frac{1}{N-1} = k. \end{aligned} \tag{4.16}$$

We will impose an equation at each meshpoint. In all interior nodes, we apply the governing equation (4.5). We apply the boundary condition (4.11) at $\phi = -\phi_1$. This is an approximation, since the boundary condition should be applied in the limit $\phi \to -\infty$, but it is found the error is negligible given ϕ_1 is sufficiently large, as discussed in section 4.4. We apply the wall and free surface boundary conditions at their respective places on the mesh. The full discrete system of equations is given by

$$\frac{\partial^2 f_{i,j}}{\partial \psi^2} + \frac{\partial^2 f_{i,j}}{\partial \phi^2} / f_{i,j} - \left[\frac{\partial f_{i,j}}{\partial \phi} / f_{i,j}\right]^2 = 0, \qquad \text{for} \begin{cases} i = 2, \cdots, M, \\ j = 2, \cdots, N-1, \end{cases} \tag{4.17a}$$

$$f_{i,N} - 1 = 0, \qquad \text{for} \quad i = 1 \cdots M, \tag{4.17b}$$

$$f_{1,j} - 2\psi_j = 0, \qquad \text{for} \quad j = 1 \cdots N, \tag{4.17c}$$

$$f_{i,1} = 0, \qquad \text{for} \quad i = 1 \cdots A+1, \tag{4.17d}$$

$$q_{i,1} \frac{\partial q_{i,1}}{\partial \phi} - \frac{1}{2F^2} \frac{\partial f_{i,1}}{\partial \psi} + \frac{1}{\alpha} \frac{\partial \kappa_{i,1}}{\partial \phi} = 0, \qquad \text{for} \quad i = A+2 \cdots M, \tag{4.17e}$$

where terms like $\kappa_{i,1}$ refer to values of the curvature (4.7) computed at the meshpoint (ϕ_i, ψ_1). All the derivatives (f_s, f_t etc.) are approximated using second-order central difference formula or, when necessity dictates, second order one-sided formula. We then use formula such as (4.13a)-(4.13b) to obtain values of f_ψ, $f_{\psi\psi}$ (etc.) at each meshpoint. We note that these formula cannot be used for derivatives where $s = 0$ or $t = 0$. In such cases, we approximate the derivatives directly in ϕ and ψ. This system of MN equations can be solved for the MN unknowns using Newton's method. We terminate the iterations in Newton's method once the L^∞-norm of the residuals (values on the right-hand side of equations (4.17a-e)) is of order 10^{-11}. Once we have obtained values of $f_{i,j}$ for all (i, j), we can obtain values of $x_{i,j}$ by integrating (4.4) along lines of constant ψ. This is given by

$$x_{i+1,j} = x_{i,j} + \frac{1}{2}\int_{\phi_i}^{\phi_{i+1}} \frac{\partial f}{\partial \psi}(\phi, \psi_j)\,\mathrm{d}\phi. \tag{4.18}$$

The above integral is approximated via the trapezoidal rule.

4.3.1 Singularity removal: smooth bubbles

It is found that singularities, when not properly accounted for, cause inaccuracies to the approximation of derivatives in finite difference schemes (see Woods [95] and appendix A). In particular, as mesh spacing is decreased, the inaccuracies grow and the method fails to converge in the limit as mesh spacing goes to zero. In our case, we must remove the singularity associated with the stagnation point at the apex of the bubble $\phi = \psi = 0$. Woods [95] derived a function splitting procedure to regulate singularities in finite difference methods, paying particular attention to Poisson's equation. We follow a similar strategy, but with some modifications. In particular, while Woods performs the function splitting to the differential operator of the governing equation as a whole, we instead use the method on individual partial derivatives, due to the nonlinearity of equation (4.5).

The basic procedure to regulate the singularity is to first consider some function $f = \chi(\phi, \psi)$ which has the same singular behaviour as our flow at the singularity

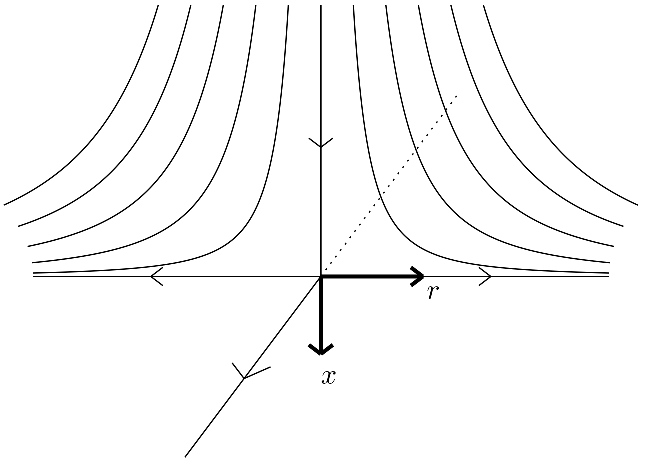

Figure 4.2: Axisymmetric flow onto a plate parallel with the r-axis. Some streamlines are shown.

and satisfies the governing equation. A natural choice is the flow onto an infinite flat plate (see Figure 4.2). The velocity potential and streamfunction of this flow are found to be

$$\phi = B\left(\frac{1}{2}f - x^2\right), \qquad \psi = -Bfx, \tag{4.19}$$

where B is an arbitrary positive constant. This can be re-arranged to remove x, producing a cubic for f. The unique real positive root of this cubic, $\chi = f$, is given by

$$\begin{aligned}\chi = \frac{2}{3B}\phi &+ \frac{1}{B^{2/3}}\left(A\phi^3 + \psi^2 + \psi\sqrt{2A\phi^3 + \psi^2}\right)^{1/3} \\ &+ \frac{1}{B^{2/3}}\left(A\phi^3 + \psi^2 - \psi\sqrt{2A\phi^3 + \psi^2}\right)^{1/3},\end{aligned} \tag{4.20}$$

where $A = 8/(27B)$. This function can be differentiated to analytically compute values of χ_ϕ (etc.) everywhere in the flow domain. The unknown constant B can be used to match the flow configuration in figure 4.2 to our problem by satisfying

$$\chi(\phi_i, \psi_j) - f(\phi_i, \psi_j) = 0, \tag{4.21}$$

for some meshpoint (ϕ_i, ψ_j) in the flow close to the singularity. A natural choice is to use the meshpoint on the free surface immediately after the apex, $(\phi_{A+2}, \psi_1) = (h^2, 0)$. This gives rise to

$$B = 2\frac{\phi_{A+2}}{f_{A+2,1}}. \tag{4.22}$$

Approximating the value of the constant B in this manner results in numerical errors, as explained in appendix A. We then re-write our solution f as

$$f(\phi, \psi) = (f - \chi) + \chi. \tag{4.23}$$

The motivation for subtracting and adding χ is now we can numerically compute derivatives on the function $(f - \chi)$ and analytically compute the derivatives of χ. Hence, in our code, the values of $\partial f_{i,j}/\partial\phi$ are computed as

$$\frac{\partial f_{i,j}}{\partial \phi} = \delta_\phi(f_{i,j} - \chi_{i,j}) + \frac{\partial \chi_{i,j}}{\partial \phi}, \tag{4.24}$$

where δ_ϕ is some finite difference approximation of the derivative. Since χ has been defined such that it has the same behaviour of f at the stagnation point, subtracting χ from f removes the leading order singularity, allowing us to approximate derivatives of $(f - \chi)$ via finite differences. Furthermore, since we have an explicit formula (4.20) for χ, computing derivatives (for example, $\partial\chi_{i,j}/\partial\phi$) is possible analytically. Therefore, (4.24) can be used to approximate derivatives at all meshpoints. We note that this would not work on a nonlinear differential operator, say $(\partial f_{i,j}/\partial\phi)^2$, since in this case

$$\left[\frac{\partial(f_{i,j} - \chi_{i,j} + \chi_{i,j})}{\partial\phi}\right]^2 \neq \left[\frac{\partial(f_{i,j} - \chi_{i,j})}{\partial\phi}\right]^2 + \frac{\partial\chi_{i,j}}{\partial\phi}^2. \tag{4.25}$$

However, one can simply apply (4.24), and then square the result to obtain the required value. Brennen [16] followed a similar method to remove a stagnation point singularity in a successive relaxation scheme used to compute axisymmetric cavitating flow past an obstruction in a tunnel. He solved the same governing equation (4.5) but with different boundary conditions. He approximated the front stagnation point using non-cavitating flow past a disc or sphere. However, he treated the governing equation as though it were linear as an approximation. Although this dramatically reduces computational time and requirements on storage (you can avoid computing terms like $\partial\chi_{i,j}/\partial\phi$ at all interior meshpoints, since χ is chosen to satisfy the governing equation), in our computations, such an approximation is unnecessary.

Special care must be taken when computing the integral (4.18) through the stagnation point. For example, consider the case where $i = A$ and $j = 1$, such that the integral is on the streamline $\psi = 0$, from the point $\phi_A = -h^2$ to $\phi_{A+1} = 0$. If we attempt to approximate the integral using the trapezoidal rule, taking into account (4.24), we obtain

$$\int_{-h^2}^{0} \frac{\partial f}{\partial \psi}\,\mathrm{d}\phi \approx \frac{h^2}{2}\left[\delta_\psi(f_{A+1,1}-\chi_{A+1,1}) + \delta_\psi(f_{A,1}-\chi_{A,1}) + \frac{\partial \chi_{A+1,1}}{\partial\psi} + \frac{\partial\chi_{A,1}}{\partial\psi}\right].$$

However, the value of $\partial\chi_{A+1,1}/\partial\psi$ is singular. Instead of directly applying the trapezoidal rule, we must integrate the $\partial\chi/\partial\psi$ term explicitly, that is

$$\int_{-h^2}^{0} \frac{\partial f}{\partial \psi}\,\mathrm{d}\phi \approx \frac{h^2}{2}\left[\delta_\psi(f_{A+1,1}-\chi_{A+1,1}) + \delta_\psi(f_{A,1}-\chi_{A,1})\right] + \int_{-h^2}^{0}\frac{\partial\chi}{\partial\psi}\,\mathrm{d}\phi, \tag{4.26}$$

where the second term is an integral calculated analytically. For the above equation, one finds that

$$\int_{-h^2}^{0}\frac{\partial\chi}{\partial\psi}\,\mathrm{d}\phi = \frac{4}{\sqrt{3B}}\sin(\pi/3)h. \tag{4.27}$$

The same consideration must be made when integrating from $\phi_{A+1} = 0$ to $\phi_{A+2} = h^2$ for $\psi = 0$.

It is of interest to note that Vanden-Broeck [83] constructed a similar finite difference scheme for this problem, taking r as a function of the independent variables

(x, ψ). However, the method took no measure to regulate the singularity at the stagnation point. Repeating the numerical scheme, we found the results were satisfactory for crude meshes, but ultimately the method diverges with mesh refinement. On the other hand, we found the new numerical scheme described above convergent upon mesh refinement, at least as far as computationally practical, as shown in section 4.4.

As another check on our numerical scheme, we also constructed a finite difference scheme to compute plane bubbles. The details are omitted here, but it closely follows the method for the axisymmetric bubble, where we instead seek y as a function of the unknowns (ϕ, ψ) (see figure 3.2). We also removed the stagnation point singularity by using the function splitting method. In this case, the local behaviour is given by equation (3.9) with $\mu = \pi/2$, which can be written as

$$y = \chi(\phi, \psi) = \Im\Big\{\frac{i}{B}\sqrt{\phi + i\psi}\Big\}. \tag{4.28}$$

The results were found to be in good agreement with the results of chapter 3, as shown in the following section.

4.4 Results for smooth Taylor bubbles

The above method was used to compute solutions to both plane and axisymmetric bubbles with and without surface tension. Some profiles of axisymmetric $\alpha^{-1} = 0$ solutions are shown in figure 4.3 . As shown in figure 4.4, as we approach $F = F_C$, the radius of curvature of the streamline becomes very small at the apex of the bubble (resulting in large values of the curvature). Since the $F = F_C$ solution is a pointed bubble with infinite curvature at the apex (computed in section 4.5), the constant B associated with the corner singularity (4.20) is singular in the limit $F \to F_C$. This made smooth bubbles with values of F close to $F = F_C$ difficult to compute. We

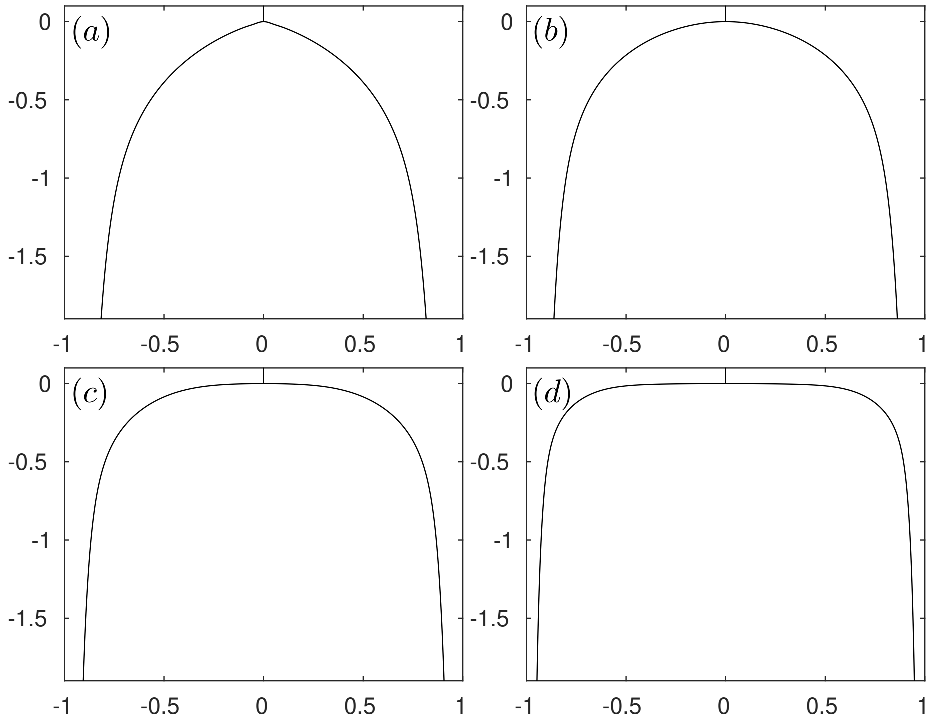

Figure 4.3: Various profiles of axisymmetric bubbles for $\alpha^{-1} = 0$, with Froude numbers (a) $F = 0.65$, (b) $F = 0.5$, (c) $F = 0.35$ and (d) $F = 0.2$.

found that we required higher than double precision when computing these solutions in order for iterations in Newton's method to convergence. This was done using MATLAB and the mp toolkit [2].

For the case of non-zero surface tension, we computed the first three solution branches $F_1(\alpha), F_2(\alpha)$ and $F_3(\alpha)$. When computing along solution branches, it is of significant importance that we are able to fix either F or α, and allow the other parameter to vary. In general, we found it more convenient to fix α. Since there is now one additional unknown, we must introduce a new equation such that our discrete system is not ill-posed. We impose a four-point interpolation formula on the curvature of the free surface, given by

$$\kappa_{L,1} - 3\kappa_{L+1,1} + 3\kappa_{L+2,1} - \kappa_{L+3,1} = 0, \tag{4.29}$$

where $L > A + 1$ is an integer such that $\phi_L > 0$. The motivation for using equation (4.29) is that, for a small range of values of F around the solution branches $F_i(\alpha)$,

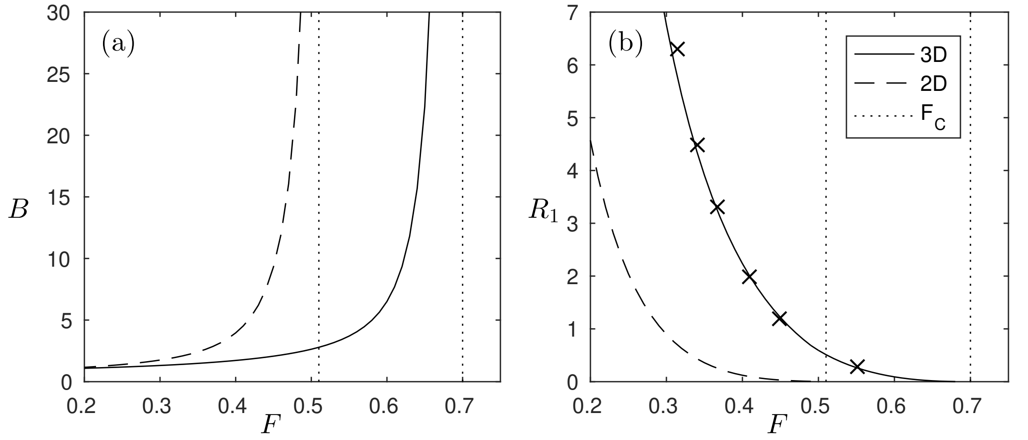

Figure 4.4: Figure (a) is a plot of the value of the constant B given in (4.28) for the plane bubble and the constant B in (4.20) for the axisymmetric bubble as a function of the Froude number F, where $\alpha^{-1} = 0$. As the solution branch approaches $F = F_C$, the curvature at the apex becomes large and the value of $B \to \infty$. This is shown in figure (b), where the radius of curvature of the streamline at the apex of the bubble, R_1, goes to zero as $F \to F_C$. The crosses show values obtained by Levine and Yang [57].

the method converges on unrealistic solutions with erratic curvature values. The range of values of F decreases as the mesh spacing is reduced. Alternatively, we occasionally fixed both α and F and manually moved through the solution space. This method was particularly useful when trying to obtain the first solution on a solution branch F_i. Once on the solution branch, the code with varying F was used to compute solutions close to the one already obtained on the branch, using the previous solution as an initial guess. The first three solutions branches for the plane and axisymmetric bubbles are shown in figure 4.5. The branch F_1 approaches F^*. For higher order branches, the numerical scheme fails to produce unique results for values of α larger than shown in figure 4.5. Fixing both α and F, it is found the numerical scheme converges for all F in this region. This is true for both the two-dimensional and axisymmetric problem. In figure 4.6, we show an enlarged plot of the limiting behaviour of the higher order branches for plane bubbles, computed using the series truncation method described in chapter 3. Solutions computed using the series truncation method are very accurate, since, through the use of conformal mapping techniques, the numerical scheme is reduced to a one-dimensional problem.

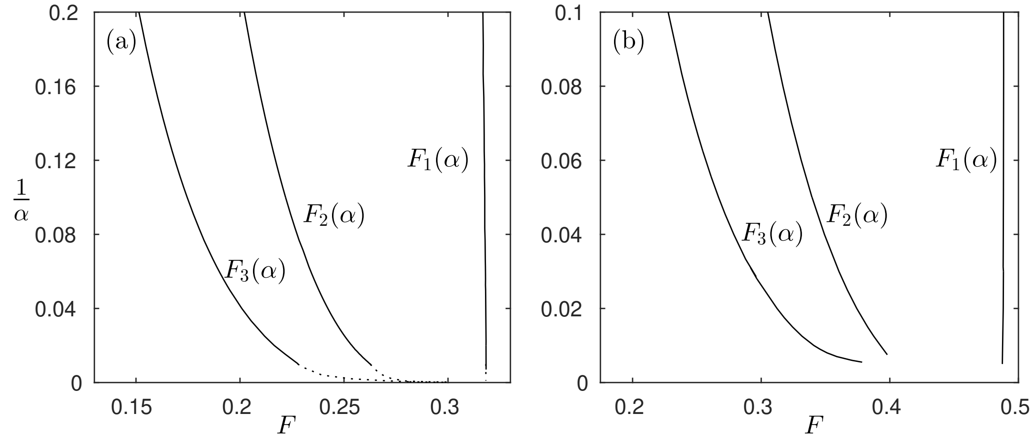

Figure 4.5: The first three branches F_1, F_2 and F_3 for the 2D (figure (a)) and axisymmetric (figure (b)) bubbles. The dotted lines in figure 4.5(a) were computed using a series truncation method (see chapter 3).

This allows computations with thousands of meshpoints on the free surface. We conjecture that the higher order branches of the axisymmetric bubbles have the same limiting behaviour, but a computationally less expensive numerical procedure would be required to compute solutions in this region. A plot of the selected axisymmetric solution F^* is shown in figure 4.7. This solution is compared with the experimental results of Davies and Taylor [26] in figure 4.8. It can be seen that the selected solution agrees with the experimental bubble near the stagnation point (the nose of the bubble). However, the curves deviate as we move further downstream. This is due to the fact that in our model we ignore viscosity, and instead balance the increasing gravitational potential with inertia. Approximating the far-field downstream as an infinitesimal jet is a mathematical simplification, justified by the fact that it has been seen in experiments that the bubble length has minimal effect on the nose of the bubble (for example, see Viana et al. [91]). This explains the weaker agreement between the numerical solution and the experimental bubble downstream.

An interesting property of solutions on the higher mode solution branches is that they develop oscillations on the free surface. Figures 4.9 and 4.10 show solutions from the first four modes for a given α for plane and axisymmetric bubbles respectively. Each odd mode F_{2n-1} has a peak at the apex followed by $n-1$ peaks and troughs,

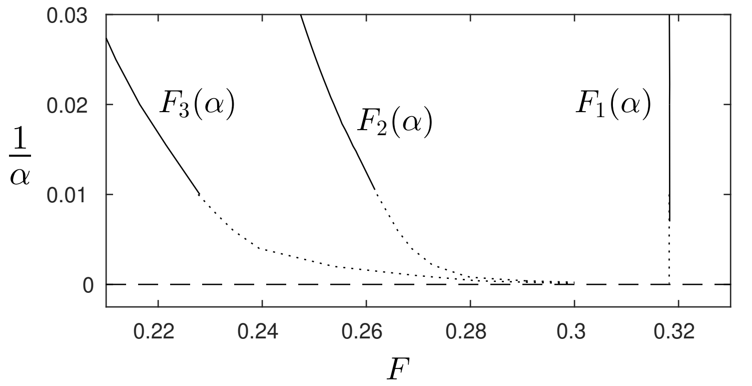

Figure 4.6: A blow up of figure 4.5(a), showing the limiting behaviour of the solution branches $F_i(\alpha)$ for plane bubbles.

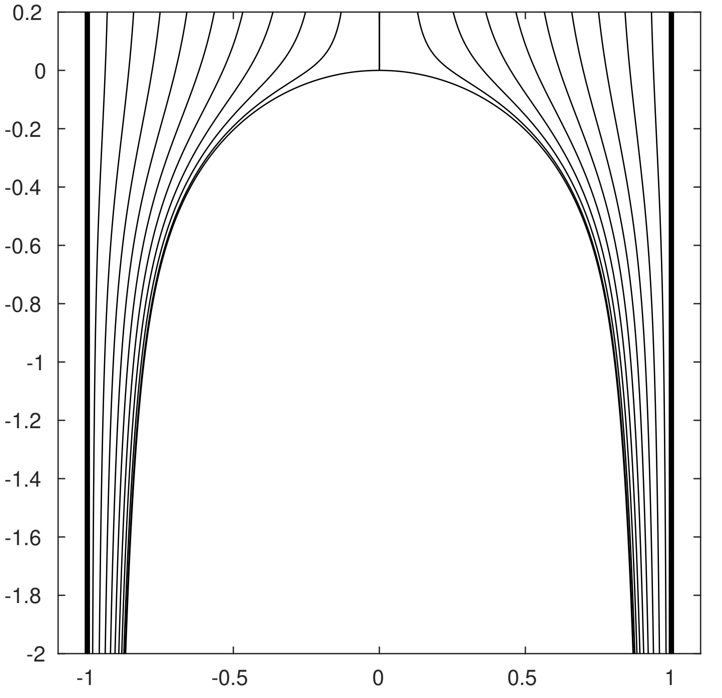

Figure 4.7: The selected axisymmetric solution $F^* = 0.49$, plotted to scale. Some streamlines are shown to demonstrate the flow field.

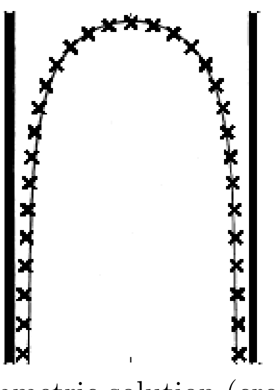

Figure 4.8: The selected axisymmetric solution (crosses) compared with the bubble in figure 9 of Davies and Taylor [26] (solid curve).

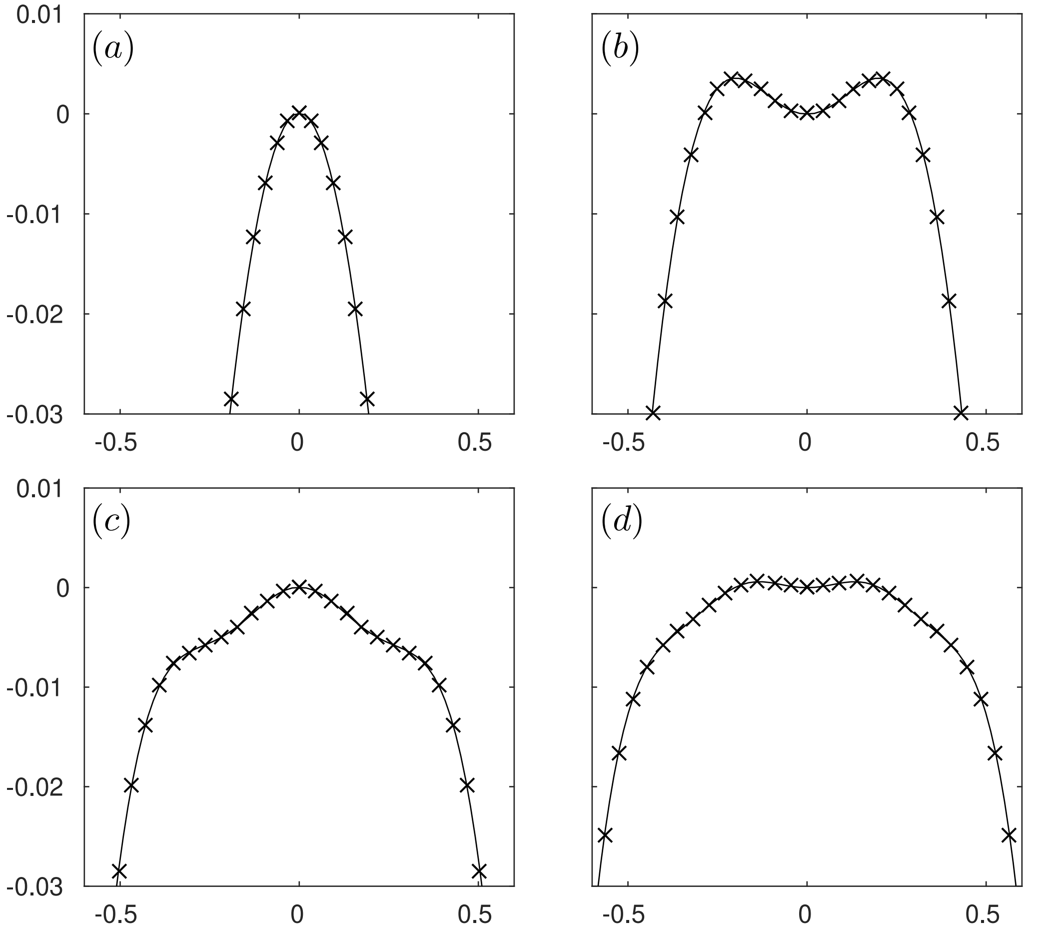

Figure 4.9: Profiles of smooth plane bubbles from the first four solution branches. The vertical scale has been exaggerated to show the oscillations clearly, and is the same for each figure. Every solution is given by $\alpha = 5$, and the values of F are (a) $F_1(5) = 0.316$, (b) $F_2(5) = 0.202$, (c) $F_3(5) = 0.151$ and (d) $F_4(5) = 0.122$. The crosses are computed using the series truncation method from chapter 3. There is good agreement with the results obtained using the finite difference scheme.

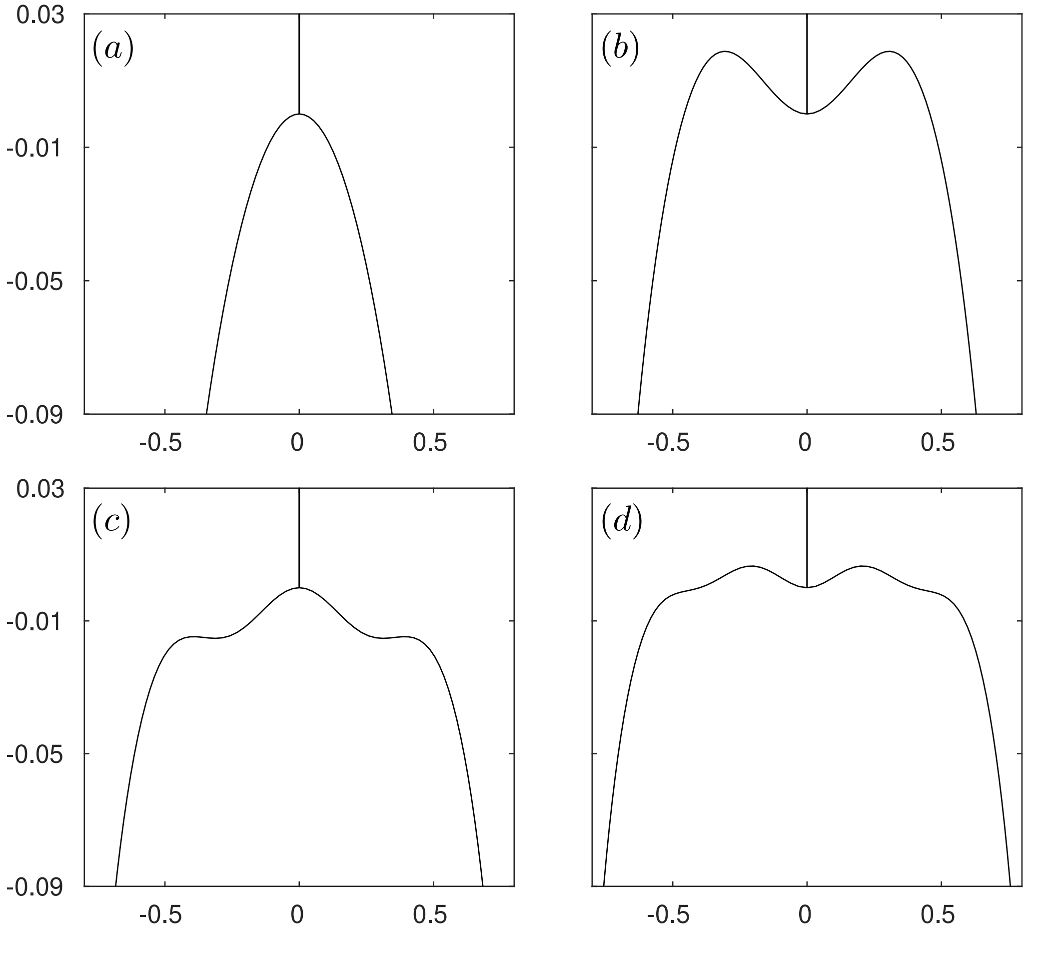

Figure 4.10: Profiles of axisymmetric Taylor bubbles from the first four solution branches. The vertical scale has been exaggerated to show the oscillations clearly, and is the same for each figure. Every solution is given by $\alpha = 10$, and the values of F are (a) $F_1(10) = 0.488$, (b) $F_2(10) = 0.305$, (c) $F_3(10) = 0.228$ and (d) $F_4(10) = 0.183$.

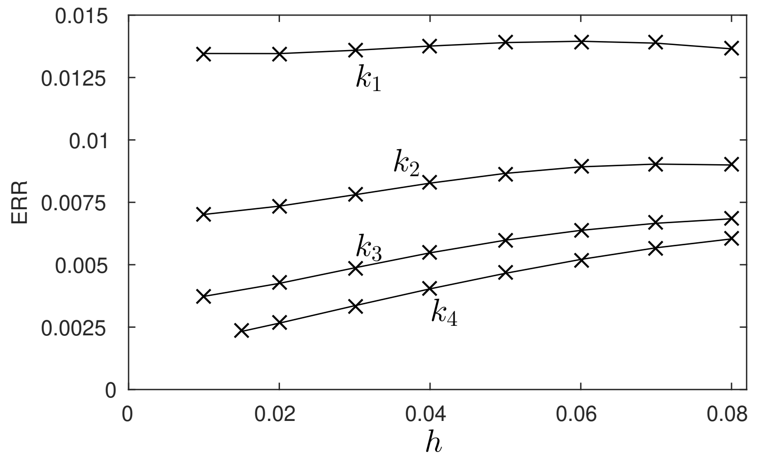

Figure 4.11: Plot of the relative errors in the value of B for the $F = 0.3$ plane bubble with zero surface tension for various mesh sizes. Denoting B_n the value obtained by the numerical scheme, the relative error is defined as ERR= $|B_e - B_n|/B_e$, where B_e is the value obtained using the series truncation method. The curves are lines of constant k, where the values of k are $k_1 = 0.04$, $k_2 = 0.02$, $k_3 = 0.01$, and $k_4 = 0.005$.

while each even mode F_{2n} has a trough at the apex, followed by n peaks and $n-1$ troughs. Such behaviour was commented on by Levine and Yang [57], who computed some higher mode solutions for larger values of the surface tension.

There are two main sources of error in the method: the approximation of derivatives via finite differences, and the truncation of the previously infinite flow domain Ω_ϕ. The error from domain truncation can be made negligible by taking ϕ_1 and ϕ_2 from (4.15) suitably large. For example, consider the axisymmetric bubble with zero surface tension and $F = 0.34$, computed with mesh spacing $h = 0.02$ and $k = 1/(60\sqrt{2})$, where h and k are defined in equation (4.16). Comparing the solution obtained with $\phi_1 \approx 4$, $\phi_2 \approx 20$ (denote $f = f_1(\phi,\psi)$) and $\phi_1 \approx 5$, $\phi_2 \approx 25$ (denote $f_2(\phi,\psi)$), we find that $L^\infty|f_1 - f_2| < 10^{-13}$.

All finite differences are computed using second order difference equations in both h and k. However, one may expect additional sources of error when approximating derivatives due to the function splitting procedure discussed in section 4.3.1. As an example, the computation of B in equation (4.22) is an approximation of the 'true' value of B. Appendix A explores the order of errors seen when approximating singular derivatives with difference equations, and how the function splitting method

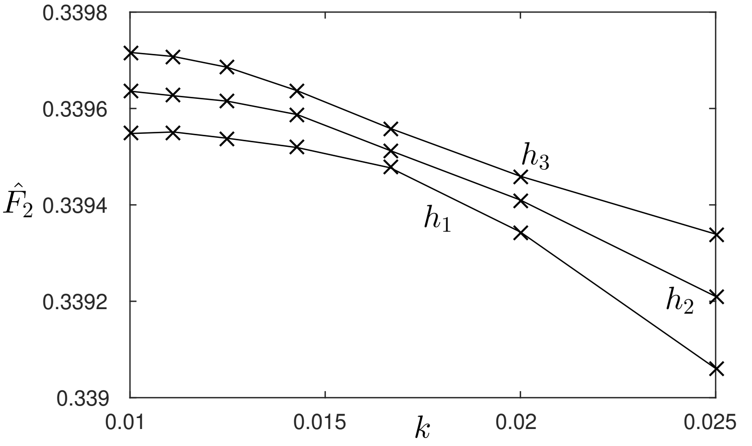

Figure 4.12: Values obtained for $F_2(20) = \widehat{F_2}$ for the axisymmetric bubble . The curves are lines of constant h, where the values of h are $h_1 = 0.02$, $h_2 = 0.01732$, and $h_3 = 0.015$.

regulates such errors, for the simplified case of a function of one variable. At the end of the appendix, we discuss the difficulties with extending the theory to multiple variables. Despite this, we are optimistic with the success of the method as applied here. In figure 4.11, we compare values of B (see equation (4.28)) for the $\alpha^{-1} = 0$, $F = 0.3$ plane bubble obtained using the series truncation with the value computed using the finite difference scheme for various h and k. We see that, for fixed k, the method appears to be close to first order accurate in h (the lines are approximately linear). Meanwhile, for fixed h, the method is somewhere between first and second order convergent in k. In figure 4.12, we compare values of $F_2(20)$ obtained for different values of h and k for the axisymmetric bubbles, demonstrating convergence of the numerical method. As an additional check on the method, we also highlight the very good agreement between the profiles obtained by the series truncation method and the finite difference scheme in figure 4.9, and the results obtained by the boundary integral scheme of Levine and Yang [57] for the axisymmetric bubbles, as seen in figure 4.4b.

4.5 Pointed $F = F_C$ bubble

We stated in chapter 3 that, for plane bubbles with zero surface tension, there are only three possible values of μ such that equation (4.3) is locally satisfied near the crest of the bubble. Milewski et al. [63] performed a local analysis near the crest of an axisymmetric solution, and found that the same is true for axisymmetric bubbles. The three possible values are $\mu \in \{0, \Theta, \pi\}$, where Θ satisfies $P'_{3/2}(\cos\Theta) = 0$. Here, $P_{3/2}$ is the Legendre function of degree 3/2 and order 0, and hence we find that $\Theta \approx 115^0$.

As described in the previous section, in the case of zero surface tension, as $F \to F_C$, the curvature of the smooth bubbles at the apex becomes singular (see figure 4.4b). From previous works, we know that for plane bubbles, the $F = F_C$ solution is a pointed bubble with interior angle $\mu = 2\pi/3$. It was believed that the $F = F_C$ axisymmetric bubble has the local behaviour as described in Milewski et al. [63]. We confirm this is true, and now present a numerical method to compute the axisymmetric $F = F_C$ solution.

Garabedian [42] derived a velocity potential describing the behaviour at the crest of the $F = F_C$ solution. The streamfunction can be found using relations (4.1), and is given by

$$\psi = Br^2(x^2 + r^2)^{1/4} \times \left\{ {}_2F_1 \left[-\frac{1}{2}, \frac{7}{2}, 2, \frac{1}{2} \left(1 + \frac{x}{(x^2 + y^2)^{1/2}} \right) \right] \right\}, \tag{4.30}$$

where ${}_2F_1$ is the Gaussian hypergeometric function, and B is an arbitrary positive constant. A plot of some streamlines for $B = 1$ is shown in figure 4.13.

Vanden-Broeck [83] constructed a finite difference scheme with r as an unknown function of the independent variables (x, ψ). The flow domain in the (x, ψ) space is an infinite strip $\Omega_x = \{\psi \in [0, 1/2], -\infty < x < \infty\}$, and can be discritised in a similar manner to Ω_ϕ in section 4.3. We again perform coordinate transforms (4.12a-

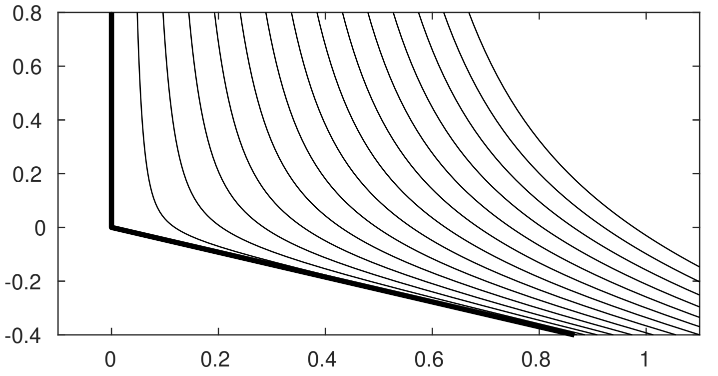

Figure 4.13: Plots of streamlines given by (4.30)

b), replacing ϕ with x in (4.12a). We then discretise Ω_x with M points in α and N points in t using equations (4.14). The governing equation, when formulated this way, is given by

$$r_{\psi\psi}\left(1+r_x^2\right)+r_\psi^2\left(r_{xx}+\frac{1}{r}\right)-2r_xr_\psi r_{x\psi}=0, \tag{4.31}$$

while Bernoilli's equation yields

$$\left(1+r_x^2\right)\left(rr_\psi\right)^{-2}-\frac{2}{F^2}x=0. \tag{4.32}$$

Using these equations, we construct a discrete system of MN equations similar to the system (4.17a-e). Vanden-Broeck failed to account for the singularity in the flow field, resulting in divergence of the numerical method as the mesh is refined. We rectify this problem by making use of Garabedian's solution (4.30). Like in 4.3.1, we desire to find a solution $r(x,\psi)=\chi(x,\psi)$ which matches the singular behaviour of the bubble at the apex. Equation (4.30) is a transcendental equation for the unknown r given a fixed point in the (x,ψ) space. This can be solved at each meshpoint using Newton's method to find χ. Equations for χ_ψ, χ_x, $\chi_{\psi\psi}$, χ_{xx}, and $\chi_{x\psi}$ can be obtained by differentiating (4.30) and making use of

$$r_\psi=\psi_r^{-1}, \tag{4.33a}$$

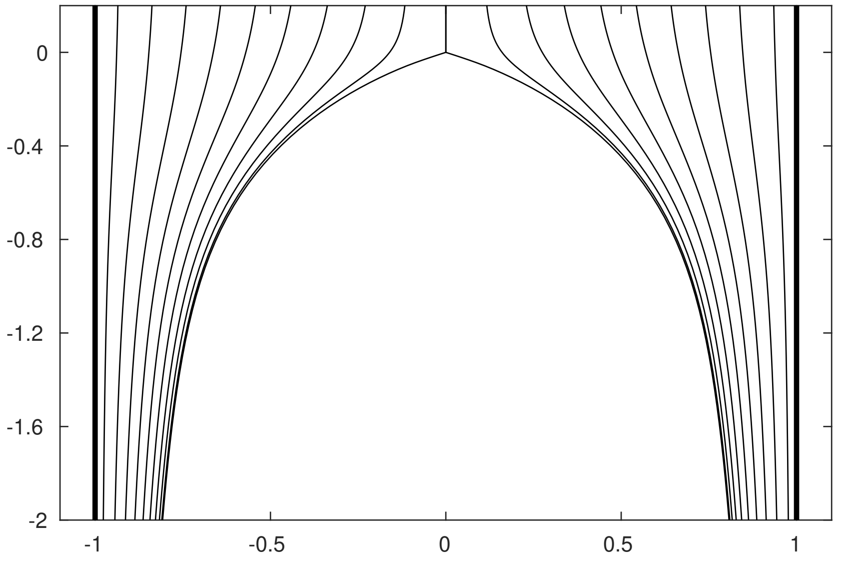

Figure 4.14: Axisymmetric zero surface tension solution for $F = F_C \approx 0.70$. Some streamlines are shown to demonstrate the flow field.

$$r_{\psi\psi} = \psi_r^{-3}\psi_{rr}, \tag{4.33b}$$

$$r_x = -\psi_x\psi_r^{-1}, \tag{4.33c}$$

$$r_{x\psi} = \left(r_x r_{\psi\psi} - \psi_{rx} r_\psi^3\right) r_\psi^{-1}, \tag{4.33d}$$

$$r_{xx} = \left(2r_x r_\psi r_{x\psi} - r_x^2 r_{\psi\psi} - \psi_{xx} r_\psi^3\right) r_\psi^{-2}. \tag{4.33e}$$

Therefore, we have all the required components to remove the singularity via the same method described in section 4.3.1. This allows us to compute the pointed bubble solution. A profile of the solution is given in figure 4.14. It is found that $F_C \approx 0.7$, as in agreement with figure 4.5. No solutions for other values of F were found with this method, suggesting that $F = F_C$ is the only value of the Froude number for which zero surface tension axisymmetric bubbles are pointed with the singular behaviour (4.30) at the apex. As we saw in chapter 3, two-dimensional Taylor bubbles with $F > F_C$ have cusps at the apex. We were unable to obtain cusped axisymmetric bubbles since no suitable treatment of the cusp singularity was found. This is briefly discussed in chapter 6.

4.6 Conclusion

In conclusion, we have presented a numerical scheme capable of computing both plane and axisymmetric Taylor bubbles. The method used produces results in good agreement with previous authors. Two of the higher order smooth solution branches, $F_2(\alpha)$ and $F_3(\alpha)$, have been computed for small values of surface tension. Although we are unable to capture the limiting behaviour of the higher order branches as $\alpha^{-1} \to 0$, similarities in the solution spaces of the two-dimensional and axisymmetric problems, combined with the knowledge of the limiting behaviour of the two-dimensional solution branches, provides numerical evidence to suggest the axisymmetric branches approach F^* in the limit as $\alpha^{-1} \to 0$. We used the velocity potential derived by Garabedian [42], combined with the singularity removal procedure, to compute the zero-surface tension $F = F_C$ axisymmetric bubble, characterised by an interior angle of approximately 130^0. This was the only value of F for which a pointed $T = 0$ solution was found, further strengthening the similarities between the two-dimensional and axisymmetric solution spaces.

In the following chapter, we investigate waves propagating on a ferrofluid jet.

Chapter 5

Steady waves on an axisymmetric ferrofluid jet

In this chapter, we will consider a modification of the classical Plateau-Rayleigh instability. The instability is suppressed with the use of ferrofluids, as described below. The results of this chapter can be found in Doak and Vanden-Broeck [33].

5.1 Introduction

Since the work of Rayleigh [73], it has been known that capillary jets (axisymmetric columns of fluid in which gravity is ignored) are unstable to linear perturbations of wavelength longer than that of the circumference of the jet. This instability, referred to as the Plateau-Rayleigh instability, causes a capillary jet to break into droplets, and removes the possibility of the existence of steady solitary wave solutions. The steady solutions that do exist, that is periodic waves with wavelength shorter than the circumference of the jet, were computed numerically by Vanden-Broeck et al. [90]. These waves, similar to the two-dimensional capillary waves found analytically by Crapper [23] for the case of infinite depth and Kinnersley [53] for finite depth, form overhanging structures as the amplitude increases, until finally a limiting configuration with a trapped bubble is formed. Alternatively, the solution branches can terminate on a non-trivial static configuration, where there is no motion in the fluid.

Ferrofluids are fluids containing nanoparticles of ferromagnetic material coated in molecular surfactant, resulting in the fluid having superparamagnetic behaviour. Ferrofluids are used in a variety of industrial applications, such as measuring the acceleration and inclination of oil drills, and sealing pump shafts (Raj et al. [71]). Since the analytic work and experiments of Bashtovoi and Krakov [8] and Arkhipenko et al. [6], it has been known that magnetic fields can stabilize the Plateau-Rayleigh instability when considering a column of ferrofluid. This is done by coating a copper wire with ferrofluid and passing a current through the wire, inducing an azimuthal magnetic field. The buoyancy effects are suppressed by surrounding the ferrofluid in a non-magnetizable fluid of equal density. The problem is characterised by a magnetic Bond number B, defined in section 5.2, which comes from a ratio of magnetic to capillary forces. Arkhipenko et al. [6] show that when $B > 1$, the Rayleigh-Plateau instability is stabilized for all wavelengths. This formulation is of particular interest since it allows for axisymmetric solitary wave solutions.

We consider two models. In the first model, which we shall call the one-layer model, we assume the surrounding non-magnetizable fluid has negligible density. In the second model, named the two-layer model, we consider a surrounding fluid of density equal to that of the ferrofluid. It is helpful to draw comparisons between the models discussed here and the classical problem of two-dimensional gravity-capillary free surface and interfacial waves. It is found there are many similarities, and some interesting differences, between these dispersive water wave systems. Reviews of two-dimensional gravity-capillary waves can be found in Dias and Kharif [27] and Vanden-Broeck [87]. We note that our model allows for variable density ratios of the two fluids. However, a ratio of unity is of particular interest since, as stated above, gravity free regimes can be experimentally realised this way. This was done recently by Bourdin et al. [15], where the surrounding fluid was taken to be freeon of almost equal density to that of the ferrofluid. Axisymmetric periodic and solitary waves were observed.

So far most analytic and numerical work on the problem has considered only the one-layer model. Under the assumption that the radius of the copper wire (denoted d) is negligible, Rannacher and Engel [72] derived a Kortewegde Vries (KdV) equation to describe weakly nonlinear solitary waves. Like the KdV equation for gravity-capillary waves, it is found that for some critical values of the parameters, the coefficient of the dispersive term changes sign (Korteweg and de Vries [55]; Benjamin [10]; Hunter and Vanden-Broeck [50]). For the ferromagnetic problem, we shall denote this critical value as $B = B_2$. However, unlike gravity-capillary waves, there is also a change in sign of the coefficient of the nonlinear term at $B = B_1 < B_2$. The implication is that the KdV equation predicts depression solitary waves in the region $B \in (B_1, B_2)$, and elevation waves for $B \in (1, B_1)$ and $B > B_2$.

Blyth and Părău [13] (referred to as BP thoughout) performed a numerical investigation of solitary wave solutions to the one-layer model in the fully nonlinear regime for arbitrary values of d. They found that, for $1 < B < B_1(d)$, solitary waves bifurcating from zero amplitude are elevation waves, while for $B_1(d) < B < B_2(d)$ these solutions are depression waves. This is in good agreement with Rannacher & Engel's KdV equation, who found $B_1 = 3/2$ and $B_2 = 9$ when $d = 0$. Time dependent computations on solutions of this type, based upon Taylor series expansions of Dirichlet to Neumann operators, are considered by Guyenne and Părău [47]. Furthermore, BP also found branches of depression solitary waves bifurcating from non-zero amplitude for $1 < B < B_1$, and likewise elevation solitary waves bifurcating from non-zero amplitude for $B_1 < B \leq 2$. This is rather surprising, since such bifurcations have not been found for two-dimensional gravity-capillary waves.

For $B < B_2$, the linear dispersion relation $c(k)$ is monotonic increasing, where c is the wavespeed and k the wavenumber. When $B > B_2$, a minimum appears. BP found no pure solitary waves (waves with monotonic decay in the far-field) in this regime. They instead found solitary wave packets, which bifurcate from the minimum of the dispersion relation. These waves are described at small amplitude by a Nonlinear Schrödinger Equation, recently derived by Groves and Nilsson [45] for the one-layer model under the assumption that $d = 0$. Groves and Nilsson also proved the existence of a variety of solitary wave solutions for this model. When there is a minimum, as well as solitary wave packets, one also expects to find generalised solitary waves. These are solitary waves characterised by a wave-train of ripples in the far-field. Such solutions have been found for gravity-capillary waves (for example, Hunter and Vanden-Broeck [50]). In this chapter, we compute numerically solutions of this type for the ferrofluid jet. It is found that, for all parameter values tested, the far-field of the solution is never flat along the branches of generalised solitary waves. This is checked by showing that the values of the curvature of the streamlines are non-zero in the far-field. This was found to be the case for two-dimensional gravity-capillary waves in the numerical investigation of Champneys et al. [20], and for hydroelastic waves by Gao and Vanden-Broeck [37]. Since no pure solitary waves are found when $B > B_2$, the KdV equation does not accurately predict the behaviour of nonlinear solutions in this regime.

In this chapter, we extend the numerical investigation of BP by computing generalised solitary waves and periodic waves for the one-layer model. Furthermore, we adapt the numerical method to allow for two flow domains, and compute solutions for the two-layer model. Steady periodic, solitary and generalised solitary wave solutions are found.

The chapter is organised as follows. In section 5.2, we formulate the problem. In section 5.3, we derive the linear dispersion relation for the problem. In section 5.4, we describe the numerical method used to compute solutions. In section 5.5, the range of possible static solutions ($c = 0$) is discussed. In section 5.6, the results of the numerical investigation are presented. Section 5.7 is a conclusion.

5.2 Formulation

We consider an axisymmetric column of ferrofluid with constant density ρ_1 and magnetic susceptibility χ_1, coating a copper rod of radius d. We choose the cylindrical coordinate system (x, θ, r) such that x points along the rod, r is the radial coordinate, and θ is the azimuthal coordinate. The ferrofluid is surrounded by a non-magnetisable fluid ($\chi_2 = 0$) of density ρ_2. The interface is given by $r = \eta(x, t)$, the mean radius of which is denoted R. Denote the velocity fields in the ferrofluid and surrounding fluid as $\boldsymbol{u_1} = (u_1, v_1)$ and $\boldsymbol{u_2} = (u_2, v_2)$ in (x, r) respectively. The system is contained inside a fixed cylindrical container of radius D (see figures 5.1 and 5.2). We note that in the experiments of Arkhipenko et al. [6] and Bourdin et al. [15], the fluids were contained in a rectangular box. However, since axisymmetric interfaces were witnessed, the box must have been of a sufficient size to not destroy the axisymmetry of the problem. Therefore, comparisons between the experiment and the model presented here can be made by considering large values of D. This is discussed further in section 5.7.

A current I is passed through the copper wire. This induces a purely azimuthal external magnetic field, given by

$$\boldsymbol{H}_{\text{ext}} = I/(2\pi r)\boldsymbol{e_\theta}, \tag{5.1}$$

where $\boldsymbol{e_\theta}$ is the unit vector in the clockwise azimuthal direction. We define the magnetic fields in the ferrofluid and the freon as $\boldsymbol{H_1}$ and $\boldsymbol{H_2}$ respectively. We assume the linear magnetization law, such that the magnetisation in each domain $\boldsymbol{M_i}$ satisfies $\boldsymbol{M_i} = \chi_i \boldsymbol{H_i}$. Since the freon is non-magnetisable, we have that $\boldsymbol{M_2} = 0$.

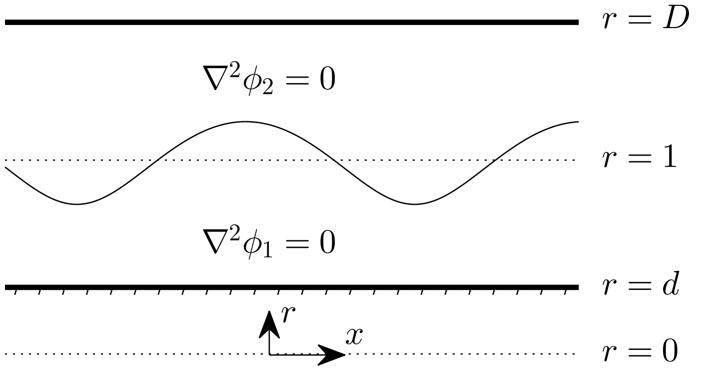

Figure 5.1: Formulation in cylindrical coordinates.

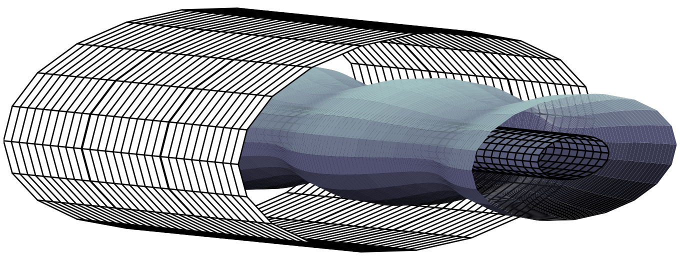

Figure 5.2: Three-dimensional visualization of the problem

The magnetic flux density $\boldsymbol{B_i}$ is given by

$$\boldsymbol{B_i} = \mu_0 \left(\boldsymbol{H_i} + \boldsymbol{M_i}\right) = \mu_0(1 + \chi_i)\boldsymbol{H_i}, \tag{5.2}$$

where μ_0 is the magnetic permeability of free space. Inside the ferrofluid, the ferromagnetic nanoparticles are too far apart to support electrical currents ([74] §3.1). Hence, we have that the magnetic field satisfies the magnetostatic equations with no current charge density (Rosensweig [74] §3.1). Therefore, Maxwell's equations state that

$$\nabla \times \boldsymbol{H_i} = 0, \qquad \nabla \cdot \boldsymbol{B_i} = 0. \tag{5.3}$$

Equations (5.2) and (5.3) imply that $\boldsymbol{H_i}$ is an irrotational and incompressible vector field. Hence, we can write $\boldsymbol{H_i} = -\nabla l_i$, where l_i is a scalar potential that satisfies Laplace's equation, given in this instance by

$$\nabla^2 l_i = \frac{\partial^2 l_i}{\partial r^2} + \frac{1}{r}\frac{\partial l_i}{\partial r} + \frac{\partial^2 l_i}{\partial z^2} + \frac{1}{r^2}\frac{\partial^2 l_i}{\partial \theta^2} = 0. \tag{5.4}$$

Consider a boundary between two mediums. Denote the values of $\boldsymbol{H}$ on either side of the boundary as $\boldsymbol{H_a}$ and $\boldsymbol{H_b}$ (and likewise for $\boldsymbol{B}$). Then the boundary conditions on $\boldsymbol{H}$ and $\boldsymbol{B}$ are given by (Rosensweig [74] §3.2)

$$(\boldsymbol{H_a} - \boldsymbol{H_b}) \times \widehat{\boldsymbol{n}} = 0, \qquad (\boldsymbol{B_a} - \boldsymbol{B_b}) \cdot \widehat{\boldsymbol{n}} = 0, \tag{5.5}$$

where $\widehat{\boldsymbol{n}}$ is the normal vector of the boundary. When the boundary is axisymmetric, we have that $\widehat{\boldsymbol{n}} = \widehat{\boldsymbol{e_r}}$, where $\widehat{\boldsymbol{e_r}}$ is the unit vector in the radial direction. Hence, under the assumption that the interface $r = \eta(x,t)$ is axisymmetric, the system of equations governing the magnetic fields becomes

$$\begin{aligned}
\nabla^2 l_1 &= 0, && \text{for} \quad d < r < \eta(x,t), && (5.6)\\
\nabla^2 l_2 &= 0, && \text{for} \quad \eta(x,t) < r < D, && (5.7)\\
l_1 &= -\frac{I\theta}{2\pi}, && \text{on} \quad r = d, && (5.8)\\
l_1 &= l_2, && \text{on} \quad r = \eta(x,t), && (5.9)\\
l_2 &= -\frac{I\theta}{2\pi}, && \text{on} \quad r = D. && (5.10)
\end{aligned}$$

This system has a solution, given by $l_1 = l_2 = -I\theta/2\pi$. The assumption of an axisymmetric interface has resulted in a decoupling of the magnetostatic problem from the hydrodynamical problem. The decoupling of Maxwell's equations is a dramatic simplification of the mathematics of the model.

The normal stress balance on an interface where one medium is magnetisable and the other is not (Rosensweig [74] §5.2) is given by

$$P_1 = P_2 + T\kappa - \frac{\mu_0}{2}\left(\boldsymbol{M_1} \cdot \widehat{\boldsymbol{n}}\right)^2. \tag{5.11}$$

Here, P_1 and P_2 are the pressures in the ferrofluid and outer fluid respectively, T the surface tension, and κ the mean curvature, given by

$$\kappa = \frac{1}{\eta}\left(1+\left(\frac{\partial \eta}{\partial x}\right)^2\right)^{-1/2} - \frac{\partial^2 \eta}{\partial x^2}\left(1+\left(\frac{\partial \eta}{\partial x}\right)^2\right)^{-3/2}. \tag{5.12}$$

Note that since $\boldsymbol{M_1}$ is azimuthal, the pressure jump associated with the magnetic field is zero.

We consider a wave of unchanging form with wavelength λ and celerity c. Under the assumption that the flows in either region are irrotational and incompressible, both velocity fields can be written in terms of a velocity potential $\boldsymbol{u_{1,2}} = \nabla\phi_{1,2}$, where ϕ_1 and ϕ_2 satisfy the Laplace equation:

$$\nabla^2\phi_i = 0, \qquad\qquad i = 1, 2, \tag{5.13}$$

in their respective flow domains. We assume the wave is symmetric about the point $\phi_1 = \phi_2 = 0$. We require no normal flow through the rod and outer cylinder, that is

$$\frac{\partial \phi_1}{\partial r} = 0 \qquad \text{for } r = d, \tag{5.14}$$

$$\frac{\partial \phi_2}{\partial r} = 0 \qquad \text{for } r = D. \tag{5.15}$$

The Bernoulli principle (Rosensweig [74] §5.2) satisfied on the interface gives

$$\frac{\partial \phi_1}{\partial t} - \rho\frac{\partial \phi_2}{\partial t} + \frac{1}{2}\left(q_1^2 - \rho q_2^2\right) + \frac{1}{\rho_1}\left(P_1 - P_2\right) - \frac{\mu_0\chi_1 I^2}{4\pi^2\rho_1}\frac{1}{2r^2} = \widehat{C}, \tag{5.16}$$

where $q_i = |\nabla\phi_i|$, $\rho = \rho_2/\rho_1$, and $\widehat{C}$ is the Bernoulli constant. We take R as the reference length and $\sqrt{T/(R\rho_1)}$ as the reference velocity. Making use of equation

(5.11), we find that the non-dimensionalised Bernoulli equation is

$$\frac{\partial \phi_1}{\partial t} - \rho \frac{\partial \phi_2}{\partial t} + \frac{1}{2}\left(q_1^2 - \rho q_2^2\right) + \kappa - \frac{B}{2r^2} = C, \tag{5.17}$$

where the magnetic Bond number B is defined as

$$B = \frac{\mu_0 \chi_1 I^2}{4\pi^2 RT}. \tag{5.18}$$

The magnetic Bond number is a ratio of magnetic to surface tension forces. It is shown in section 5.3 that the stability of linear perturbations is determined by B. Finally, the kinematic boundary condition on the interface is given by

$$\frac{\partial \eta}{\partial t} + \frac{\partial \eta}{\partial x}\frac{\partial \phi_i}{\partial x} = \frac{\partial \phi_i}{\partial r}, \qquad i = 1, 2. \tag{5.19}$$

Note that for solitary waves with a flat far-field, instead of fixing the mean of η to unity, we fix η in the far-field to be unity. This choice of scaling gives rise to the far-field condition

$$\eta \to 1, \qquad \text{as} \quad x \to \pm\infty. \tag{5.20}$$

It is left to solve the governing equation (5.13) for ϕ_1 and ϕ_2 in their respective flow domains, subject to boundary conditions, (5.14), (5.15), (5.17) and (5.19). We consider two values of ρ, that is $\rho = 0$ (one-layer model) and $\rho = 1$ (two-layer model). For the one-layer model, we ignore the outer boundary $r = D$. This is equivalent to taking $D \to \infty$. This removes the requirement to solve for ϕ_2, since the equations concerning just ϕ_1 form a closed system (no ϕ_2 terms are present in equation (5.17) when $\rho = 0$).

In the following section, we derive the linear dispersion relation for the system.

5.3 Linear theory

Consider a small perturbation to the undisturbed jet of the form

$$\phi_1 = \epsilon \sum_{m=1}^{\infty} F_m(r) e^{imk(x-ct)}, \qquad \phi_2 = \epsilon \sum_{m=1}^{\infty} G_m(r) e^{imk(x-ct)}. \tag{5.21}$$

where $|\epsilon| << 1$, and F_m and G_m are unknown functions of r. Note that if $c^2 > 0$, the solution is stable, while if $c^2 < 0$, the amplitude grows exponentially in time and the solution is unstable. Ignoring terms of $O(\epsilon^2)$, and solving the linearised system, one finds the equation for the free surface,

$$\eta = 1 + C_1\epsilon \left(I_1(k) - \frac{I_1(kd)}{K_1(kd)} K_1(k) \right) e^{ik(x-ct)} + \text{c.c.} \tag{5.22}$$

Here, I_n and K_n are the modified Bessel functions of the first and second kind of order n, and C_1 is an arbitrary constant. Equation (5.22) is a linear perturbation of wavenumber k, travelling at speed c. Furthermore, we recover the linear dispersion relation

$$c^2 = \frac{1}{k\left(\frac{m_2^d}{m_1^d} - \rho \frac{m_2^D}{m_1^D}\right)} \left(k^2 - 1 + B\right), \tag{5.23}$$

where

$$m_1^d = I_1(k)K_1(kd) - K_1(k)I_1(kd), \qquad m_2^d = I_0(k)K_1(kd) + I_1(kd)K_0(k). \tag{5.24}$$

Replacing all instances of d with D in the above equations gives m_1^D and m_2^D. If it is the case that $c(k) = c(nk)$ for some positive integer $n \geq 2$, then the leading order solution is given by

$$\begin{aligned}\eta = 1 &+ \epsilon C_1 \left(I_1(k) - \frac{I_1(kd)}{K_1(kd)} K_1(k) \right) e^{ik(x-ct)} \\ &+ \epsilon C_n \left(I_1(nk) - \frac{I_1(nkd)}{K_1(nkd)} K_1(nk) \right) e^{ink(x-ct)}.\end{aligned} \tag{5.25}$$

This phenomenon is called Wilton ripples, and is only possible when a minimum occurs in the dispersion relation (corresponding to $B > B_2$). Higher mode resonance was originally derived for gravity-capillary waves by Wilton [93]. One would expect to find at higher order a solvability condition for C_n. However, the algebra quickly becomes complicated, and instead these solutions are recovered via fully nonlinear computations, as seen in section 5.6.

Consider the denominator in equation (5.23). Modified Bessel functions of the first kind $I_n(z)$ of all orders are monotonically increasing and positive for $z \geq 0$ (see Abramowitz and Stegun [1]). Meanwhile, modified Bessel functions of the second kind $K_n(z)$ of all orders are monotonically decreasing, but remain positive, for $z \geq 0$. These properties ensure that $m_2^d > 0$ and $m_2^D > 0$. Furthermore, we find the relation

$$m_1^p = I_1(k)K_1(kp) - K_1(k)I_1(kp) \begin{cases} > 0 & \text{for } \ 0 < p < 1, \\ < 0 & \text{for } \ p > 1. \end{cases} \tag{5.26}$$

Hence, since $d < 1 < D$, we have that $m_2^d/m_1^d > 0$, while $m_2^D/m_1^D < 0$. Therefore, given $\rho \geq 0$, the denominator in equation (5.23) is always positive, meaning that the stability of the solution depends on k and B. We find that solutions with wavenumber k are stable if

$$k^2 > 1 - B. \tag{5.27}$$

This is true for all k if $B > 1$. Note that we recover the stability condition found by Rayleigh [73] by taking $B = 0$ (that all solutions with $k < 1$ are unstable).

The right hand side of equation (5.23) tends to infinity as $k \to \infty$. Hence, whether the dispersion curve has a minimum or not can be determined by considering the gradient of c^2 for small k. A negative gradient for small k corresponds to the existence of a minimum. Denoting the dispersion relation when $\rho = 0$ as c_ρ, we find that

$$c_\rho^2 = \frac{1}{k}\left(\frac{m_1^d}{m_2^d}\right)\left(k^2 - 1 + B\right). \tag{5.28}$$

Taking a small k expansion of the above equation, and differentiating with respect to k, one gets

$$2c_\rho \frac{dc_\rho}{dk} \approx \frac{1}{8}\left[\left(-1 + 4d^2 - 3d^2 + 4d^4 \log d\right)(B-1) + 8\left(1 - d^2\right)\right] k + O(k^3). \tag{5.29}$$

Hence, there exists a minimum in $c_\rho(k)$ given that the coefficient of k in the above equation is negative. This is the case if $B > B_2$, where B_2 has the following dependence on d:

$$B_2(d) = 1 + \frac{8\,(1-d^2)}{1 - 4d^2 + 3d^4 - 4d^4 \log d}. \tag{5.30}$$

This expression is in agreement with equation (3.5) in the paper of BP. We see in section 5.6 that the characteristics of the solution space changes upon the existence of a minimum.

When $\rho = 1$, we now expect B_2 to have dependence on both d and D. In the case when $D \to \infty$, BP demonstrated that $B_2 = 1$. For a finite value of D, one can follow the same argument given above for c_ρ to find that

$$B_2(d, D) = 1 - \frac{E}{F}, \tag{5.31}$$

where

$$E = \frac{\frac{1}{2}(1-d^2)(D^2-1)}{D^2 - d^2}, \tag{5.32}$$

$$F = \frac{1}{8\left(D^2 - d^2\right)^2}[(D^2-1)(1-d^2)(D-d)(D+d) + 2d^4\left(D^2-1\right)^2 \log d - 2D^4\left(d^2-1\right)^2 \log D]. \tag{5.33}$$

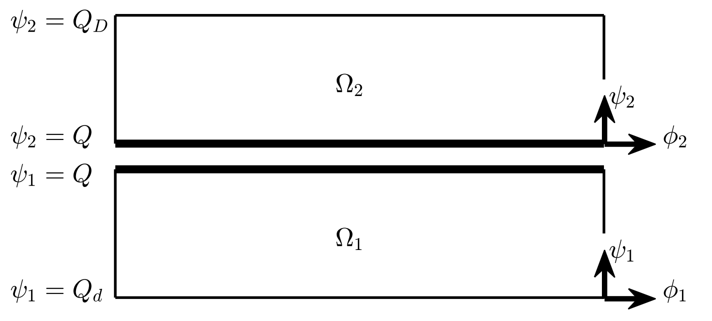

Figure 5.3: The two flow domains in potential space. The interface between the two fluids is in bold, and corresponds to the same streamline in physical space.

This agrees with the observation of BP, since $E/F \sim (\log D)^{-1}$ as $D \to \infty$. We will find it useful to denote the value of c at $k = 0$ as c_0, and the minimum value of c occurring at $k = k_m$ to be denoted c_m. When $B < B_2$, $c_0 = c_m$. In the following section, we describe the numerical method used to solve the fully nonlinear problem.

5.4 Numerical scheme

We consider a wave of wavelength λ travelling with unchanging form at a constant speed c. We remove time dependence by taking a frame of reference travelling with the wave. We will use a finite difference scheme, similar to the one proposed in chapter 4. We will first describe the method used to find solutions to the two-layer model. This involves adapting the finite difference scheme to allow for two computational domains, as described below. Following this, we state the simplifications made to the method to solve the one-layer problem.

As before, the idea is to solve the problem by finding the physical variable r in the two potential spaces (ϕ_1, ψ_1) and (ϕ_2, ψ_2), where ψ_1 and ψ_2 are the Stokes streamfunctions, defined by

$$u_i = \frac{1}{r}\frac{\partial \psi_i}{\partial r}, \qquad v_i = -\frac{1}{r}\frac{\partial \psi_i}{\partial x}, \qquad i = 1, 2. \tag{5.34}$$

Lines given by $\psi_i =$ constant are everywhere parallel to the velocity vector $\boldsymbol{u_i}$, and are orthogonal to lines of constant ϕ_i. Without loss of generality, we choose to define $\psi_1 = d^2c/2 = Q_d$ on $r = d$, $\psi_1 = \psi_2 = Q$ on the interface, and $\psi_2 = Q_D$ on $r = D$. We note that, in the case of a flat free surface (uniform stream solution), $Q = c/2$ and $Q_D = cD^2/2$. Integrating (5.34) with $u_i = c$ and $v_i = 0$, the uniform stream solution is found to be

$$r = \begin{cases} \sqrt{\frac{2\psi_1}{c}}, & \text{if } Q_d \leq \psi_1 \leq Q, \\ \sqrt{\frac{2\psi_2}{c}}, & \text{if } Q < \psi_2 \leq Q_D. \end{cases} \tag{5.35}$$

This encourages the coordinate transformations $\psi_1 = t^2$ and $\psi_2 = s^2$ to better distribute streamlines between the interface and the boundaries. This choice of transformation means that taking equally spaced points in the discretisation of t and s results in equally spaced streamlines in the computation of the uniform stream solution. Seeking a periodic wave of wavelength λ, symmetric about $\phi_1 = \phi_2 = 0$, the ferrofluid and surrounding fluid flow domains are mapped onto the rectangular domains Ω_1 and Ω_2 respectively, where

$$\Omega_1 = \left\{\phi_1 \in [-c\lambda/2, 0], t \in \left[Q_d^{1/2}, Q^{1/2}\right]\right\}, \tag{5.36}$$

$$\Omega_2 = \left\{\phi_2 \in [-c\lambda/2, 0], s \in \left[Q^{1/2}, Q_D^{1/2}\right]\right\}. \tag{5.37}$$

Here, we only consider the flow domains over half a wavelength, making use of the assumed symmetry. The flow domain in the potential space is shown in figure 5.3. Seeking r as a function of the independent variables (ϕ_1, ψ_1) in Ω_1 and (ϕ_2, ψ_2) in Ω_2, we find that equation (5.13) under the mapping becomes

$$r^3 \frac{\partial^2 r}{\partial \psi_i^2} + r \frac{\partial^2 r}{\partial {\phi_i}^2} + r^2 \left(\frac{\partial r}{\partial \psi_i}\right)^2 - \left(\frac{\partial r}{\partial \phi_i}\right)^2 = 0. \tag{5.38}$$

Furthermore, one can express $q_i = |\nabla\phi_i|$ and the mean curvature κ evaluated on the interface as functions of ϕ_i, using the identities

$$q_i(\phi_i) = \left(u_i^2 + v_i^2\right)^{1/2} = \left(\left(\frac{\partial r}{\partial \phi_i}\right)^2 + r^2\left(\frac{\partial r}{\partial \psi_i}\right)^2\right)^{1/2}, \tag{5.39}$$

$$\kappa_i(\phi_i) = -q_i^3\left(r\frac{\partial r}{\partial \psi_i}\frac{\partial^2 r}{\partial \phi_i^2} - \left(\frac{\partial r}{\partial \phi_i}\right)^2\frac{\partial r}{\partial \psi_i} - r\frac{\partial r}{\partial \phi_i}\frac{\partial^2 r}{\partial \phi_i \psi_i}\right) + \frac{\partial r}{\partial \psi_i}q_i. \tag{5.40}$$

Note that κ_1 here denotes the mean curvature as a function of ϕ_1, and likewise for κ_2. These functions correspond to the same curve in physical space (the interface), and hence have the same value at given points along the interface, but are different functions due to the discontinuity in tangential velocities across the interface. We discretise Ω_1 and Ω_2 into equidistant points with M points in ϕ_1 and ϕ_2, N points in t, and P points in s as follows

$$\phi_{1_i} = \phi_{2_i} = -\frac{c\lambda}{2(M-1)}(M-i), \qquad i = 1, \cdots, M, \tag{5.41}$$

$$t_j = Q_d^{1/2} + \left(Q^{1/2} - Q_d^{1/2}\right)\frac{j-1}{N-1}, \qquad j = 1, \cdots, N, \tag{5.42}$$

$$s_j = Q^{1/2} + \left(Q_D^{1/2} - Q^{1/2}\right)\frac{j-1}{P-1}, \qquad j = 1, \cdots, P. \tag{5.43}$$

We satisfy the governing equation (5.38) at the interior nodes of Ω_1 and Ω_2, finding the values of derivatives with finite difference approximations. We use second order central differences, making use of the symmetry by imposing $\partial r/\partial \phi_i = 0$ at $\phi_i = 0$ and $\phi_i = -c\lambda/2$ (for $i = 1, 2$). On the interface, we use second order backwards differences to compute derivatives with respect to t, and forward differences for derivatives with respect to s. Derivatives with respect to ψ_1 are given in terms of derivates with respect to t via the identities

$$\frac{\partial}{\partial \psi_1} = \frac{1}{2t}\frac{\partial}{\partial t}, \tag{5.44}$$

$$\frac{\partial^2}{\partial \psi_1^2} = \frac{1}{4t^2}\left(\frac{\partial^2}{\partial t^2} - \frac{1}{t}\frac{\partial}{\partial t}\right). \tag{5.45}$$

The same is done for ψ_2 and s. Equations (5.14) and (5.15) can be written as

$$r(\phi_1, Q_d) = d, \qquad r(\phi_2, Q_D) = D, \tag{5.46a,b}$$

respectively. Finally, we satisfy the dynamic boundary condition (5.17) on the interface in both Ω_1 and Ω_2. For example, consider (5.17) satisfied in Ω_1. Making use of (5.39), this gives

$$\frac{1}{2}\left(\left[\left(\frac{\partial r}{\partial \phi_1}\right)^2 + r^2\left(\frac{\partial r}{\partial \psi_1}\right)^2\right] - \rho\left[\left(\frac{\partial r}{\partial \phi_2}\right)^2 + r^2\left(\frac{\partial r}{\partial \psi_2}\right)^2\right]\right) + \kappa_1 - \frac{B}{2r^2} = C, \tag{5.47}$$

where κ_1 is computed using (5.40). Note that the time dependent term is removed due to the moving frame of reference. We see that we require $\partial r/\partial \phi_2$ and $\partial r/\partial \psi_2$ as functions of ϕ_1 on the interface to solve this equation in Ω_1. Similarly, we require $\partial r/\partial \phi_1$ and $\partial r/\partial \psi_1$ as functions of ϕ_2 to solve it in Ω_2. This is done by integrating the identities

$$\frac{\partial x}{\partial \phi_i} = r\frac{\partial r}{\partial \psi_i}, \qquad i = 1, 2, \tag{5.48}$$

on the interface to find x as a function of ϕ_1 in Ω_1, and x as a function of ϕ_2 in Ω_2. We then interpolate in x to find ϕ_2 as a function of ϕ_1, since the interface is the same in either domain. An unfortunate consequence of the interpolation procedure is that it requires the interface η to be a single valued function of x, meaning the method will not work for overhanging waves.

Fixing a value of B, the system above provides $M(P+N)$ equations for $M(P+N)+4$ unknowns (r at each meshpoint, C, c, Q and Q_D). We obtain three additional equations by fixing the amplitude A of the wave,

$$A = r(0, Q) - r\left(-c\lambda/2, Q\right), \tag{5.49}$$

and the wavelength λ,

$$\lambda = \left[\int_{-c\lambda}^{0} r\frac{\partial r}{\partial \psi_1}\,\mathrm{d}\phi_1\right]_{\psi_1=Q}, \qquad \lambda = \left[\int_{-c\lambda}^{0} r\frac{\partial r}{\partial \psi_2}\,\mathrm{d}\phi_2\right]_{\psi_2=Q}. \tag{5.50a,b}$$

Finally, we fix the mean displacement of the interface ($R = 1$) by writing

$$\left[\int_{-\lambda c/2}^{0} (r-1)r\frac{\partial r}{\partial \psi_1}\,\mathrm{d}\phi_1\right]_{\psi_1=Q} = 0. \tag{5.51}$$

In some instances, it is convenient to fix instead the speed c and allow the amplitude A to be an unknown. The discrete system of $M(P+N)+4$ equations for $M(P+N)+4$ unknowns can be solved numerically via Newton's method. We terminate the iterations in Newton's method once the L^{∞}-norm of the residuals is of order 10^{-11}.

When considering pure solitary waves, the far-field condition (5.20) is equivalent to demanding r tends to the uniform stream solution (5.35) as $\phi_i \to \pm\infty$. Furthermore, the far-field condition fixes the Bernoulli constant $C = (1-\rho)c^2/2+1-B/2$ (see equation (5.17)) and the fluxes $Q = c/2$ and $Q_D = cD^2/2$. In such circumstances, we replace the governing equation (5.38) with equation (5.35) at the meshpoints $\phi_{1_1} = \phi_{2_1} = -c\lambda/2$. Again, we obtain $M(N+P)$ equations from the field equation and boundary conditions. We obtain an additional equation by fixing the amplitude of the wave, which for solitary waves we choose to be the value of r on the interface at the point of symmetry. This results in $M(P+N)+1$ equations for the $M(P+N)+1$ unknowns (r at each meshpoint, and c). We must take λ large enough such that the solution becomes identical within graphical accuracy to further increase in λ. This is common practice when computing solitary waves (for example, see Byatt-Smith and Longuet-Higgins [19]), since computationally we cannot solve for infinitely large domains. As with the Taylor bubbles in chapter 4, it is found the errors associated with domain truncation are negligible given a suitably large value of λ. The value required depends on the amplitude of the solution. We found it difficult to compute solitary waves of very small amplitude (around $A < 0.01$), since the waves become broader as the amplitude decreases further.

The numerical scheme described above is used to find solutions for the two-layer model. When finding solutions for the one-layer problem, we do not need to solve for values of r in the domain Ω_2, or the value Q_D. For example, for one-layer periodic waves, there are $MN + 3$ unknowns (r at each meshpoint in Ω_1, C, c, and Q). We solve the field equation (5.38) at interior nodes of Ω_1. Furthermore, we satisfy (5.47) with $\rho = 0$ on $\psi_1 = Q$, as well as equations (5.46a), (5.49), (5.50a) and (5.51). This results in a closed discrete system of $MN + 3$ equations for $MN + 3$ unknowns. Furthermore, since we do not require values from Ω_2 to solve equation (5.47) in Ω_1, we no longer need to interpolate values in x, as is done in the two-layer problem. This allows us to compute overhanging solutions for the one-layer model.

Typical mesh sizes for periodic waves are $M = 200$, and N and P are chosen such that differences in t are approximately equal to differences in s. For example, with $d = 0.5$ and $D = 2$, we took $N = 30$ and $P = 60$. For solitary waves, larger values of M are considered. Meshes of this size are possible due to the sparsity of the Jacobian matrix. Furthermore, for more extreme profiles, it can be useful to perform the coordinate transforms

$$\phi = -c\lambda(1-\alpha^2)/2, \qquad \text{or} \qquad \phi = -c\lambda\alpha^2/2, \tag{5.52}$$

on either ϕ_1 or ϕ_2 (or both), and then take equally spaced points in $\alpha \in [0, 1]$. The first transformation condenses points close to $\phi = -c\lambda/2$, while the second condenses points near $\phi = 0$. The transformation is chosen such that the distribution of points is more uniform. There are less points in areas of small velocities if equally spaced points in ϕ are used.

In the following section, we discuss the possible static configurations of the problem.

5.5 Static Profiles

It is helpful to discuss static configurations of this problem ($c = 0$), since many of the dynamic solution branches terminate on static profiles. Setting all time derivatives and velocities to zero in equation (5.17), it is left to find η that satisfies

$$\kappa - \frac{B}{2\eta^2} = C, \tag{5.53}$$

where κ is the mean curvature. BP solved equation (5.53) by parameterising the problem in terms of arclength s, and expressing it as a two-dimensional conservative system for the unknowns η and α, where $\alpha = \tan \eta_x$. This is given by

$$\frac{d}{ds}\begin{pmatrix}\eta \\ \alpha\end{pmatrix} = \begin{pmatrix}\sin\alpha \\ \cos\alpha/\eta - B/(2\eta^2) - C\end{pmatrix}. \tag{5.54}$$

They found that the energy, E, given by

$$E = \eta\cos\alpha - \frac{C}{2}\eta^2 - \frac{B}{2}\log\eta, \tag{5.55}$$

is a conserved quantity. Curves of constant E correspond to trajectories in the (α, η) plane. Full details can be found in section 4 of BP. There are four possible fixed points of the system, given by

$$(2n\pi, \beta_+), \quad (2n\pi, \beta_-), \quad ((2n+1)\pi, \gamma_+), \quad ((2n+1)\pi, \gamma_-). \tag{5.56}$$

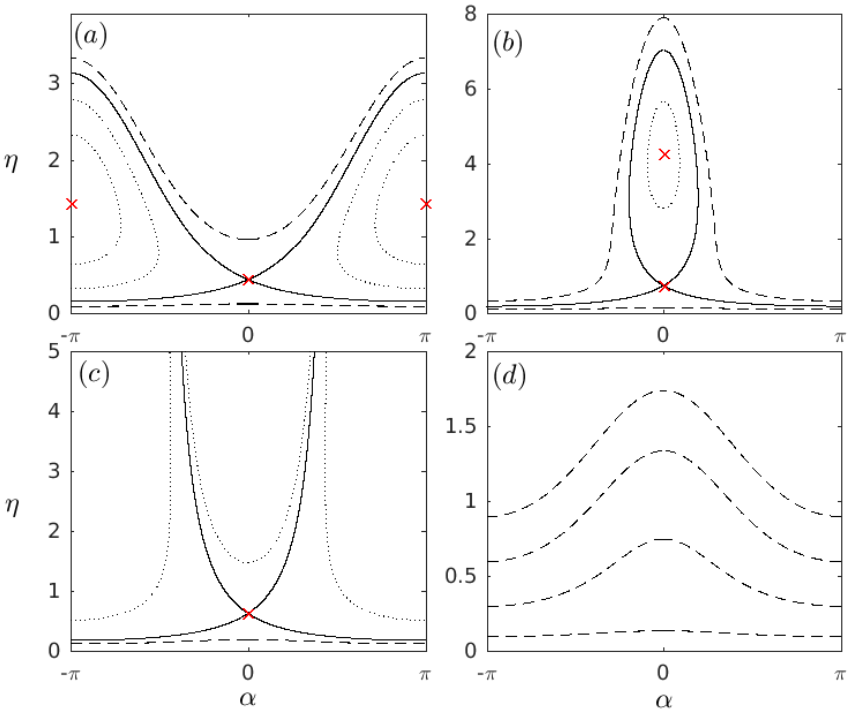

Figure 5.4: Curves of constant E in the (α, η) plane. All figures are for $B = 1.25$. The values of C are (a) $C = -1$, (b) $C = 0.2$, (c) $C = 0$ and (d) $C = 2$. The critical points are labeled with crosses.

where

$$\beta_{\pm} = \frac{1 \pm \sqrt{1 - 2CB}}{2C}, \qquad \gamma_{\pm} = \frac{-1 \pm \sqrt{1 - 2CB}}{2C}. \tag{5.57}$$

Since we only consider solutions with $\eta \geq 0$, assuming $B > 0$, the existence of these fixed points can be broken down into four cases.

In the first case, when $C < 0$, we find that the fixed point $(2n\pi, \beta_-)$ is a saddle point, and the fixed point $((2n+1)\pi, \gamma_-)$ is a centre. The other two fixed points are unphysical, and are ignored. Figure 5.4a shows trajectories in the (α, η) space. The two heteroclinic orbits (solid lines) connecting the saddle points at $(2n\pi, \beta_-)$ and $(2(n+1)\pi, \beta_-)$ correspond to two solitary waves (one elevation, one depression) with radial displacement β_- in the far-field. These solutions self-intersect, and are hence unphysical. The circular orbits (dotted lines) contained inside the heteroclinic orbits correspond to smooth (here meaning not self-intersecting) periodic profiles, while the 2π periodic curves (dashed lines) correspond to self-intersecting periodic

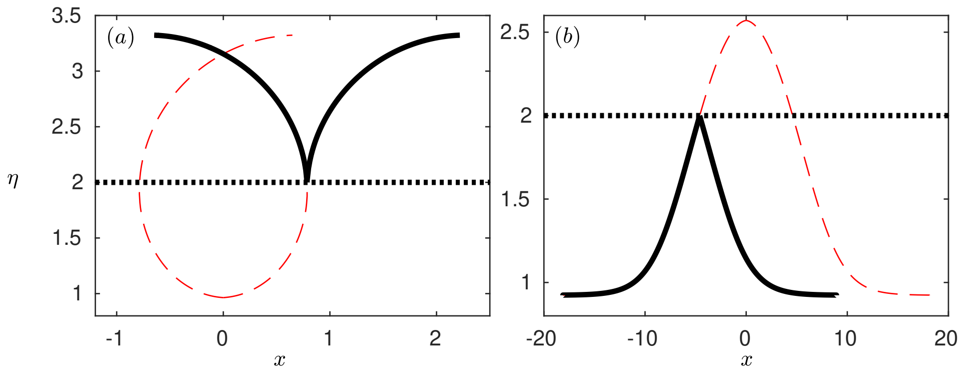

Figure 5.5: The dashed curves are profiles of static configurations. In figure 5(a), this static solution corresponds to a 2π periodic curve in the (α, η) space, while in figure 5(b), it corresponds to a homoclinic orbit. The dotted curves we take as boundaries below (figure (a)) or above (figure (b)) the profile. The black curves show the modified solution, taken by reflecting the relevant part of the dashed profile.

profiles.

Next, when $0 < C < \frac{1}{2B}$, we find that the fixed point $(2n\pi, \beta_-)$ is again a saddle point, and the fixed point $(2n\pi, \beta_+)$ is a centre. Figure 5.4b is an example of the (α, η) space. The homoclinic orbit connecting the saddle point to itself corresponds to a smooth elevation solitary wave profile. The heteroclinic orbits connecting the saddle points are again self-intersecting solitary waves. Circular orbits correspond to smooth periodic profiles, and 2π periodic curves are self-intersecting periodic solutions.

When $C = 0$, we find that the only fixed point is the saddle point $(2n\pi, \beta_-)$, where $\beta_- = B/2$. Figure 5.4c is a typical phase space. There exist heteroclinic orbits connecting the saddle points with $\eta < \beta_-$, as is seen in both the above cases. However, the curves exiting the saddle point with $\eta > \beta_-$ form neither a homoclinic orbit back to the same critical point, nor does it form a heteroclinic orbit to the saddle points at $\alpha = 2n\pi \pm 2\pi$. Instead, they tend to $\eta \to \infty$ at $\alpha = 2n\pi \pm \pi/2$. The dotted lines also approach $\alpha = \pi/2$ as $\eta \to \infty$. The dashed curves beneath the saddle point are 2π periodic curves.

Finally, when $C > 1/(2B)$, there are no physical fixed points, and all trajectories are 2π periodic curves in the (α, η) space, corresponding to self intersecting periodic profiles. These are shown by the dashed curves in figure 5.4d.

When seeking solitary waves which satisfy equation (5.20), equation (5.53) (when satisfied in the far-field) implies that $C = 1 - B/2$. When this is the case, the saddle point $(2n\pi, \beta_-)$ satisfies $\beta_- = 1$, which corresponds to the far-field of the solitary wave. When $B > 2$, the phase space is qualitatively similar to that of figure 5.4a (i.e. the $C < 0$ phase space). The elevation and depression solitary waves are both self intersecting. When $1 < B < 2$, the phase space is qualitatively similar to that of figure 5.4b. Within this parameter regime, there exists elevation solitary waves which do not self intersect, which as mentioned above is given by the homoclinic orbit. An interesting question is what happens in the limit as $B \to 2$. The value of β_+ is

$$\beta_+ = \frac{B}{2 - B}. \tag{5.58}$$

Hence, as $B \to 2$, the value of β_+ becomes infinitely large. It follows that the amplitude of the homoclinic orbit surrounding the center, which we shall denote $\eta_{\max}$, also becomes infinitely large in the limit $B \to 2$. Meanwhile, as $B \to 1$, we have that $\beta_+ \to 1$. Hence, there exists a family of smooth static elevation solitary waves for $B \in (1, 2)$, whose amplitude $\eta_{\max} \in (1, \infty)$ is a monotonically increasing function of B. This will be useful to note later when discussing in what parameter regimes we expect to see static solitary waves.

All of the solutions described above are one-dimensional profiles that satisfy (5.53) and $\eta \geq 0$ with $c = 0$. We integrate for values of x along the curve of constant E via the integral

$$x = \int\limits_{E=\text{const}} \cot\alpha \, \mathrm{d}\eta, \tag{5.59}$$

to obtain the profile in the (x, η) space. This integral is evaluated numerically using the trapezoidal rule.

The solutions do not take into consideration any boundaries at $r = d$ and $r = D$. As mentioned by BP, it is of interest to note that we can interpret the profiles even if they intersect a boundary: the solutions can be seen as profiles which touch a boundary. We then consider the profile up to the point of contact, where the solution is reflected. This is demonstrated in figure 5.5, where two examples of a static profile (dashed curves) crossing a boundary (dotted curve) from above and below (figure (a) and (b) respectively) is interpreted this way. We only consider the portion of the profile satisfying $d \leq \eta \leq D$. In figure (a), the dashed profile self-intersects, and is hence not physical without the inclusion of a boundary. The dashed profile of figure (b) is a static elevation solitary wave, and is a valid solution without the boundary. We note that these modified solutions disregard the complicated physical properties of contact angles (for example, see Batchelor [9] §1.9). Despite this, the solutions are still of importance to consider, since many dynamic solution branches approach such static limiting configurations, as shown in section 5.6.

In the next section, we discuss the results found using the numerical procedure introduced in section 5.4 for non-static solutions, and how they relate to the static solutions discussed above.

5.6 Results

A thorough numerical investigation was performed by BP on the one-layer model for solitary waves. In this section, we find new results for periodic and generalised solitary waves. We will repeat a discussion of the results of BP, since it will help to explain the solution space of the two-layer model, where there are many similarities. We differentiate between two distinct cases, when there does not exist a minimum in the dispersion curve ($B < B_2$) and when there does exist a minimum ($B > B_2$), describing the solution space in each instance. Below, we first consider $B < B_2$.

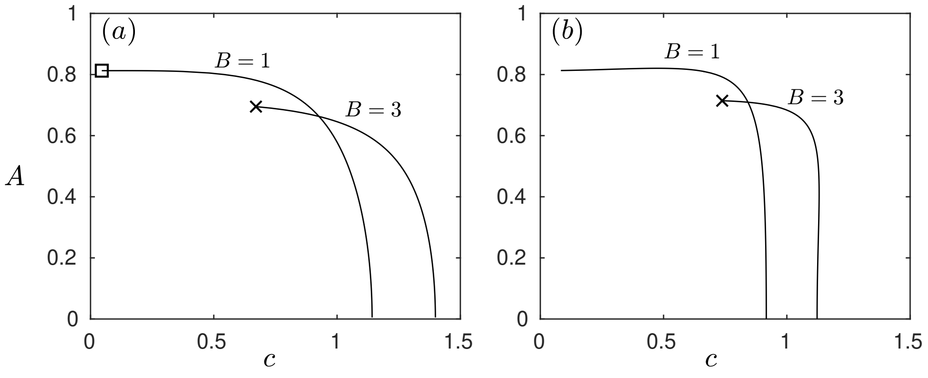

Figure 5.6: Periodic solution branches with $\lambda = \pi$ and $d = 1.5/3.8$. Figure (a) shows one-layer solution branches, while figure (b) is for two-layer solution branches with $D = 2$. In both cases, the $B = 1$ branch terminates on a static profile which touches the bottom boundary $r = d$. The $B = 3$ branch for $\rho = 0$ overturns and ultimately forms a trapped bubble. The limiting configuration of the $B = 3$ branch for $\rho = 1$ is unknown.

5.6.1 $B < B_2$

5.6.1.1 One-layer

We begin by considering the solution space for the one-layer model. Using a linear solution (5.22) as an initial guess in the Newton's iterations, we are able to use the numerical method described in section 5.4 to compute periodic solutions. Once on a solution branch, we can use the method of continuation to compute larger amplitude solutions. In figure 5.6a, we show some solution branches for periodic waves for the one-layer model. These branches have the value $d = 1.5/3.8$, which is the value of d used in the experiments of Bourdin et al. [15] for periodic waves. We computed branches for a variety of parameter values to determine the effect the parameters have on the solutions. Our findings are presented below.

The solution branches terminate in a variety of ways. It can be the case that, given B and d are sufficiently small, the solution branch terminates on a smooth static profile. These static solutions were computed for $B = 0$ by Vanden-Broeck et al. [90]. We cannot use the numerical scheme described in section 5.4 to compute the static profiles, since the method assumes the existence of a velocity field. However,

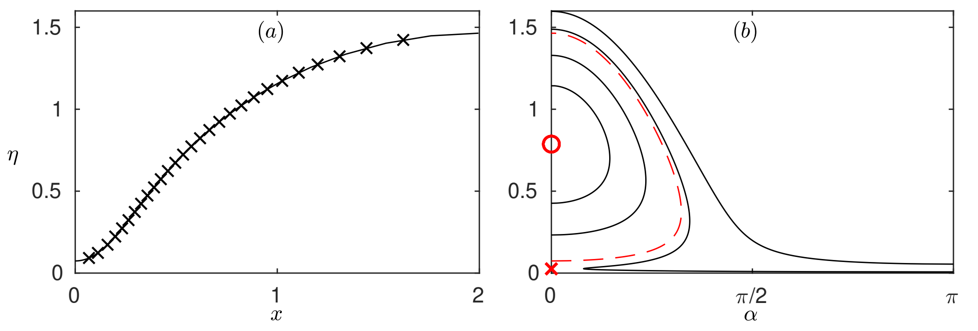

Figure 5.7: Figure (a) shows a comparison between a one-layer solution found for $c = 0.02$ (solid curve) and a smooth static profile (crosses). Only half a wavelength is shown. The solution has parameter values $d = 0$, $B = 0.05$ and $\lambda = 4$. Figure (b) shows the trajectories in the (α, η) space. The dashed curve is the solution given by the crosses in figure (a). In figure (b), the cross is a saddle point and the circle a centre.

one can continue along the solution branches up to small values of c. We can then extrapolate to find an approximate value of the Bernoulli constant C for $c = 0$. This allows us to find the set of static configurations in the (α, η) space associated with the given Bernoulli constant, as described in section 5.5. Comparisons can then be made with the small c profile and the static profile obtained by integrating along the curve of constant energy E, where E can be obtained by evaluating equation (5.55) at some meshpoint on the interface of the small c solution. Periodic smooth static profiles are orbits in the (α, η) space. Figure 5.7a is a comparison between a one-layer solution with parameter values $B = 0.05$, $\lambda = 4$, $d = 0$ and $c = 0.02$, and the static profile obtained by integrating along the corresponding trajectory in the (α, η) space (the (α, η) space is shown in figure 5.7b). The agreement between the two profiles obtained via different methods provides a check on our numerical method, and demonstrates that the solution branches can terminate on static profiles. These smooth static configurations only occur for small values of B. For example, with the parameter values of the solution shown in figure 5.7, but with $B = 0.1$, it is found that the solution branch instead terminates on a static profile which touches the bottom boundary. This is described below.

As mentioned in section 5.5, static profiles can be interpreted as solutions which

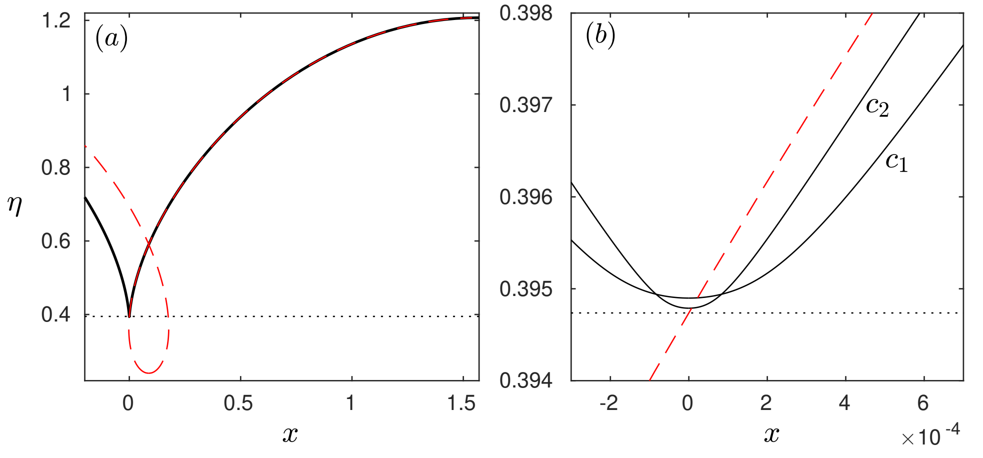

Figure 5.8: Figure (a) is a comparison between the solution corresponding to the square in figure 5.6a (given by the solid curve) and its corresponding $c = 0$ solution (dashed curve). Figure (b) shows a blow up of the behaviour close to the point of contact for solutions with phase speeds $c = c_1 = 0.08$ and $c = c_2 = 0.05$.

touch a boundary. It is found that this configuration is a limiting case for many solution branches. Consider one-layer periodic solutions for varying values of d. For a fixed B, if d is large enough, as we continue along a solution branch, the value of c decreases as the solution forms a profile which gets very close to the boundary $r = d$. A branch which terminates in such a manner is the $B = 1$ branch from figure 5.6a. The final solution computed along the branch (shown by the square in the figure) is a solution for $c = 0.05$. Figure 5.8a shows the profile of this solution. Computing a static profile with the same value of C and E results in a self-intersecting profile, shown by the dashed curve in the figure. The static profile agrees well with the $c = 0.05$ solutions up to where the static solution intersects the boundary. Figure 5.8b shows a blow up of this region. The two solid curves are solutions with the phase speeds $c = c_1 = 0.08$ and $c = c_2 = 0.05$. The image shows that as the speed is decreased further, the agreement between the curves and the static profile improves, and the thickness of the layer of fluid at the point of intersection continues to decrease. This provides numerical evidence that as $c \to 0$, the dynamic profile approaches a static solution which touches the bottom boundary.

The final possible limiting configuration of one-layer periodic solution branches

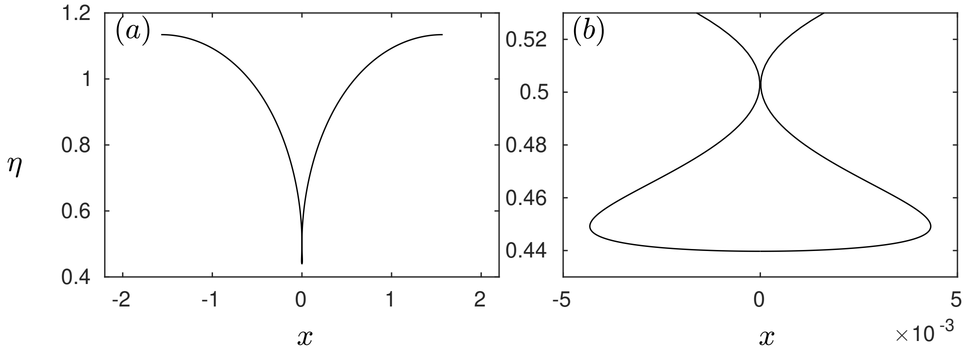

Figure 5.9: Periodic solution corresponding to the cross in figure 5.6 a. Figure (*a*) shows one wavelength of the solution. Figure (*b*) is a blow up of the trapped bubble.

are profiles with a trapped bubble. Such branches occur for larger values of B than the branches which terminate in static solutions. The $B = 3$ branch of figure 5.6a is one such example, and the profile of the limiting configuration solution (corresponding to the cross in figure 5.6a) is shown in figure 5.9. This limiting configuration has been found to occur for two-dimensional capillary and gravity-capillary waves, as found by Crapper [23], Kinnersley [53] and Hunter and Vanden-Broeck [50]. Such solutions were also found for axisymmetric capillary waves ($B = 0$) by Vanden-Broeck et al. [90]. Continuing along the branch past the trapped bubble solutions, we find solutions with self intersecting interfaces. Such solutions are not physically valid. It may be possible to extend the solution branch by allowing the pressure inside the bubble to vary, as was done by Vanden-Broeck and Keller [89] for two-dimensional capillary waves. However, difficulties are experienced, since this introduces a discontinuity in equation (5.47), and hence in the derivatives of r, which in turn would require a more sophisticated treatment in a finite difference scheme. These intricate overturning solutions require a larger number of meshpoints to retain accuracy. A discussion of the numerical errors can be found in section 5.6.3.

In section 5.3, we saw that when $B > 1$, all wavelengths are stabilized. This allows for the existence of pure solitary waves. Starting from small amplitude, as we increase λ, the waves form longer troughs and shorter crests. In the limit $\lambda \to \infty$, the solutions approach a solitary wave with a flat far-field. These solitary wave branches bifurcate from the uniform stream at c_0. Assuming $d = 0$, Rannacher and Engel [72] obtained a KdV equation which approximates such solutions for small amplitude. Fully non-linear computations of the solutions with arbitrary d were done by BP. They found that, in agreement with the KdV equation, there exists critical values $B_1(d)$ and $B_2(d)$ such that when $B < B_1$, the solitary waves are of elevation, while if $B_1 < B < B_2$, the solutions are depression waves. These waves get broader as the amplitude goes to zero, making it computationally impossible to compute the branches all the way to the bifurcation point.

As well as the solitary waves bifurcating from the uniform stream, BP found solitary waves solutions which bifurcate from finite amplitude. For $1 < B < B_1$, these branches are waves of depression. The amplitude from which these solution branches bifurcate decreases as B increases up to B_1. Meanwhile, for $B_1 < B < 2$, the finite amplitude bifurcating branches are elevation solitary waves. The amplitude at which these branches bifurcates decreases as B approaches B_1 from above. It would appear that the bifurcating amplitude of these two branches approaches zero as B tends to B_1. This is further supported by the analysis of Groves and Nilsson [45], who for $d = 0$ derived a cubic KdV equation (see equations (1.4)-(1.5) in their paper) for the model when B is close to B_1. The equation predicts that both elevation and depression waves exist in this region, both of which bifurcate from zero amplitude. The numerical results of BP suggest that this is also true for non-zero values of d, although difficulties in computing solution branches up to the point of bifurcation due to wave broadening deny conclusive numerical evidence.

The existence of the finite amplitude bifurcating pure solitary waves is in stark contrast with the gravity-capillary problem, where such solutions have not been observed. Continuing the branches beyond the bifurcation point into large amplitudes, BP found that depression waves terminate in either static profiles which touch the

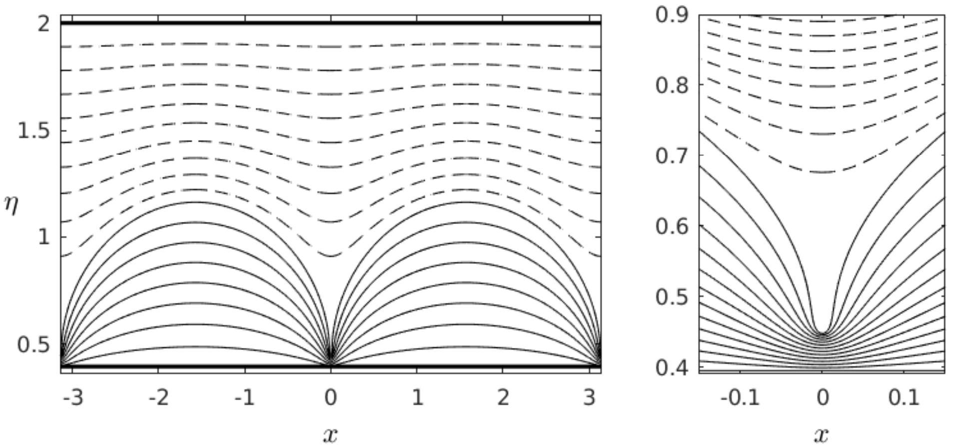

Figure 5.10: Periodic solution corresponding to the cross in figure 5.6b. Two wavelengths are shown. Streamlines in the ferrofluid are the black curves, while streamlines in the second fluid are the dashed curves. Not all streamlines have been plotted. This is the largest amplitude solution computed on this solution branch. The branch could not be computed further due to difficulties with overturning.

bottom boundary, or overturning waves with a trapped bubble, while elevation solitary wave branches terminate in smooth static configurations. They also found that the amplitude of the $B = 2$ elevation branch increases indefinitely. These results make sense in light of the discussion in section 5.5. Reverse engineering the elevation branches, by starting from a static solution and increasing c, we expect solutions in the range $1 < B < 2$ (the values for which static elevation solitary waves exist). The $B = 2$ branch is a limiting case, where the end point of the branch is an elevation wave of infinite amplitude. Meanwhile, no smooth static depression solutions were found, and hence static depression waves must touch the bottom boundary.

5.6.1.2 Two-layer

Next, we shall discuss the solution space for the two-layer model when the dispersion relation is monotonic increasing. Again, starting from linear solutions, we can use the method of continuation to compute periodic solution branches. Some periodic solution branches are shown in figure 5.6b. These branches have the same parameter values as the one-layer periodic branches of figure 5.6a, except for a density ratio of unity between the two fluids (since it is the two-layer model), and an

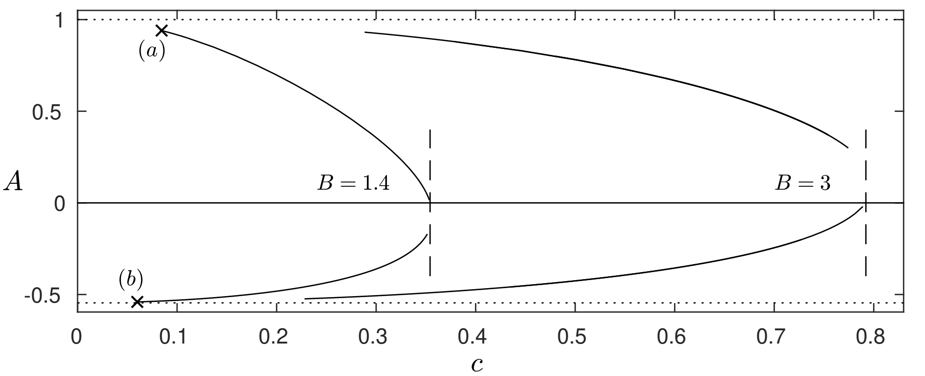

Figure 5.11: Two-layer pure solitary wave branches with $d = 1.5/3.3$ and $D = 2$ for $B = 1.4$ and $B = 3$. The dashed curves show the value of c_0 for the two choices of B, while the dotted curves correspond to the maximum possible value of the amplitude, where the profile touches a boundary. The points $(a) - (b)$ refer to the solutions shown in figure 5.12.

additional outer boundary at $r = D$, where $D = 2$. The $B = 1$ branch, as with the one-layer $B = 1$ branch, terminates on a static profile which touches the boundary $r = d$. Decreasing the value of D, one finds the solution branches can also terminate on static profiles which touch the upper boundary. For example, for the $B = 1$ branch discussed above, taking the same parameter values but changing D to $D = 1.3$ results in such a limiting configuration.

Next, consider the $B = 3$ branch. Due to the similarities between the one-layer and two-layer model for the $B = 1$ model, one may expect this solution branch to form overturning solutions, and eventually form a trapped bubble. Unfortunately, as mentioned earlier, the numerical method described in section 5.4 cannot compute overturning solutions for the two-layer model. This is due to the interpolation procedure for values on the interface being performed in the x variable, for which overturning solutions are not single-valued. One may be tempted to instead interpolate in the r variable, for which these solutions are single-valued. However, the code is extremely sensitive to this method and fails to converge. We have computed the $B = 3$ branch from figure 5.6b as far as computationally possible with the method. The profile of this solution is shown in figure 5.10. We believe the solution will overturn as one continues along the branch. However, a new numerical treatment

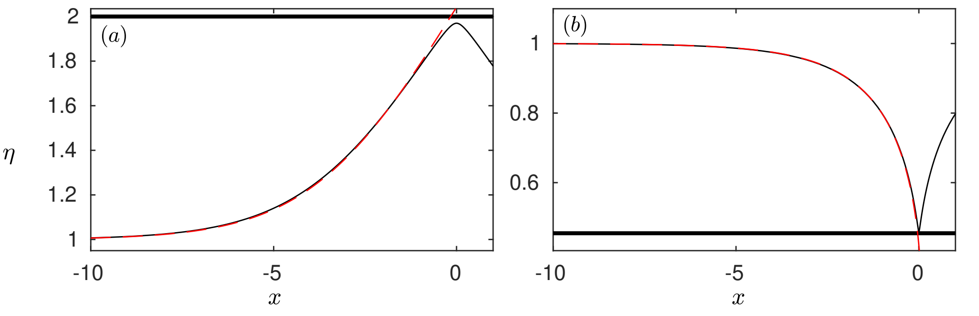

Figure 5.12: Profiles corresponding to the points (a) and (b) in figure 5.11. They approach static profiles which touch $r = D$ and $r = d$ respectively. The dashed curves are static profiles which the solutions approach as $c \to 0$.

of the problem will be required to investigate these solutions. Overturning two-dimensional gravity-capillary internal waves have been found in the recent numerical and analytical investigations of Akers et al. [3].

For $B > 1$, we again expect to see pure solitary waves. Some solution branches for $d = 1.5/3.3$ and $D = 2$ are shown in figure 5.11. It can be seen that for $B = 1.4$, the elevation branch bifurcates from zero amplitude, while the depression branch bifurcates from non-zero amplitude. The roles are reversed when $B = 3$, implying $B_1 \in (1.4, 3)$ for the given values of d and D. Due to the existence of the upper boundary $r = D$, the elevation branches can now terminate on static profiles which touch the boundary. This is shown in figure 5.12a, where an elevation solitary wave for $c = 0.08$ is shown to be in good agreement with a static profile that crosses $r = 2$. This new limiting configuration means that, unlike for the one-layer model, there now exists pure elevation solitary waves (bifurcating from finite amplitude) for values of $B > 2$. One does not have to consider the case when there is no upper boundary for two-layer pure solitary wave solutions, since BP showed that when $D \to \infty$, there exists a minimum in the dispersion curve for $B > 1$, removing the possibility of pure solitary waves (it can be seen from equations (5.31)-(5.33) that $B_2 \to 1$ as $D \to \infty$).

A description of the solution space when there exists a minimum is presented in the following section.

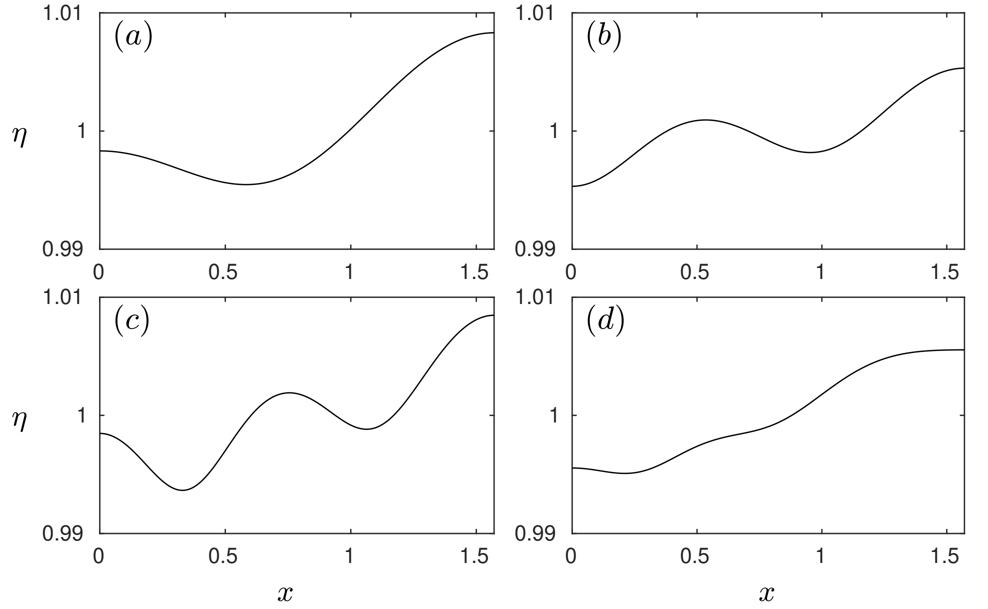

Figure 5.13: One-layer solutions exhibiting higher mode resonance for $\lambda = \pi$ and $d = 0$. Only half a wavelength is shown. The values of B are $B = 16.4$, $B = 21.7$, $B = 27.2$ and $B = 32.8$ while the values of n in equation (5.25) are $n = 2, 3, 4, 5$ for figures (a), (b), (c), and (d) respectively.

5.6.2 $B > B_2$

As stated previously, if $B > B_2$, then a minimum occurs in the dispersion relation. We will discuss the results for the one-layer and two-layer model simultaneously, since the solution spaces in this regime are qualitatively similar. The only difference occurs for overhanging solutions, where our inability to compute overhanging solutions for the two-layer model means the limiting configurations of some two-layer solution branches remain unknown. This is discussed below.

When there is a minimum in the dispersion curve, we see periodic solutions exhibiting higher mode resonance, as described by equation (5.25). These solutions exist for integer values of $n > 1$ when $c(k) = c(nk)$, where c is given by (5.23). Fixing a value of k and n, we can find a value of B such that this equality is satisfied. Using these parameter values, we are able to compute solutions with Wilton ripples, as shown in figure 5.13 for $n = 2, 3, 4, 5$. These solutions are for the one-layer model. One can continue these branches of solutions into highly nonlinear regimes by further increase of the amplitude. They form interesting profiles, where the depression of

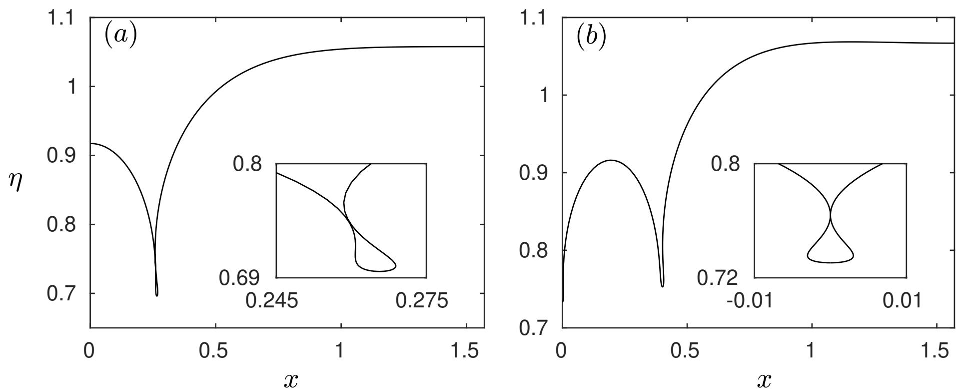

Figure 5.14: The limiting configuration of the solution branch obtained by continuing the solutions of figure 5.13a and 5.13b to larger amplitude. Only half a wavelength is shown. The inset shows the trapped bubble formed by each solution.

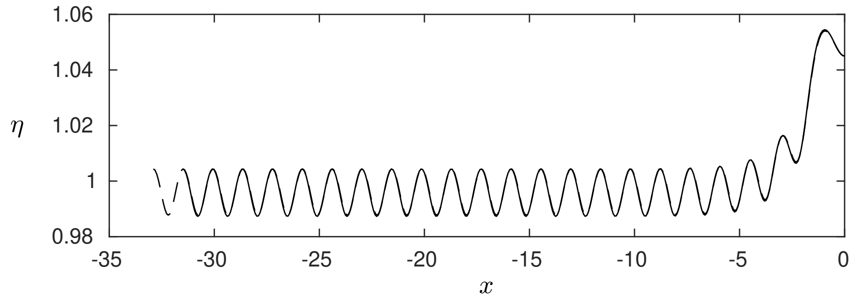

Figure 5.15: Two one-layer long wave solutions with parameter values $B = 13$, $d = 0$, $c = 12.5$ and $\eta(0) = 1.045$, and wavelengths $\lambda = 65.8$ (solid curve) and $\lambda = 71.1$ (dashed curve). It can be seen that the two profiles almost perfectly overlap, where the longer solution has an additional periodic wave in the tail.

each ripple begins to overturn (see figure 5.14). They terminate once one of the overhanging structures forms a trapped bubble. These results can be repeated for the two-layer problem, although as before we are unable to extend solution branches beyond the point of overturning.

Increasing the wavelength of periodic solutions when $c(k)$ has a minimum results in a larger central peak or trough, and a train of smaller amplitude waves in the far-field. Denote the wavelength of the far-field waves as $\widehat{\lambda}$. Increasing the wavelength of the solution by $\widehat{\lambda}$ results in two almost overlapping solutions, where the longer wave has one additional linear wave in the far-field. This is demonstrated in figure 5.15. One can easily add more waves to the far-field, limited only by computational storage. These solutions are finite wavelength approximations of generalised solitary waves. As one would expect, $\widehat{\lambda}$ is found to be the finite valued wavelength which gives

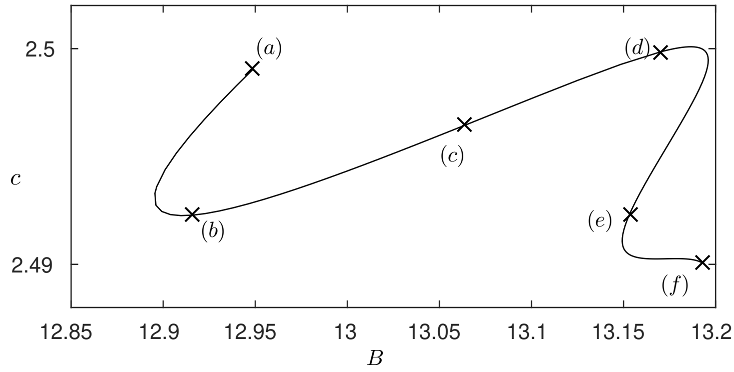

Figure 5.16: Generalised solitary wave branch for $\eta(0) = 1.045$ and $\lambda = 63$. Some profiles corresponding to points on the branch are shown in figure 5.17.

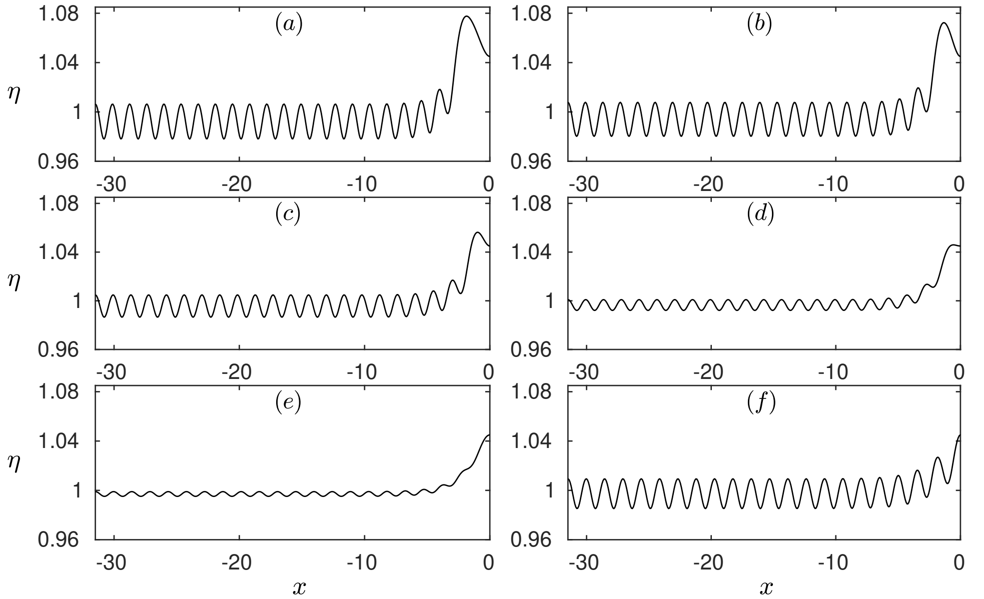

Figure 5.17: Generalised solitary waves corresponding to points $(a) - (f)$ in figure 5.16. Only half a wavelength is shown.

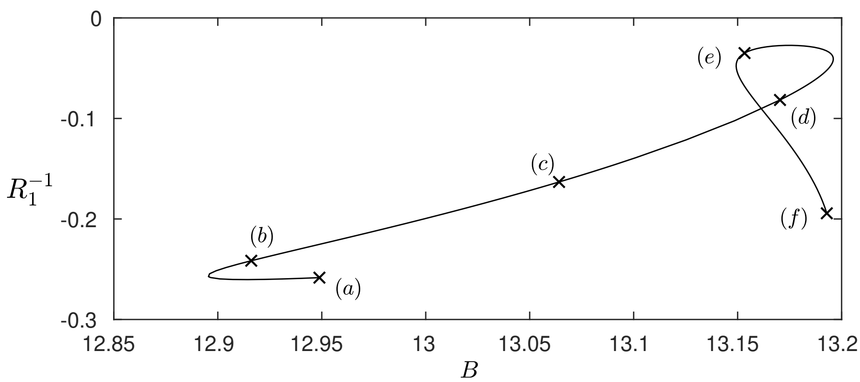

Figure 5.18: Plot of the curvature of the free surface R_1^{-1} (equation (5.60)) in the far-field against B for the generalised solitary waves. R_1^{-1} remains strictly negative, meaning none of these solutions are pure solitary waves. The points $(a) - (f)$ refer to the solutions shown in figure 5.17 .

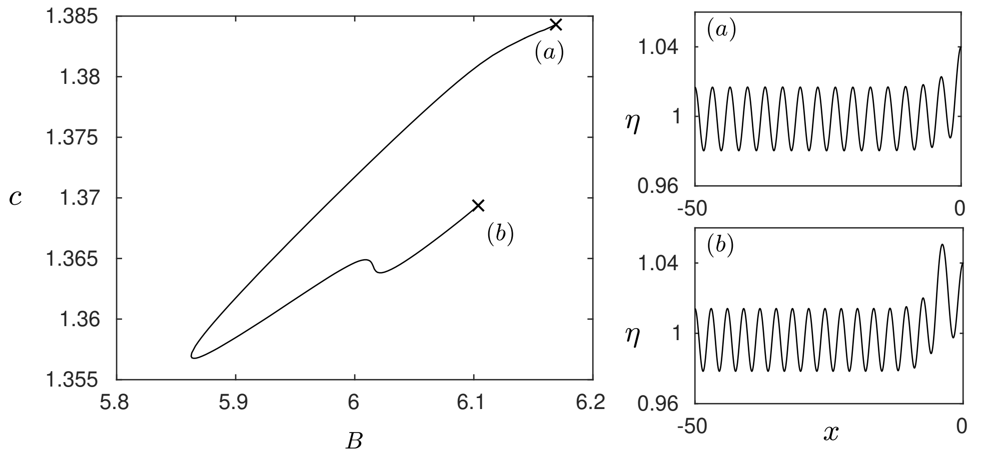

Figure 5.19: Two-layer generalised solitary wave branch for $d = 1.5/3.3$, $D = 3$, $\eta(0) = 1.04$ and $\lambda = 100$. Two profiles corresponding to points (a) and (b) are shown. Only half the solution is shown in figures (a) and (b).

$c(\widehat{\lambda}) = c_0$. These waves were computed by Vanden-Broeck [84] and Champneys et al. [20] for gravity-capillary waves. We present a generalised solitary wave solution branch for the one-layer problem in figure 5.16, and the corresponding profiles in figure 5.17. We fix $\eta(x = 0) = 1.045$, and vary the speed of the wave. Due to the imposed symmetry, and since these solutions are finite wavelength approximations of generalised solitary waves, the far-field wavetrain ends in either a peak or a trough. We can see in figure 5.17 (by looking at the leftmost point of the profile) that in this case it is a peak. As with gravity-capillary waves, the branches start and end on solutions with larger amplitude far-field waves. For solutions in between the ends of the branch, the amplitude of the waves in the far-field is smaller (see figure 5.17). No solutions with a flat far-field were found. This is shown numerically in figure 5.18, where the reciprocal of the radius of curvature of the free surface, given by

$$R_1^{-1} = -\frac{\eta_{xx}}{(1 + \eta_x^2)^{1/2}}, \tag{5.60}$$

is shown to be strictly negative when evaluated at the furthest meshpoint in the far-field for all solutions on the branch. The KdV equation of Rannacher and Engel [72] predicts pure elevation solitary waves in this region, and hence fails to accurately

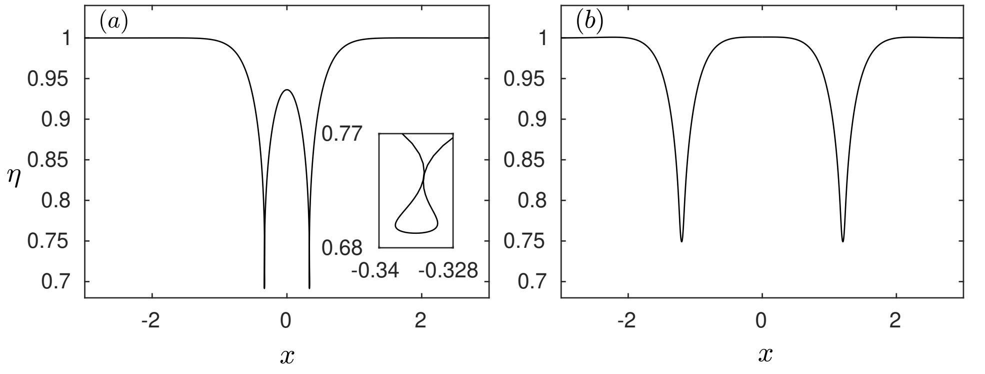

Figure 5.20: One-layer solitary wave packets for $d = 1.5/3.3$, $B = 20$. Figure (a) is the limiting configuration of the depression branch and figure (b) the furthest point computed on the elevation branch. The inset of figure (a) shows the trapped bubble.

describe fully nonlinear solutions when $B > B_2$. Generalised solitary wave branches with the same behaviour were found for the two-layer problem, where one such branch is presented in figure 5.19.

Although there do not exist pure solitary waves bifurcating from zero amplitude at c_0, there do exist branches of solitary wave packets bifurcating from a linear wavetrain of wavenumber k_m at c_m. Use of the chain rule shows that at the minimum of the dispersion relation, the group velocity of linear waves is equal to the phase velocity. This allows the existence of solitary wave packets (Akylas [4]), in particular one depression branch and one elevation branch. At small amplitudes, these waves are described by a Nonlinear Schrödinger Equation, as derived for the one-layer model (assuming $d = 0$) by Groves and Nilsson [45]. Fully nonlinear solutions for the one-layer problem were computed numerically by BP. They found that as one increases the amplitude along the depression branch, the solutions begin to overturn, forming a trapped bubble. Repeating the numerical scheme for variable parameter values, we found the overturned bubble does not have to occur at the point of symmetry, but can also appear at some other point in the profile, as seen in figure 5.20a. For no parameter values tested did the solution branches approach a static configuration. This is in agreement with section 5.5, where the range of static solutions found did not include solitary waves with decaying oscillating tails.

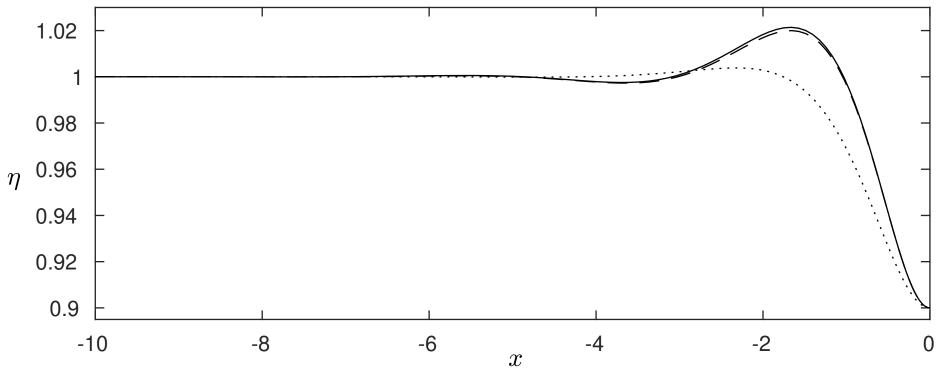

Figure 5.21: Two-layer solitary wave packets with amplitude $A = -0.1$, for $d = 1.5/3.3$, $B = 8.3$, and $D = 2$ (dotted curve), $D = 4$ (dashed curve) and $D = 8$ (solid curve). Only one half of the profile is shown. The dashed and solid curves almost overlap.

BP conjecture that the elevation branches overturn and form trapped bubbles as well, although they note care must be taken since this conjecture was mistakenly made by Vanden-Broeck and Dias [88] for two-dimensional gravity-capillary elevation solitary wave packets. The more accurate computations of Dias et al. [30] demonstrated that these solution branches actually turn around and form many loops in the (c, η) space. Figure 5.20b shows a solution from the elevation branch, computed as far along the branch as possible. Both the elevation and depression solution from figure 5.20 were computed with $N = 30$ and $M = 900$. These solutions also exist for the two-layer model. This is expected, since the same phenomena occurs for two-dimensional internal gravity-capillary waves (Laget and Dias [56]). In figure 21, we show a two-layer depression solitary wave packet, with varying values of D. As D gets larger, the variation in the profiles becomes small. It follows that one could approximate the case of a surrounding fluid of infinite radius ($D \to \infty$) by taking a suitably large value of D. This is further confirmed by considering the dispersion relation (5.23) for various values of D, as shown in figure 5.22. It can be seen that the dispersion relations for $D = 8$ and $D \to \infty$ are very similar, the largest difference occurring at $k \to 0$ (the long wave speed).

There are difficulties with comparing the two-layer numerical results of this chap-

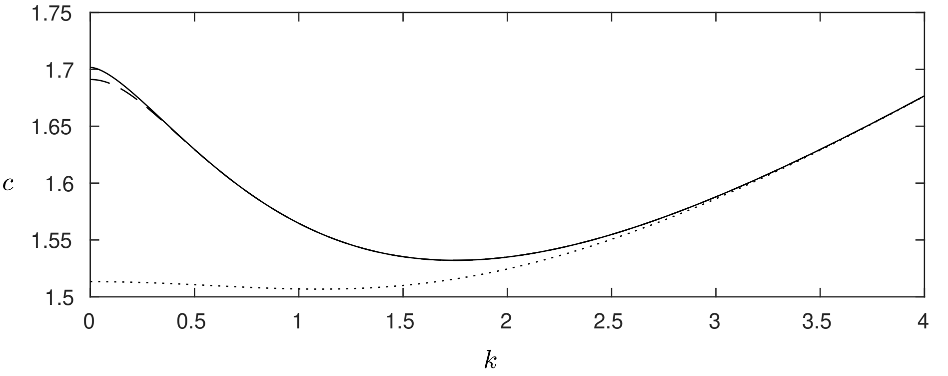

Figure 5.22: Two-layer dispersion relation, given by equation (5.23), with $d = 1.5/3.3$, $B = 8.3$, and $D = 2$ (dotted curve), $D = 8$ (dashed curve) and $D \to \infty$ (solid curve).

ter with the experimental data of Bourdin et al. [15], as was discussed in BP. For completeness, we highlight the key points here. Bourdin *et al.* coated a copper wire of radius 1.5mm with a ferrofluid jet of radius 3.8mm when creating periodic waves, and 3.3mm when creating solitary waves. The ferrofluid was surrounded in freon of almost equal density, and the whole system was contained in a cuboid container with a 40mm $\times$ 40mm side and 30mm length. The fact that axisymmetric profiles were witnessed in a cuboid container implies that the effects of the container were negligible. Hence, to compare our model with these experimental results, we wish to consider the case of a surrounding fluid of infinite radius. As shown above, this can be approximated by considering a large value of D. Bourdin *et al.* observed pure solitary waves: a depression wave for magnetic Bond number $B = 8.1$ and a wave of elevation for $B = 10.5$. As noted by BP, and confirmed by the results in this chapter, one would expect to see solitary wave packets or generalised solitary waves for such parameter values, due to the occurrence of minimum in the dispersion curve. This is at odds with the pure elevation and depression solitary waves witnessed by Bourdin *et al.* However, we suspect the inclusion of the effects of the second fluid are not negligible. Evidence for this was given by BP, who showed that the agreement between the experimental and theoretical dispersion curve improved when taking the second fluid to have equal as opposed to negligible density. Given the wealth of so-

		M		
		75	150	300
	25	0.6925392	0.6925667	0.6925733
N	50	0.6927149	0.6927432	0.6927502
	100	0.6927601	0.6927886	0.6927956
	200	0.6927716	0.6928001	-

Table 5.1: Values of the amplitude A up to 7 decimal places for the one-layer solution with parameter values $B = 3$, $d = 1.5/3.8$, and $c = 0.7$ for different mesh sizes. Issues with memory (the size of the Jacobian used in Newton's method becomes very large) deny the possibility of computing a solution with $N = 200$ and $M = 300$.

lutions found for the two-layer model, and the discrepancy between the experiments and fully nonlinear calculations, it would be of interest to see further experimental results on the problem, looking at a wider range of parameter values.

In the following section, we discuss the numerical errors that occur in our finite difference scheme.

5.6.3 Numerical errors

In the results of this chapter, we have computed some intricate profiles, including overhanging structures, and solutions which come very close to a boundary. To ensure there were sufficient meshpoints at areas of rapidly changing ϕ_1 or ϕ_2, we often performed the coordinate transformations (5.52). Below, we discuss the order of the errors seen for both the one-layer and two-layer model, where we consider large amplitude solutions.

Consider highly nonlinear solutions close to the end of the $B = 3$ branch of figure 5.6a. These solutions have overhanging structures, as was seen in the solution at the end of the branch in figure 5.9. Fixing the phase speed to $c = 0.7$ and allowing the amplitude to vary, table 5.1 shows the amplitude obtained for different values of M and N. The table demonstrates the convergence of the numerical method for these extreme overhanging profiles. Recalling the mesh spacing (5.41)-(5.43), denote the

		M		
		75	150	300
	10, 20	0.1094310	0.1101299	0.1102692
N, P	20, 40	0.1094107	0.1101119	0.1102511
	40, 80	0.1094046	0.1101077	0.1102469
	80, 160	0.1094025	0.1101066	-

Table 5.2: Values of the speed c for the two-layer elevation solitary wave solution on the $B = 1.4$ branch of figure 5.11 with amplitude $A = 0.9$.

distance between two mesh points in t as k, in ϕ_1 and ϕ_2 as h, and in s as l. All derivatives were approximated using second order difference equations in h, k and l. Fixing k, if we denote the value of the amplitude A as $h \to 0$ as $\widehat{A_k}$, and the value of the finite difference scheme for some values of h and k as $A_{h,k}$, then denoting the absolute error as $E_{h,k} = |A_{h,k} - \widehat{A_k}|$, one can seek the order of error in the form

$$E_{h,k} = a_1 h^\alpha + O(h^\beta), \tag{5.61}$$

where a_1, α and $\beta > \alpha$ are real constants. One can then show that

$$\alpha \approx \log_2 \left(\frac{E_{2h,k} - E_{4h,k}}{E_{h,k} - E_{2h,k}} \right). \tag{5.62}$$

Noting that doubling M is equivalent to halving h, using the values from table 5.1 in equation (5.62) , we find that $\alpha \approx 2$. Similarly, fixing h and varying k, one finds that

$$E_{h,k} = a_2 k^\gamma + O(k^\delta), \tag{5.63}$$

where a_2, γ and $\delta > \gamma$ are again real constants. From table 5.1, we find that $\gamma \approx 2$. Hence, the finite difference scheme appears to be second order accurate in h and second order accurate in k, which agrees with the use of second order difference equations.

A similar result is found for the two-layer model. For example, consider a large amplitude pure elevation solitary wave solution. Table 5.2 shows the value of c obtained for the solution with amplitude $A = 0.9$ on the $B = 1.4$ branch of figure 5.11, for various values of M, N and P. We again find that the solution is approximately second order accurate, as can be seen by substituting the values from table 5.2 into equations (5.61) and (5.63).

5.7 Conclusion

In conclusion, we have presented a numerical model capable of finding stable travelling wave solutions on a ferrofluid jet, where the surrounding fluid is assumed to be of zero density or equal density to that of the ferrofluid. The results from the classical problem of two-dimensional gravity-capillary waves have helped predict the behaviour of the solution space for various parameter values. The importance of the existence of a minimum in the linear dispersion relation has been demonstrated, and periodic, solitary and generalised solitary waves have been found for both models. The stability of the solutions is as of yet unknown, and would require a time dependent numerical scheme to find out, as done by Guyenne and Părău [47] for pure solitary waves on the one-layer model. As well as time dependent models, it would be interesting to see if symmetry breaking bifurcations can be found with the numerical scheme described in this chapter (by removing the imposed symmetry condition), as has been found by Gao et al. [38] for gravity-capillary waves.

Chapter 6

Future work

In this chapter, we will discuss the ways in which the models in this thesis could be improved, as well as some new projects.

6.1 Flow from a pipe onto a plate

In chapter 3, we computed two-dimensional flows exiting a pipe onto a flat plate. We repeated the computations of Christodoulides and Dias [21], where we improved the series representation of the complex velocity ξ by including the singularity at $t = 1$. This was shown by the order of the coefficients in table 3.2. These computations were for zero surface tension: it would be of interest to see what effect the inclusion of surface tension has on the solution space. The singularity structure in the far-field is richer when surface tension is included, as discussed in section 3.4.2. In particular, when the roots are complex, we expect the flow to decay with oscillations in the far-field.

We find it beneficial to rescale the problem such that the depth and speed of the uniform stream in the far-field are unity. This allows us to fix the Froude number in the far-field (denoted F_f in chapter 3) to be less than one, a condition required to avoid linear waves. In the code, we allow the angle μ at the separation point to vary. We initially attempted some computations including surface tension with the series (3.60). For zero surface tension, although the singularity at $t = 1$ (the far-field) disrupts the convergence of the series, it still produces graphically accurate solutions (as was done by Christodoulides and Dias). However, when surface tension is included, it is found that the solution obtained becomes dependent on N, and hence the method is no longer convergent.

Therefore, we will try to use a series of the form (3.59). Note that, when the leading order singularity is the conjugate pair (case 4 of figure 3.12), we will require a series of the form

$$\xi(t) = \left(\frac{t_B - t}{t_B}\right)^{1-\beta/\pi} (t+1)^{2-2\mu/\pi} \times \exp\left(A\left[(1-t)^{2\lambda} + (1-t)^{2\bar{\lambda}} - 2\right] + \sum_{n=1}^{N} a_n t^n\right). \tag{6.1}$$

This is to ensure that ξ satisfies the boundary conditions for $t \in [-1, 1]$. We are yet to achieve convergent results. This is a subject of current investigation.

6.2 Other axisymmetric models

There are a variety of other axisymmetric flows one could attempt to solve using the methodology seen in this thesis. For example, related to the previous model, one could consider axisymmetric flow exiting a cylindrical pipe onto an infinite flat plate. The flow configuration is shown in figure 6.1a. One must find a suitable treatment of the singularity, where the flow exists the pipe and forms a free surface. The stagnation point singularity can be managed via the function splitting method, using equation (4.20).

When both surface tension and gravity are ignored, Mackenroth [59] and Turenne and Fiset [79] used the finite difference scheme of Woods and Jeppson to compute

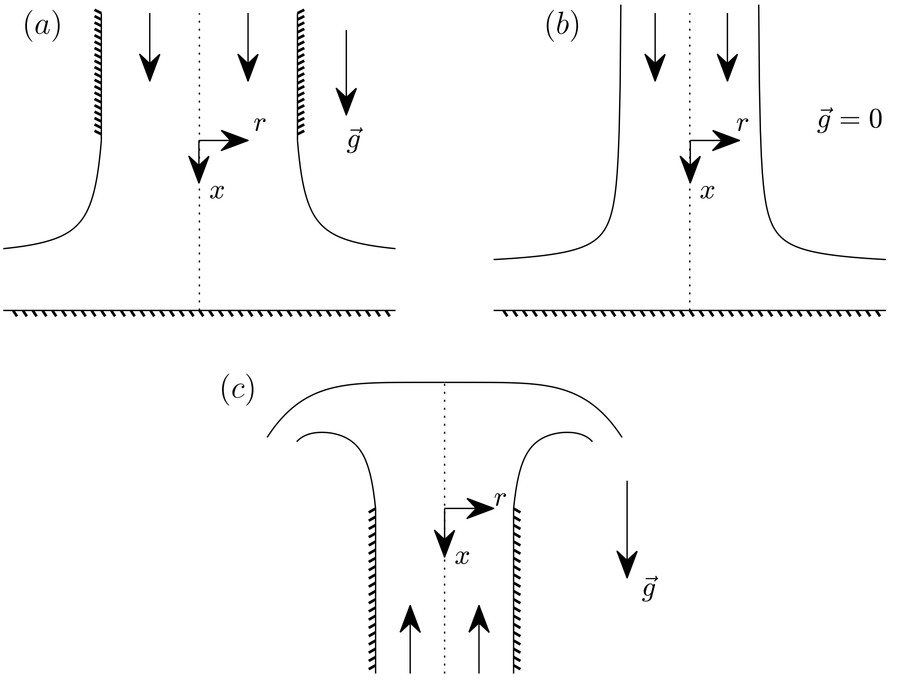

Figure 6.1: Axisymmetric flow configurations. The unlabeled arrows show the flow direction. The dotted curve is the axis of rotation, the cylindrical coordinates are given by (x, r), while $\vec{g}$ is gravity.

a free streamline jet hitting a plate. The flow configuration in axisymmetric coordinates is shown in figure 6.1b. In both the above references, a crude mesh was used, and Mackenroth stated that the largest numerical errors were seen close to the stagnation point singularity. It is not clear if their codes would converge upon mesh refinement, where approximations of derivatives close to the singularity would become problematic. One could improve on their numerical scheme by making use of the function splitting procedure to regulate errors near the stagnation point.

One could also consider the flow exiting a pipe aimed upwards, under the effect of gravity. The fluid exits the pipe, and forms a falling jet, bounded either side by a free surface. A schematic of the flow is shown in figure 6.1c. The two-dimensional analogue of this model was solved using boundary integral methods by Dias and Vanden-Broeck [28]. The limiting case, where the pipe is taken infinitely far away from the jet, was later solved using a finite difference scheme by Vanden-Broeck [86]. A review of two-dimensional flows of this type is given by Dias and Vanden-Broeck

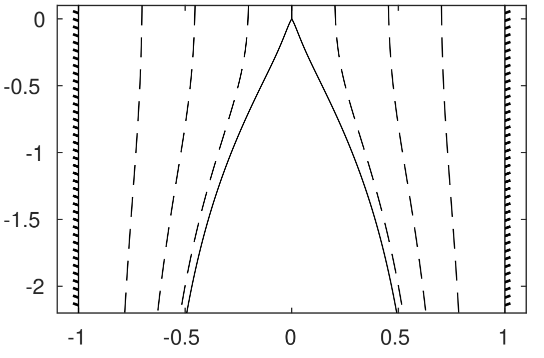

Figure 6.2: A cusped bubble obtained for $F = 2$ using the finite difference scheme without removing the singularity, with a crude mesh. This profile is not a solution of a convergent numerical scheme. Some streamlines are shown with dashed curves.

[29].

Finally, when computing the surface tension free solution space of Taylor bubbles in chapter 4, we were unable to obtain any solutions for $F > F_C$. We suspect these solution are cusped bubbles. This singularity is weaker than the stagnation point singularity of the smooth and pointed bubbles. This motivated attempting the finite difference method without the singularity removal procedure described in section 4.3.1. Solutions were obtained for crude meshes. However, the method became divergent as the mesh was refined. The same results were found by Vanden-Broeck [83], whose method suffers the same fate under mesh refinement. A local representation of the flow field about the cups would allow for the method to regulate the singularity. Figure 6.2 shows a solution found for a crude mesh, with no treatment of the cusp singularity. We stress here that this is **not** sufficient proof of the behaviour of the solutions for $F > F_C$, and it would be interesting to see solutions in this parameter regime computed using a convergent numerical method.

6.3 Electrified axisymmetric jet

Similar to the topic of chapter 5, researchers have explored the stabilisation and destabilisation of a fluid column under the effect of an electric field. The model in question concerns a perfect conducting fluid, surrounded by a dielectric gas with electric permittivity ϵ. An electric field is created by applying a potential to an axial hollow electrode, containing the conducting jet. An electrified jet in this configuration has been considered by a variety of authors. A linear dispersion relation has been derived by Melcher [62], Schneider et al. [75], and Artana et al. [7]. It is found that the electric field stabilises the long wave Rayleigh-Plateau instability, but in turn destabilises short waves. The ability to modify the dominant destabilising mode allows one to regulate droplet size formation in an droplet generator (Crowley [24]), as well as having applications in particle sorting (Bonner et al. [14]) and fuel injection.

Setiawan and Heister [76] derived a fully nonlinear time-dependent numerical method to investigate the late stages of the instability. The numerical scheme was a boundary integral method, making use of Green's functions. They found that the electric field steepens the interface, and the droplets become squeezed. More recently, a KdV equation was derived by Wang et al. [92]. They found both elevation and depression solitary wave solutions, the existence of which depended on the parameters. Increasing the strength of the electric field took one from a regime where the KdV emits depression solitary waves to one where it emits elevation solitary waves.

Fully nonlinear computations on this model were done by Grandison et al. [44], who used the finite difference scheme discussed in this thesis by. However, the linear theory of the paper has errors, and there is a lack of clarity in the description of the numerical method used. Recently, we have explored this problem, in a sense providing a correction to the above paper.

6.3.1 Formulation

We consider an axisymmetric column of a perfectly conducting fluid with constant density ρ and undisturbed radius R. The column of fluid is surrounded by a

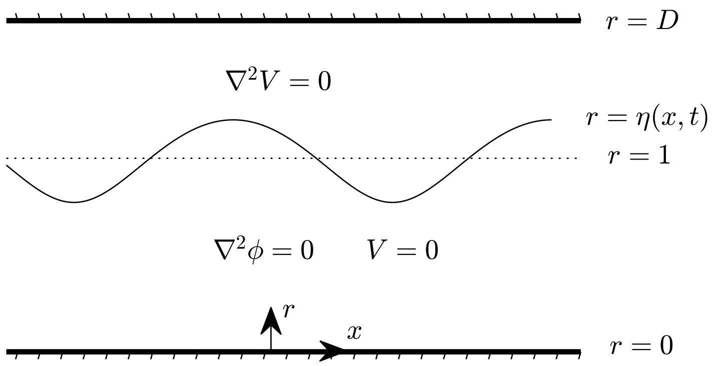

Figure 6.3: Formulation of the problem in cylindrical coordinates.

dielectric passive gas, with electric permittivity ϵ. The whole system is contained inside an axisymmetric hollow electrode of radius D. We choose a cylindrical coordinate system (x, θ, r), where x is parallel to the electrode, and r is the radial coordinate. We denote the interface $r = \eta(x,t)$. The flow configuration is shown in figure 6.3.

The conducting fluid is held at zero voltage, while the outer electrode is held at a constant voltage potential V_0. The potential difference results in an electric field in the annular region between the conducting fluid and the electrode. We assume that the magnetic conductivity of both the fluid and gas are small, such that the electrostatic approximation of Maxwell's equations are sufficient (Papageorgiou [65]). Hence, we have that the electric field in the dielectric $\boldsymbol{E}$ is an incompressible and irrotational vector field. We write $\boldsymbol{E} = -\nabla V$, where V is the electric potential. The above assumptions imply that V satisfies the Laplace equation. The interface and electrode are both equipotential surfaces of V.

As well as the electrostatics in the gaseous dielectric, we must also solve the hydrodynamical problem associated with the conducting fluid. We write the velocity vector $\boldsymbol{u} = (u, v)$ in (x, r). We will consider the fluid to be inviscid, and the flow incompressible and irrotational. Hence, we write $\boldsymbol{u} = \nabla\phi$. Consider a periodic disturbance with wavelength λ travelling at constant speed c. Taking λ as the reference length scale, c as the reference velocity, and V_0 as the reference voltage, we find a system of equations given by

$$\nabla^2 V = 0, \qquad \text{for } \eta(x,t) < r < D, \tag{6.2}$$

$$\nabla^2 \phi = 0, \qquad \text{for } 0 < r < \eta(x,t), \tag{6.3}$$

$$V = 1, \qquad \text{for } r = D, \tag{6.4}$$

$$V = 0, \qquad \text{for } r = \eta(x,t), \tag{6.5}$$

$$\phi_r = 0, \qquad \text{for } r = 0, \tag{6.6}$$

$$\phi_r = \eta_z \phi_z, \qquad \text{for } r = \eta(x,t), \tag{6.7}$$

and

$$\frac{1}{2}q^2 + \gamma\kappa - \frac{E_b}{2}\left(\nabla V \cdot \widehat{\boldsymbol{n}}\right)^2 = P, \qquad \text{for } r = \eta(x,t),, \tag{6.8}$$

where $\widehat{\boldsymbol{n}}$ is the unit normal vector to the interface, $q = |\nabla\phi|$, κ is the mean curvature, and γ and E_b are nondimensional parameters, given by

$$\gamma = \frac{T}{\rho\lambda c^2}, \qquad E_b = \frac{\epsilon V_0^2}{\rho c^2 \lambda^2}. \tag{6.9}$$

Here, equations (6.2) and (6.3) are the governing equations, equations (6.4) and (6.5) the equipotential conditions on the electrode and interface respectively, and equations (6.6) and (6.7) are the kinematic boundary conditions of the fluid flow on the axis of rotation and interface respectively. Equation (6.8) is the dynamic boundary condition, given by evaluating Bernoulli's equation on the interface. It is similar to equation (2.12), where we have ignored gravity. This can be achieved experimentally by performing microgravity experiments (for example Burcham and Saville [18] performed experiments concerning electrified bridging on a space station). This completes the formulation of the problem. It is left to find the functions ϕ and V such that equations (6.2) and (6.3) are satisfied in their respective domains, subject to boundary conditions (6.4)-(6.8).

6.3.2 Numerical method

We use a finite difference scheme, similar in many ways to the numerical method used for the two-layer ferrofluid problem. We solve for r as a function of (ϕ, ψ) in the inner domain. For the outer domain, we solve for r as a function of (W, V), where W is defined by

$$W_x = rV_r, \qquad W_r = -rV_x. \tag{6.10}$$

The variable W has the same role as the Stokes streamfunction ψ in relation to the velocity potential ϕ: the relations (6.10) follow from the fact that the vector field $\boldsymbol{E} = -\nabla V$ is incompressible and irrotational. One can then transform the equations such that r in the dependent variable and W and V are the independent variables. Denoting the value of ψ on the axis of rotation and interface as 0 and Q respectively, the flow domain in the potential spaces becomes

$$\Omega_1 = \left\{\phi \in \left[-\frac{1}{2}, 0\right], \psi \in [0, Q]\right\}, \tag{6.11}$$

$$\Omega_2 = \left\{W \in \left[-\frac{W_0}{2}, 0\right], V \in [0, 1]\right\}. \tag{6.12}$$

Here, W_0 is unknown and must be found as part of the solution. The obvious advantage to working in the (W, V)-space is that the interface is fixed to $V = 0$, as shown in figure 6.4. One can then derive a system of equations, taking r as the dependent variable of (ϕ, ψ) in Ω_1 and (W, V) in Ω_2. We perform the coordinate transform $\psi = t^2$, and the two spaces are discretised as follows:

$$\phi_i = -\frac{M-i}{2(M-1)}, \qquad W_i = W_0\phi_i \qquad i = 1, \cdots, M, \tag{6.13}$$

$$t_j = Q^{1/2}\frac{j-1}{N-1}, \qquad j = 1, \cdots, N, \tag{6.14}$$

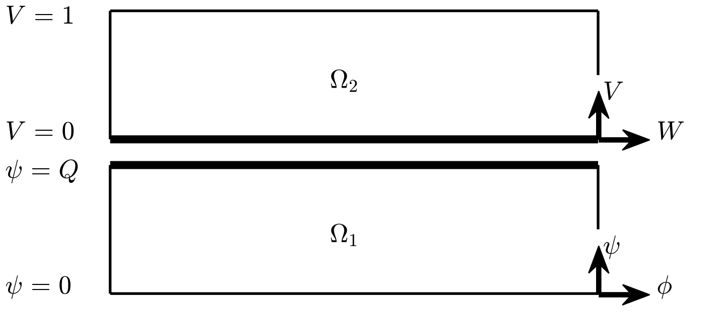

Figure 6.4: Flow domain in the potential space.

$$V_j = \frac{j-1}{N-1}, \qquad j = 1, \cdots, P. \tag{6.15}$$

Derivatives are computed using second order difference equations. We satisfy the governing equation at interior nodes, (6.8) on the interface, and $r = 0$ and $r = D$ at $\psi = 0$ and $V = 1$ respectively. Interpolation in x on the interface is then used to couple the systems via the dynamic boundary condition (6.8).

6.3.3 Results

We fix a value of Q, E_b, and the amplitude A, given by

$$A = \eta(0) - \eta(\lambda/2). \tag{6.16}$$

We then used the above numerical scheme to compute small and medium amplitude periodic waves. The linear dispersion relation is found to be

$$\gamma = \frac{kR^2\left[I_0(kR)(\log D)^2 - E_b I_1(kR)\left(S + \frac{1}{kR}\right)\right]}{(\log D)^2\left(R^2k^2 - 1\right)I_1(kR)}, \tag{6.17}$$

where

$$S = \frac{I_1(kR)K_0(kD) + I_0(kD)K_1(kR)}{I_0(kR)K_0(kD) - I_0(kD)K_0(kR)}. \tag{6.18}$$

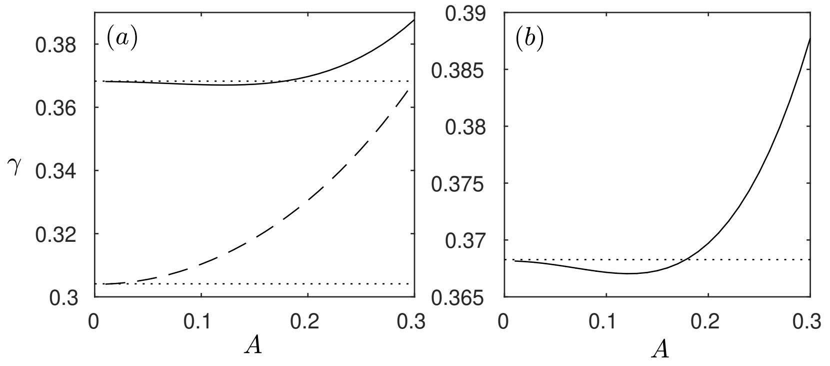

Figure 6.5: Periodic solution branches for $E_b = 10^{-6}$ (dotted curve) and $E_b = 0.5$ (solid curve). The dispersion relation (6.17) for a given E_b is the dashed line. Figure (b) shows a blown up image of the $E_b = 0.5$ branch.

Here, I_n and K_n are the modified Bessel functions of the first and second kind of order n respectively. This disagrees with equation (34) found in Grandison et al. [44], who state that

$$\gamma = \frac{kR^2\left[I_0(kR)(\log D)^2 + E_b I_1(kR)S\right]}{(\log D)^2\left(R^2k^2-1\right)I_1(kR)}. \tag{6.19}$$

We found that the dispersion relation (6.17) agrees with previous literature (for example, see Wang et al. [92]). We computed some periodic solution branches for $Q = 1/(2\pi^2)$ with $E_b = 10^{-6}$ and $E_b = 0.5$, as shown in figure 6.5. These are the parameter values used in figure 6 in the paper by Grandison et al. It was found that the results of the numerical method agreed with the linear dispersion relation (6.17) for small amplitudes. We also found that the $E_b = 0.5$ branch does not monotonically increase in γ as one increases the amplitude A, where A is defined using equation (5.49). As we increase the amplitude further, it is the case that the interface in either domains (Ω_1 and Ω_2) start to deviate. This problem did not occur for the two-layer ferrofluid problem. As it stands, this issue denies us the ability to compute large amplitude solutions for this model. This may lead one to question the validity of the numerical scheme. In table 6.1, we present some values of γ obtained for the $A = 0.1$ solution on the $E_b = 0.5$ branch of figure 6.5. Using equations similar to

		M		
		75	150	300
	10, 50	0.36546	0.36541	0.36540
N, P	20, 100	0.36688	0.36683	0.36682
	40, 200	0.36721	0.36715	-

Table 6.1: Values of γ up to 5 decimal places for the $A = 0.1$ solution from the branch shown in figure 6.5.

(5.61), we find the method approximately second order accurate in differences in ϕ, W, t and V.

This is a subject of current investigation.

6.4 Two-dimensional electrohydrodynamical capillary-gravity waves

Finally, we will briefly discuss a recent joint project with Dr Tao Gao on electrohydrodynamical gravity-capillary waves propagating under vertical electric fields. The model can be seen as a generalisation of previous works, a recent and comprehensive review of which was published by Papageorgiou [65]. The general set up consists of two immiscible dielectric fluids with different electric permittivities, with an interface in between. To reduce the complexity of the problem, some assumptions were made in previous works. For example, Papageorgiou et al. [67] and Papageorgiou and Vanden-Broeck [66] made the assumption that the upper layer is much larger than the lower one. Boussinesq-type long wave models were derived in the former whereas a boundary integral method was used to compute fully nonlinear solutions in the latter. Another common assumption is to consider the case when one of the layers is a perfect conductor. Korteweg de-Vries (KdV), modified KdV, forced KdV and KdV-Benjamin-Ono equations were derived respectively by Easwaran [35], Hunt and Vanden-Broeck [49], Perelman et al. [68], and Gleeson et al. [43] in the case of a layer

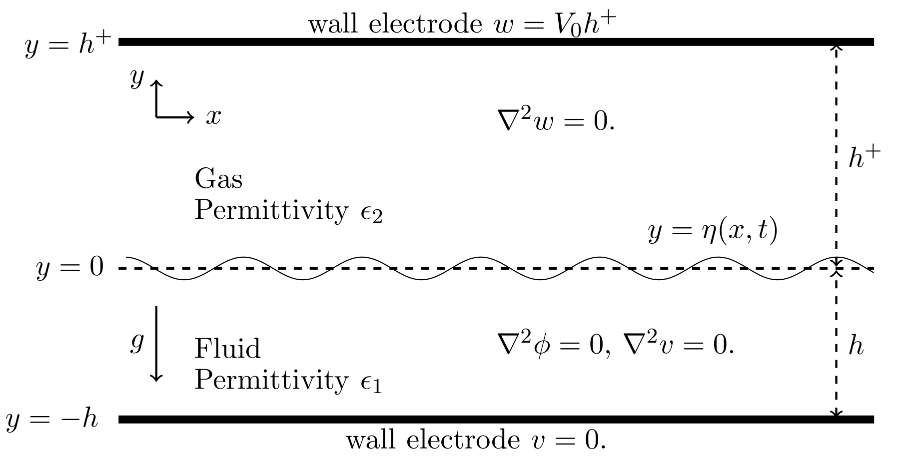

Figure 6.6: Configuration of the problem from section 6.4. Gravity acts in the negative y-direction. We denote the equation of the unknown free surface as $y = \eta(x,t)$.

of conducting fluid on bottom and a dielectric on top. On the other hand, assuming instead the upper region is a conducting gas, fully nonlinear travelling solitary waves on a dielectric fluid of infinite and finite depth respectively as well as their dynamics based on a time-dependent hodograph transformation technique are found in Gao et al. [39] and Gao et al. [40]. To our knowledge, no fully nonlinear computations have been achieved for the general set up of two dielectrics with two finite depth layers so far.

6.4.1 Formulation

We consider the two-dimensional irrotational flow of an inviscid incompressible fluid of finite depth that is bounded below by an electrode and above by a hydrodynamically passive region, which in turn is bounded above by an electrode (see figure 6.6). The fluid and the passive gas are assumed to be perfect dielectrics with permittivity ϵ_1 and ϵ_2 respectively. The problem can be formulated by using Cartesian coordinates with the y-axis directed vertically upwards and $y = 0$ at the mean level. We take h as the undisturbed depth of the fluid, and h^+ as the undisturbed depth of the passive gas. The gravity g and the surface tension σ are both included in the formulation. The deformation of the free surface is denoted by $\eta(x,t)$. We denote the voltage potential in the fluid as v, and in the gas as w. Without loss of generality, we choose $v = 0$ on the bottom electrode. Continuity of the tangential component of the electric fields results in the condition that v and w are equivalent on the free-surface, up to an arbitrary constant, which without loss of generality we take to be zero. The potential on the upper electrode w is then a fixed parameter of the problem, which we shall denote $w = V_0 h^+$. This choice of w on the upper electrode is chosen such that, in the case where $h^+ \to \infty$, we have that the electric field approaches a uniform vertical electric field with strength V_0. Since the fluid motion can be described by a velocity potential function $\phi(x,y,t)$, the governing equations can then be written as

$$\nabla^2\phi = 0, \qquad \text{for} \quad -h < y < \eta(x,t), \tag{6.20}$$

$$\nabla^2 v = 0, \qquad \text{for} \quad -h < y < \eta(x,t), \tag{6.21}$$

$$\nabla^2 w = 0, \qquad \text{for} \quad \eta(x,t) < y < h^+, \tag{6.22}$$

$$\eta_t = \phi_y - \phi_x\eta_x, \qquad \text{on} \quad y = \eta(x,t), \tag{6.23}$$

$$\phi_y = 0, \qquad \text{on} \quad y = -h. \tag{6.24}$$

$$w = V_0 h^+, \qquad \text{on} \quad y = h^+, \tag{6.25}$$

$$v = 0, \qquad \text{on} \quad y = -h, \tag{6.26}$$

$$v_x + \eta_x v_y = w_x + \eta_x w_y, \qquad \text{on} \quad y = \eta(x,t), \tag{6.27}$$

$$v_y - \eta_x v_x = \Lambda\left(w_y - \eta_x w_x\right), \qquad \text{on} \quad y = \eta(x,t), \tag{6.28}$$

and

$$\phi_t + \frac{1}{2}|\nabla\phi|^2 + gy - \frac{T}{\rho}\frac{\eta_{xx}}{(1+\eta_x^2)^{3/2}} + \sigma = B, \quad \text{on} \quad y = \eta(x,t), \tag{6.29}$$

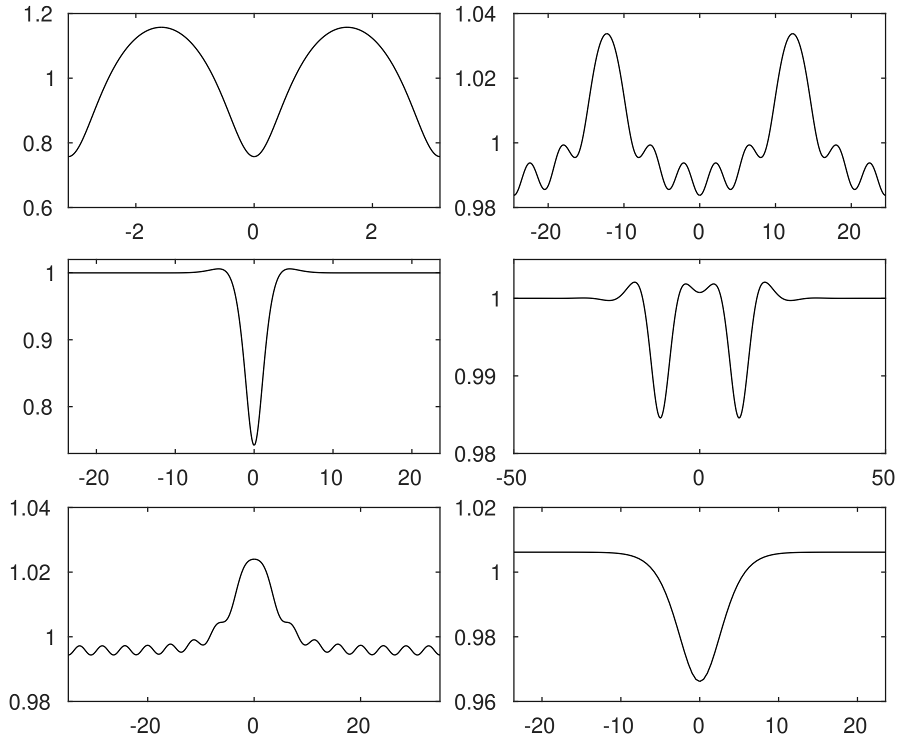

Figure 6.7: Some fully nonlinear solutions found with $E_b = 1.5$, $h^+ = 1.5$, and varying values of τ.

where the subscripts denote partial derivatives, B is the Bernoulli constant and σ is the Maxwell stress given by

$$\sigma = -\frac{\epsilon_1}{\rho(1+\eta_x^2)}\left[\frac{1}{2}(1-\eta_x^2)(v_x^2 - v_y^2 - \Lambda(w_x^2 - w_y^2)) + 2\eta_x(v_x v_y - \Lambda w_x w_y)\right], \quad (6.30)$$

with $\Lambda = \epsilon_2/\epsilon_1$ being the ratio of the permittivity from two layers. The last three terms of (6.29) are the forces due to gravity, the Maxwell stresses due to the electric field, and surface tension. Equations (6.23) and (6.24) are the kinematic boundary conditions on the interface and bottom electrode respectively. The conditions (6.25) and (6.26) fix the electric potentials at the electrodes. Finally, continuity of the tangential components of the electric field and continuity of the normal component of the displacement field is given by (6.27) and (6.28) respectively.

By choosing h, $\sqrt{h/g}$ and V_0 as the reference length, time and voltage potential, the bottom is at the level $y = -1$, and the system is still governed by the Laplace equations but with the dynamic boundary condition (6.29) becoming

$$\phi_t + \frac{1}{2}|\nabla\phi|^2 + \eta + \sigma - \tau\frac{\eta_{xx}}{(1+\eta_x^2)^{3/2}} = B \qquad \text{on} \quad y = \eta(x,t), \tag{6.31}$$

and

$$\sigma = \frac{E_b(\Lambda - 1)}{2\Lambda(1+\eta_x^2)}\left[(\Lambda + \eta_x^2)v_x^2 + (\Lambda\eta_x^2 + 1)v_y^2 + 2(\Lambda - 1)v_x v_y \eta_x\right], \tag{6.32}$$

where τ is the Bond number and E_b is the electric Bond number defined by

$$\tau = \frac{T}{\rho g h^2}\,, \quad E_b = \frac{\epsilon_1 V_0^2}{\rho g h^3}\,. \tag{6.33}$$

The project concerns fully nonlinear numerical computations to the solutions of the above system. A boundary integral method, similar to the one found in Papageorgiou and Vanden-Broeck [66], is used. Details are omitted here. A variety of solutions have been computed: periodic waves, Wilton ripples, solitary wave packets, pure solitary waves and generalised solitary wave solutions have all been found. Some example profiles are shown in figure 6.7. In the future, we wish to derive some long wave models, and provide comparisons between the weakly nonlinear solutions and the fully nonlinear computations.

Chapter 7

Conclusion

In conclusion, we have presented novel solutions to a variety of steady potential flows. The main focus has been axisymmetric models, a field which has historically received less attention that its two-dimensional counterpart. Using the finite difference scheme derived by Woods [94] and Jeppson [51], we have provided the strongest evidence to date that the higher order branches ($F_2(\alpha)$, $F_3, (\alpha) \cdots$) of smooth axisymmetric Taylor bubbles approach F^* as surface tension is taken to zero. Following from the work of Blyth and Părău [13], with a suitable modification of the numerical scheme, we have found a variety of solutions of travelling waves on a ferrofluid jet for the one-layer and two-layer models. We also found novel solutions for two-dimensional flow exiting a pipe onto a wedge, and improved the convergence of the numerical method deployed by Christodoulides and Dias [21] to compute flow impacting a flat plate. Finally, we have highlighted areas where the methods used in this thesis could be applied to solve new problems.

Appendix A

Errors in function splitting

It is necessary to discuss the errors associated with the function splitting procedure used in chapter 4. In our numerical scheme, we are required to compute derivatives of a function $f(\phi, \psi)$ whose derivatives are singular at the origin. We compute its derivatives via finite differences. In this section, we will introduce some toy examples, and discuss the relative errors that occur when attempting to compute derivatives using the function splitting method.

A.1 Errors of finite differences near a singular point

We start by considering a function of one variable, $f : [0,1] \to \Re$, which is infinitely differentiable in $(0,1]$. We will discretise the independent variable x with equally spaced points, and denote the distance between two mesh points as h. We choose h to be rational such that $1/h = N \in \mathbb{N}$. This gives us the mesh

$$x_i = h\,i, \qquad i = 1, \cdots, N. \tag{A.1}$$

We have not included a mesh point at $x = 0$, since we will not be computing the derivative at this point.

Finite difference methods can be derived by considering local expansions of f. Assuming f is infinitely differentiable at x_i, it can be expressed locally as a Taylor series, given by

$$f(x) = f(x_i) + f'(x_i)\,(x - x_i) + f''(x_i)\frac{1}{2}\,(x - x_i)^2 + \cdots \;, \tag{A.2}$$

where $f^{(n)} = d^n f/dx^n$. Let us first assume that $f(x)$ and all of its derivatives are of $O((x - x_i)^\alpha)$, $\alpha \geq 0$ near $x = x_i$. We may wish to approximate $f(x)$ by truncating the above series after some finite number of terms. For example, evaluating (A.2) at x_{i+1}, and using that $x_{i+1} - x_i = h$, we may write

$$f(x_{i+1}) = f(x_i) + hf'(x_i) + \frac{h^2}{2} f''(x_i) + O(h^3). \tag{A.3}$$

This offers us a way to numerically approximate a function with a finite order polynomial in h. The order of accuracy of the approximation (A.3) is third order, meaning the local truncation error is of $O(h^3)$. If we also evaluate equation (A.2) at x_{i-1}, one can show that

$$f'(x_i) = \frac{f(x_{i+1}) - f(x_{i-1})}{2h} + \frac{1}{6} f'''(x_i)h^2 + \cdots \tag{A.4}$$

Therefore, one can write

$$\begin{aligned} f'(x_i) &= \frac{f(x_{i+1}) - f(x_{i-1})}{2h} + O(h^2) && \text{(A.5)} \\ &= \delta_x f(x_i) + O(h^2) && \text{(A.6)} \end{aligned}$$

The discrete operator δ_x is a second order accurate approximation to the derivative of f at x_i. As we decrease h, the difference between the true value of the derivative and the approximation will decrease, up until a point where rounding errors become the main source of error (using double precision, these errors are of $O(|f(x_i)|\ 2^{-53}/h)$). In general, a discrete operator that is an $O(h^n)$ accurate approximation of f' can be written in the form

$$f'(x_i) = \delta_x f(x_i) + Ah^n f^{(n+1)}(x_i) + Bh^{n+1} f^{(n+2)}(x_i) + \cdots, \tag{A.7}$$

where A and B are constants. We define the piecewise absolute error E_i^{abs} as

$$E_i^{\text{abs}} = |f'(x_i) - \delta_x f(x_i)|. \tag{A.8}$$

We can see that for an n order accurate finite difference scheme, $E_i^{\text{abs}} = O(h^n)$. When considering the errors of a derivative that is singular, it will be more meaningful to consider the piecewise relative error E_i, given by

$$E_i = \frac{|f'(x_i) - \delta_x f(x_i)|}{f'(x_i)}. \tag{A.9}$$

If $f'(x_i) = O(1)$, an n order accurate finite difference scheme gives $E_i = O(h^n)$. However, if $f'(x_i) = O(h^\alpha)$, $\alpha > 0$, then we find that $E_i = O(h^{n-\alpha})$. When considering approximations of a derivative which is small near $x = x_i$, it is best to instead consider the absolute error (A.8). As an example, using the forward Euler scheme ($n = 1$) on the function $f(x) = \sin(x)$, for $x = O(h)$, we find $E_i^{\text{abs}} = O(h)$ and $E_i = O(1)$. This can be read as the absolute error is of the order of the derivative, which is itself small.

We note here that if $f \sim x^p$ for $x = O(h)$, where $p \in \mathbb{N} \equiv \{0, 1, \cdots\}$, if we approximate the derivative of f using an n order difference scheme, we find that if $n < p$, then near $x = 0$

$$f'(x_i) = \delta_x f(x_i) + O(h^{p-1}). \tag{A.10}$$

This comes from the fact that the coefficients of the first $p - 1$ terms in the local representation (A.2) of f at $x = 0$ are zero.

In the above derivation, we assumed that f and all of its derivatives are finite near x_i. Let us now consider the situation where some or all of the derivatives of f are singular at a given value of x. Without loss of generality, let us assume this occurs at $x = 0$. Using the mesh (A.1), we want to see the orders of errors that occur in approximating f' with polynomials at the first few mesh point, when $x = O(h)$.

Consider a function f where $m \in \mathbb{N}$ is the smallest value of m such that $f^{(m)}$ is singular at $x = 0$. Near $x = 0$, let $f^{(m)}$ have the leading order behaviour $f^{(m)} \sim x^{p-m}$, where $p \in \Re \backslash \mathbb{N}$. This term will appear as x^p in the local expansion of f. This motivates the choice of p, since if $p \in \mathbb{N}$, the term will not be a singularity of $f^{(m)}$. We will assume that the leading order behaviour of f is $f \sim x^p$. This does not have to be the case, but when it is not true, the function splitting method experiences problems when approximating the constant in the term χ, as shown in the following section. It follows that $f^{(n+1)} \sim x^{p-n-1}$. We will also ignore more complicated singularities like $\log(x)$ for simplicity. Consider a finite difference approximation (A.7) with order of accuracy n. If $n + 1 \geq m$, we have

$$f'(x_i) = \delta_x f(x_i) + \underbrace{Ah^n f^{(n+1)}(x_i)}_{O(h^{p-1})} + \underbrace{Bh^{n+1} f^{(n+2)}(x_i)}_{O(h^{p-1})} + \cdots \tag{A.11}$$

$$= \delta_x f(x_i) + O(h^{p-1}) \tag{A.12}$$

where we have made use of the fact that $f^{(n+1)} \sim x^{p-n-1}$. If $n+1 < m$, we have that

$$f'(x_i) = \delta_x f(x_i) + \underbrace{Ah^n f^{(n+1)}(x_i)}_{O(h^{p-1})} + \cdots + \underbrace{Ch^m f^{(m+1)}(x_i)}_{O(h^{p-1})} + \cdots \tag{A.13}$$

$$= \delta_x f(x_i) + O(h^{p-1}) \tag{A.14}$$

From equations (A.12) and (A.14), since $f'(x_i) = O(h^{p-1})$, we can see that, given

$f \sim x^p$, where $p \in \Re \backslash \mathbb{N}$, the order of the local truncation error is equivalent to that of the derivative itself, and is independent of the finite difference scheme used! This is true even if the term $f^{(m)}(x_i)$ is not included in the coefficients used to approximate the polynomials within the derivation of the finite difference scheme (i.e. $n+1 < m$). Applying equation (A.12) to (A.8) and (A.9), we find that $E_1^{abs} = O(h^{p-1})$ and $E_1 = O(1)$. This is particularly problematic if $p < 1$: we have a large absolute error, of the same order as the derivative itself. We will illustrate the above with a couple of examples.

Let us define two functions, f_1 and f_2, as

$$f_1(x) = x^{-2}\left(1+\sin(x)\right) \sim x^{-2} \qquad f_1'(x) \sim x^{-3}, \tag{A.15}$$

$$f_2(x) = x^{5/2}\cos(x^2) \sim x^{5/2} \qquad f_2'(x) \sim x^{3/2}. \tag{A.16}$$

We will compute the derivatives of these functions at the point x_1 using first, second, and third order forward finite difference schemes. The first function, f_1, is singular at $x = 0$. Therefore, in the above notation, we have that $m = 0$ and $p = -2$. The first ($n = 1$), second ($n = 2$) and third ($n = 3$) order finite differences all have errors of $O(h^{-3})$. This is shown in figure A.1(a), where a log-log plot E_1^{abs} (the absolute error at $x = x_1 = h$) against h is shown. The curves for the $n = 1$ (black), $n = 2$ (dashed) and $n = 3$ (dotted) schemes all have gradients of -3. Meanwhile, the function f_2 is not singular at $x = 0$, but its third derivative is ($m = 3$). Therefore, the $n = 1$ difference scheme satisfies $n + 1 < 3$, while the $n = 2$ and $n = 3$ schemes satisfy $n + 1 \geq 3$. Despite this, all of the difference schemes have an order of error of $O(h^{3/2})$, as shown in log-log plot of figure A.1(b). These results are in agreement with equations (A.12) and (A.14).

In the following section, we will describe the function splitting procedure, and how it can improve the accuracy a finite difference scheme near a singularity.

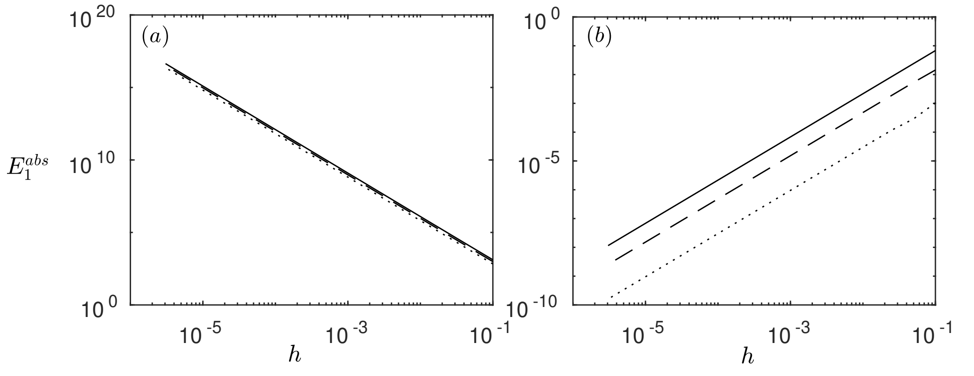

Figure A.1: Log-log plot of the mesh spacing h against the E_1^{abs} for a $n = 1$ (solid curve), $n = 2$ (dashed) and $n = 3$ (dotted) forward difference scheme. Figure (a) is for f_1 , and figure (b) is f_2 (see equations (A.15) and (A.16)).

A.2 Function splitting method

So far we have discussed the errors associated with approximating a derivative near a singular point with finite differences. Throughout this section, let m again refer to the lowest order derivative of f which is singular at $x = 0$, and $p \in \Re\backslash\mathbb{N}$ be such that $f^{(m)} \sim x^{p-m}$ near $x = 0$. In chapter 4, we propose regulating the singularity by adding and subtracting a function $\chi(x)$, given by

$$\chi(x) = Bx^p. \tag{A.17}$$

We will repeat the method for clarity. The function f can be written as

$$f(x) = f(x) - \chi(x) + \chi(x). \tag{A.18}$$

We approximate the derivative of f at a point x_i as

$$f'(x_i) \approx \underbrace{\delta_x \left(f(x_i) - \chi(x_i)\right) + \chi'(x_i)}_{\bar{\delta_x}(f(x_i))}. \tag{A.19}$$

We denote the operation on the right hand side as $\bar{\delta_x}$. The motivation is that the m^{th} derivative of the function $(f(x) - \chi(x))$ no longer has the leading order singularity at $x = 0$, and hence inaccuracies of the numerical approximations of this function could potentially be avoided. When applied to the full numerical scheme of chapter 4, the function $\chi(x)$ will have a free constant B (see equation (4.20)). In the analytic examples that follow, one could find B exactly, by considering the local expansions of f about $x = 0$. However, we will approximate this constant the same way as done in chapter 4, by matching $\chi(x)$ to $f(x)$ at the first meshpoint past the singularity:

$$\chi(x_1) = f(x_1). \tag{A.20}$$

The question we shall answer is what is the order of E_1 when using the approximation (A.19). Noting equation (A.12), when computing finite difference approximations directly (replacing $\bar{\delta_x}$ with δ_x in equation (A.9)), we have that $E = O(1)$ when $x = O(h)$.

We believe it best to summarise the conclusion of this section, before preceding to demonstrate some examples. For simplicity, we shall assume that f has the form

$$f(x) = \widehat{B}x^p + Cx^q + O(x^r), \tag{A.21}$$

near $x = 0$, where $p < q < r$, $p \in \Re \backslash \mathbb{N}$, and $\widehat{B}$ and C are real constants. It could be that there exist more complicated terms (for example, $x^q \log x$), and the results for this section can be modified to include such behaviours. Following the function splitting method, we write

$$\chi(x) = Bx^p. \tag{A.22}$$

We found that $E_1 = O(h^{p-q})$. The sources of the error are from the approximation of the constant B in equation (A.22), and the application of δ_x to the term Cx^q in equation (A.21), both of which produce errors like $E_1 = O(h^{p-q})$. We can see from equation (A.21) that the 'true' value of B should be $\widehat{B}$ (the coefficient of the leading order term). However, in chapter 4, we must approximate B, since the solution is not known analytically a priori. We match the function χ to our numerical solution using equation (A.20). Substituting (A.22) and (A.21) into (A.20) gives

$$B = \widehat{B} + O(h^{q-p}). \tag{A.23}$$

We see that there is an $O(h^{q-p})$ error in evaluating the constant B. Equation (A.17) implies we must consider functions f that have the leading order behaviour $f \sim x^p$, or else the errors in the approximation of B become too large. This can be seen by considering equation (A.23) with $q < p$.

We shall demonstrate how this applies to some example functions, but first we provide some justification as to why this is the case. Differentiating (A.21), we find that

$$f'(x) = p\widehat{B}x^{p-1} + qCx^{q-1} + O(x^{r-1}). \tag{A.24}$$

Following the function splitting method, we write

$$\chi(x) = Bx^p, \qquad B = \widehat{B} + O(h^\delta). \tag{A.25}$$

Substituting the above into equation (A.19), we find that

$$\bar{\delta_x} f(x_i) = \delta_x \left(\widehat{B}x^p + Cx^q + O(x^r) - \left(\widehat{B} + O(h^\delta) \right) x^p \right) + \chi'(x_i). \tag{A.26}$$

Re-arranging, and making use of (A.25), one finds

$$\bar{\delta_x} f(x_i) = \delta_x \left(Cx^q + O(x^r) - O(h^\delta)x^p \right) + p\widehat{B}x^{p-1} + px^{p-1}O(h^\delta). \tag{A.27}$$

We must find the error that occurs when applying δ_x to the first term in the brackets.

In general, we shall write

$$\delta_x\left(Cx^q\right) = Cqx^{q-1} + O(h^\alpha). \tag{A.28}$$

First, consider the case when $q \in \Re\backslash\mathbb{N}$. Equation (A.12) tells us that $\alpha = q-1$. Meanwhile, if $q \in \mathbb{N}$, we have that the error in the finite difference approximation is the order of the difference scheme if $n > q$ (i.e. $\alpha = n$), or alternatively we get $\alpha = q-1$ if $n < q$ (see equation (A.10)). Substituting (A.28) into equation (A.27), and using $x = O(h)$, we find

$$\begin{aligned}\bar{\delta_x}(x_i) &= p\widehat{B}x^{p-1} + qCx^{q-1} + O(h^\alpha) + O(h^{\delta+p-1}) \\ &= \frac{df}{dx}(x_i) + O(h^\alpha) + O(h^{\delta+p-1}),\end{aligned} \tag{A.29}$$

where we made use of equation (A.24). Substituting equation (A.29) into equation (A.9), and using that $f'(x) = O(h^{p-1})$ gives

$$E_1 = \frac{O(h^\alpha) + O(h^{\delta+p-1})}{f'(x_i)} = O(h^{\alpha+1-p}) + O(h^\delta). \tag{A.30}$$

This provides a bound on E_1. Hence, we find that

$$E_1 = \begin{cases} O(h^{\min(q-p,\delta)}), & q \in \Re\backslash\mathbb{N}, \quad \text{(A.31)} \\ O(h^{\min(n+1-p,\delta)}), & q \in \mathbb{N},\, n > q\ , \quad \text{(A.32)} \\ O(h^{\min(q-p,\delta)}), & q \in \mathbb{N},\, n < q\ . \quad \text{(A.33)} \end{cases}$$

When approximating B via equation (A.20), we have shown in equation (A.23) that $\delta = q - p$. Hence, equations (A.31-A.33) reduce to

$$E_1 = O(h^{q-p}). \tag{A.34}$$

It is worth noting that when we are not near $x = 0$, the approximation $\bar{\delta_x}$ is as accurate as δ_x. This can be shown by considering

$$\bar{\delta_x} = \delta_x f + \left[\frac{d\chi}{dx}(x_i) - \delta_x \chi\right] \tag{A.35}$$

$$= \frac{df}{dx}(x_i) + O(h^n) + \left[\frac{d\chi}{dx}(x_i) - \frac{d\chi}{dx}(x_i) - O(h^n)\right] \tag{A.36}$$

$$= \frac{df}{dx}(x_i) + O(h^n). \tag{A.37}$$

In this sense, the 'correction' to the operator δ_x has errors of $O(h^n)$ when not near the singularity. The correction terms is only important near the singularity.

Let us demonstrate with some examples. Consider again the function from equation (A.15), and its corresponding χ,

$$f(x) = \frac{1 + \sin x}{x^2} \sim \frac{1}{x^2} + \frac{1}{x} + \cdots, \qquad \chi(x) = \frac{B}{x^2}. \tag{A.38}$$

Comparing equations (A.38) and (A.21), we find that $p = -2$ and $q = -1$. Hence, from equation (A.34), we expect E_1 to be no better than $O(h)$. Figure A.2 shows a log-log plot of E_1 against h for a first order ($n = 1$) and second order ($n = 2$) approximation, given by the solid and dashed curves respectively. Both have a gradient of one, as expected. As a further test on our analysis, we place an artificial error on the value B of $O(h^{1/2})$, which is equivalent to changing δ in equation (A.31) to 1/2. We find that the order of E_1 is reduced to $O(h^{1/2})$, and this is shown by the dotted curve in figure A.2.

As a second example, consider

$$f = x^{1/4} + x^3 I_0(x) \sim x^{1/4} + x^3 + \cdots, \qquad \chi(x) = Bx^{1/4}, \tag{A.39}$$

where I_0 is the modified Bessel function of the first kind of order zero. In our notation, this is equivalent to $p = 1/4$ and $q = 3$. Figure A.3 shows a log-log plot

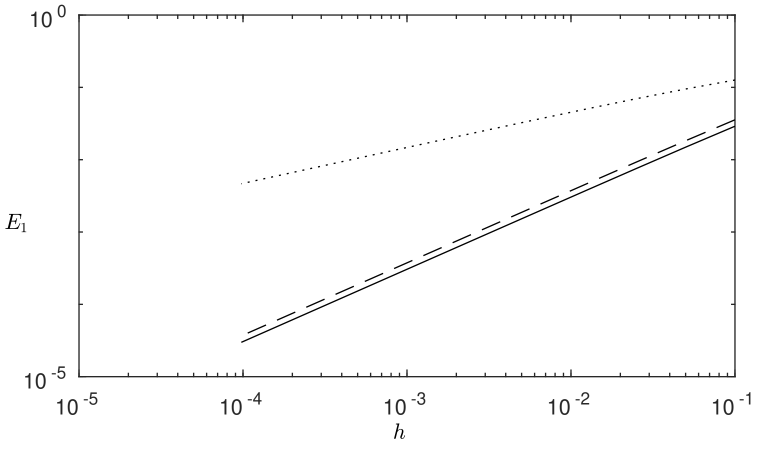

Curve	Gradient
Solid	0.9999
Dashed	0.9999
Dotted	0.4967

Figure A.2: Log-log plot of E_1 against h for the function (A.38). The solid and dashed curve are for $n = 1$ and $n = 2$ respectively. The dotted curve is for $n = 1$ and has an artificial error of $O(h^{1/2})$ applied to the approximation of B. The gradient between the penultimate two points of each curve, $h = 2^{-9}/10$ and $h = 2^{-8}/10$, is shown in the table.

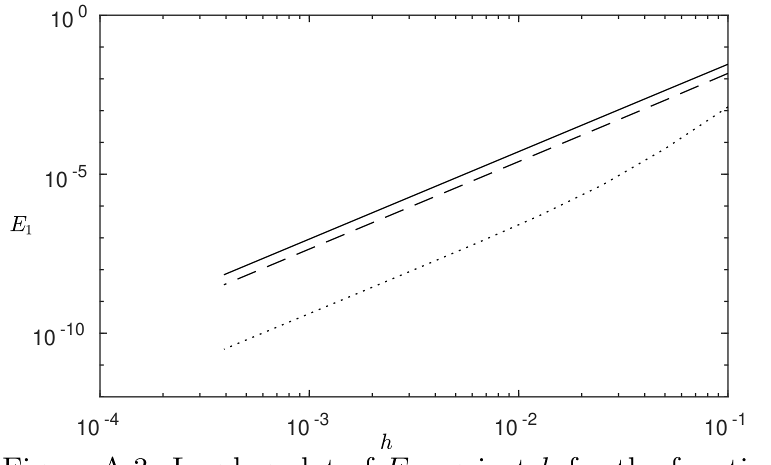

Curve	Gradient
Solid	2.7500
Dashed	2.7500
Dotted	2.7523

Figure A.3: Log-log plot of E_1 against h for the function (A.39). The solid, dashed and dotted curves are for $n = 1$, $n = 2$ and $n = 3$ respectively.

of E_1 against h for first (solid curve), second (dashed) and third (dotted) difference equations. Equation (A.32) predicts the gradient of these curves should be 11/4, which agrees with the curves seen in the figure. We note here that the results of the appendix can be trivially extended to higher order derivatives. The same bounds on the relative error are seen. In the following paragraphs, we will explain how this relates to the numerical method of chapter 4.

Finite difference methods can be extended to multivariable functions by considering multivariable Taylor series. The extension of the theory in this appendix to multivariable functions is less clear. Consider the function $\chi(\phi, \psi)$ used in chapter

4, given by equation (4.20). After some algebra, one finds that the local behaviour of χ near $\phi = 0$ is given by

$$\chi(\phi, \psi) = \frac{1}{B^{2/3}} 2^{1/3} \psi^{2/3} + \frac{2}{3B}\phi + \frac{2^{5/3}}{9\psi^{2/3}}\phi^2 + O(\phi^3). \tag{A.40}$$

However, to obtain such an expansion, one must assume that ψ is not a small parameter. This can be seen by the fact that the local expansion is not valid in the limit as $\psi \to 0$. Hence, the nature of the singularity at the origin is more complicated: we can consider different limits due to the existence of two variables. For example, taking $\epsilon << 1$, we could take $\psi = \phi = \epsilon$, or alternatively $\psi = \phi^2 = \epsilon$. This denies the ability to discuss local behaviour of the form (A.21), upon which the results of this section depend upon.

This may paint a very pessimistic picture. However, the order of the relative errors near the singularity are not crucial to know, as long as they are given by $O(h^\alpha)$ and $O(k^\beta)$ for some $\alpha > 0$ and $\beta > 0$. As discussed in section 4.4, it appears that the numerical method is slightly worse than first order accurate in h. This can be seen in figure 4.11, where the relative error of the value of B is shown for a two-dimensional bubble. The numerical scheme appears to be between first and second order accurate in k, as shown in 4.12.

The author acknowledges that the analysis contained within the appendix may seem out of place, given that it cannot be neatly applied to the numerical scheme of chapter 4. However, although some authors have used similar techniques for finite difference methods (Ames [5], Brennen [16], Brennen [17], Woods [95]), the author has not seen analysis of the type presented in this appendix. The analysis itself is relatively heuristic, lacking the proper rigor of numerical analysis, but the agreement of the theory with tested functions provides evidence that the results are correct. It would be of interest to see if the theory can be extended to higher dimensions. At the very least, the theory demonstrates that the function splitting method, and the approximation of the constant B, has an effect on the accuracy of finite difference approximations.

Bibliography

[1] M. Abramowitz and I. A. Stegun. *Handbook of mathematical functions: with formulas, graphs, and mathematical tables*, volume 55. Courier Corporation, 1965.

[2] Advanpix. Multiprecision computing toolbox for matlab, 2017. URL `http://www.advanpix.com/`.

[3] B. F. Akers, D. M. Ambrose, K. Pond, and J. D. Wright. Overturned internal capillary–gravity waves. *Eur. J. Mech. B*, 57:143–151, 2016.

[4] T. R. Akylas. Envelope solitons with stationary crests. *Phys. Fluids A*, 5(4):789–791, 1993.

[5] W. F. Ames. *Numerical methods for partial differential equations.* Academic press, 2014.

[6] V. I. Arkhipenko, Y. D. Barkov, V. G. Bashtovoi, and M. S. Krakov. Investigation into the stability of a stationary cylindrical column of magnetizable liquid. *Fluid Dyn.*, 15(4):477–481, 1980.

[7] G. Artana, H. Romat, and G. Touchard. Theoretical analysis of linear stability of electrified jets flowing at high velocity inside a coaxial electrode. *J. Electrostatics*, 43(2):83–100, 1998.

[8] V. G. Bashtovoi and M. S. Krakov. Stability of an axisymmetric jet of magnetizable fluid. *J. App. Mech. Tech. Phys.*, 19(4):541–545, 1978.

[9] G. K. Batchelor. *An introduction to fluid dynamics*. Cambridge university press, 1994.

[10] T. B. Benjamin. The solitary wave with surface tension. *Q. Appl. Maths*, 40(2): 231–234, 1982.

[11] G. Birkhoff and D. Carter. Rising plane bubbles. *J. Math. Mech.*, pages 769–779, 1957.

[12] G. Birkhoff and E. H. Zarantonello. *Jets, Wake and Cavities*. Academic Press, New York, 1957.

[13] M. G. Blyth and E. I. Părău. Solitary waves on a ferrofluid jet. *J. Fluid Mech.*, 750:401–420, 2014.

[14] W. A. Bonner, H. R. Hulett, R. G. Sweet, and L. A. Herzenberg. Fluorescence activated cell sorting. *Rev. Sc. Instruments*, 43(3):404–409, 1972.

[15] E. Bourdin, J. C. Bacri, and E. Falcon. Observation of axisymmetric solitary waves on the surface of a ferrofluid. *Phys. Rev. Lett.*, 104(9):094502, 2010.

[16] C. Brennen. *Cavitation and Other Free Surface Phenomena*. PhD thesis, Oxford University, 1966.

[17] C. Brennen. A numerical solution of axisymmetric cavity flows. *J. Fluid Mech.*, 37(04):671–688, 1969.

[18] C. L. Burcham and D. A. Saville. The electrohydrodynamic stability of a liquid bridge: microgravity experiments on a bridge suspended in a dielectric gas. *J. Fluid Mech.*, 405:37–56, 2000.

[19] J. G. B. Byatt-Smith and M. S. Longuet-Higgins. On the speed and profile of steep solitary waves. *Proc. R. Soc. Lond. A*, 350(1661):175–189, 1976.

[20] A. R. Champneys, J.-M. Vanden-Broeck, and G. J. Lord. Do true elevation gravity–capillary solitary waves exist? A numerical investigation. *J. Fluid Mech.*, 454:403–417, 2002.

[21] P. Christodoulides and F. Dias. Impact of a falling jet. *J. Fluid Mech*, 657: 22–35, 2010.

[22] R. Collins. A simple model of the plane gas bubble in a finite liquid. *J. Fluid Mech.*, 22(04):763–771, 1965.

[23] G. D. Crapper. An exact solution for progressive capillary waves of arbitrary amplitude. *J. Fluid Mech.*, 2(6):532–540, 1957.

[24] J. M. Crowley. Electrohydrodynamic droplet generators. *J. Electrostatics*, 14 (2):121–134, 1983.

[25] P. Daripa. The fastest smooth Taylor bubble. *App. Num. Math.*, 34(4):373–379, 2000.

[26] R. M. Davies and G. Taylor. The mechanics of large bubbles rising through extended liquids and through liquids in tubes. *Proc. R. Soc. Lond. A*, 200 (1062):375–390, 1950.

[27] F. Dias and C. Kharif. Nonlinear gravity and capillary-gravity waves. *Annu. Rev. Fluid Mech.*, 31(1):301–346, 1999.

[28] F. Dias and J.-M. Vanden-Broeck. Flows emerging from a nozzle and falling under gravity. *J. Fluid Mech.*, 213:465–477, 1990.

[29] F. Dias and J.-M. Vanden-Broeck. Potential-flow studies of steady two-dimensional jets, waterfalls, weirs and sprays. *J. Eng. Math.*, 70(1-3):165–174, 2011.

[30] F. Dias, D. Menace, and J. M. Vanden-Broeck. Numerical study of capillary-gravity solitary waves. *Eur. J. Mech.*, 15:1736, 1996.

[31] A. Doak and J.-M. Vanden-Broeck. Solitary gravity waves and free surface flows past a point vortex. *IMA J. App. Math.*, 82(4):821–835, 2017.

[32] A. Doak and J.-M. Vanden-Broeck. Solution selection of axisymmetric Taylor bubbles. *J. Fluid Mech.*, 843:518–535, 2018.

[33] A. Doak and J.-M. Vanden-Broeck. Travelling wave solutions on an axisymmetric ferrofluid jet. *J. Fluid Mech.*, 865:414–439, 2019.

[34] D. T. Dumitrescu. Strömung an einer luftblase im senkrechten rohr. *ZAMM-Journal of Applied Mathematics and Mechanics/Zeitschrift für Angewandte Mathematik und Mechanik*, 23(3):139–149, 1943.

[35] C. V. Easwaran. Solitary waves on a conducting fluid layer. *Phy. Fluids*, 31 (11):3442–3443, 1988.

[36] J. Eggers and A. F. Smith. Free streamline flows with singularities. *J. Fluid Mech.*, 647:187–200, 2010.

[37] T. Gao and J.-M. Vanden-Broeck. Numerical studies of two-dimensional hydroelastic periodic and generalised solitary waves. *Phys. Fluids*, 26(8):087101, 2014.

[38] T. Gao, Z. Wang, and J.-M. Vanden-Broeck. Investigation of symmetry breaking in periodic gravity–capillary waves. *J. Fluid Mech.*, 811:622–641, 2017.

[39] T. Gao, P. A. Milewski, D. T. Papageorgiou, and J.-M. Vanden-Broeck. Dynamics of fully nonlinear capillary–gravity solitary waves under normal electric fields. *J. Eng. Math.*, 108(1):107–122, 2018.

[40] T. Gao, A. Doak, J.-M. Vanden-Broeck, and Z. Wang. Dynamics of fully nonlinear capillary–gravity solitary waves under normal electric fields. *Eur. J. Mech. B (accepted)*, 2019.

[41] P. R. Garabedian. On steady-state bubbles generated by Taylor instability. *Proc. R. Soc. Lond. A*, 241(1226):423–431, 1957.

[42] P. R. Garabedian. A remark about pointed bubbles. *Comm. Pure App. Math.*, 38(5):609–612, 1985.

[43] H. Gleeson, P. Hammerton, D. T. Papageorgiou, and J.-M. Vanden-Broeck. A new application of the Korteweg–de Vries Benjamin-Ono equation in interfacial electrohydrodynamics. *Phy. Fluids*, 19(3):031703, 2007.

[44] S. Grandison, J.-M. Vanden-Broeck, D. T. Papageorgiou, T. Miloh, and B. Spivak. Axisymmetric waves in electrohydrodynamic flows. *J. Eng. Math.*, 62(2): 133–148, 2008.

[45] M. Groves and D. Nilsson. Spatial dynamics methods for solitary waves on a ferrofluid jet. *J. Math. Fluid Mech.*, pages 1–32, 2018.

[46] M. I. Gurevich. *The theory of jets in an ideal fluid*, volume 93. Pergamon, 1966.

[47] P. Guyenne and E. I. Părău. An operator expansion method for computing nonlinear surface waves on a ferrofluid jet. *J. of Comp. Phys.*, 321:414–434, 2016.

[48] B. Hopkinson. On discontinuous fluid motions involving sources and vortices. *Proc. Lond. Math. S.*, 1(1):142–164, 1897.

[49] M. J. Hunt and J.-M. Vanden-Broeck. A study of the effects of electric field on two-dimensional inviscid nonlinear free surface flows generated by moving disturbances. *J. Eng. Math.*, 92(1):1–13, 2015.

[50] J. K. Hunter and J.-M. Vanden-Broeck. Solitary and periodic gravity–capillary waves of finite amplitude. *J. Fluid Mech.*, 134:205–219, 1983.

[51] R. W. Jeppson. Axisymmetric seepage through homogeneous and nonhomogeneous porous mediums. *Water Resourses Res.*, 4(6):1277–1288, 1968.

[52] R. W. Jeppson. Inverse formulation and finite difference solution for flow from a circular orifice. *J. Fluid Mech*, 40(01):215–223, 1970.

[53] W. Kinnersley. Exact large amplitude capillary waves on sheets of fluid. *J. Fluid Mech.*, 77(2):229–241, 1976.

[54] G. Kirchhoff. Zur theorie freier flüssigkeitsstrahlen. *J. für die reine und angewandte Mathematik*, 70:289–298, 1869.

[55] D. J. Korteweg and G. de Vries. On the change of form of long waves advancing in a rectangular channel, and a new type of long stationary wave. *Phil. Mag*, 39:422–443, 1895.

[56] O. Laget and F. Dias. Numerical computation of capillary–gravity interfacial solitary waves. *J. Fluid Mech.*, 349:221–251, 1997.

[57] H. Levine and Y. Yang. A rising bubble in a tube. *Phys. Fluids A*, 2(4):542–546, 1990.

[58] A. E. H. Love. On the theory of discontinuous fluid motions in two dimensions. Cambridge Philosophical Society, 1891.

[59] E. Mackenroth. Application of inverse mapping technique for the solution of the ideal axisymmetric impinging jet problem. Master's thesis, 1968.

[60] C. C. Maneri and N. Zuber. An experimental study of plane bubbles rising at inclination. *Int. J. of Multiphase Flow*, 1(5):623–645, 1974.

[61] J. W. McLean and P. G. Saffman. The effect of surface tension on the shape of fingers in a Hele–Shaw cell. *J. Fluid Mech.*, 102:455–469, 1981.

[62] J. R. Melcher. *Field-coupled surface waves: Comparative study of surface-coupled electrohydrodynamic and magnetohydrodynamic systems.* MIT, Cambridge, MA, 1963.

[63] P. Milewski, J. M. Vanden-Broeck, and J. B. Keller. Singularities on free surfaces of fluid flows. *Studies App. Math.*, 100(3):245–267, 1998.

[64] V. Modi. Comment on bubbles rising in a tube and jets falling from a nozzle. *Phys. Fluids*, 28(11):3432–3433, 1985.

[65] D. T. Papageorgiou. Film flows in the presence of electric fields. *Ann. Rev. F. Mech.*, 51:155–187, 2019.

[66] D. T. Papageorgiou and J.-M. Vanden-Broeck. Numerical and analytical studies of non-linear gravity–capillary waves in fluid layers under normal electric fields. *IMA J. App. Math.*, 72(6):832–853, 2006.

[67] D. T. Papageorgiou, P. G. Petropoulos, and J.-M. Vanden-Broeck. Gravity capillary waves in fluid layers under normal electric fields. *Phy. Rev. E*, 72(5): 051601, 2005.

[68] T. L. Perelman, A. K. Fridman, and M. M. Eliashevich. Modified Korteweg-de Vries equation in electrohydrodynamics. *Zhurnal Eksperimental'noi i Teoreticheskoi Fiziki*, 66:1316–1323, 1974.

[69] M. Planck. Zur theorie der flüssigkeitsstrahlen. *Annalen der Physik*, 257(3): 499–509, 1884.

[70] J. Plateau. Statique expérimentale et théorique des liquides soumis aux seules forces moléculaires. *Acad. Sci. Bruxelles Mem.*, 23(5), 1849.

[71] K. Raj, B. Moskowitz, and R. Casciari. Advances in ferrofluid technology. *J. Magn. Magn. Mater.*, 149(1-2):174–180, 1995.

[72] D. Rannacher and A. Engel. Cylindrical Korteweg–de Vries solitons on a ferrofluid surface. *New J. Phys.*, 8(6):108, 2006.

[73] J. W. S. Rayleigh. On the instability of jets. *Proc. Lond. Math. Soc.*, 10:4–13, 1878.

[74] R. E. Rosensweig. *Ferrohydrodynamics*. Dover, 1985.

[75] J. M. Schneider, N. R. Lindblad, C. D. Hendricks, and J. M. Crowley. Stability of an electrified liquid jet. *J. App. Phy.*, 38(6):2599–2605, 1967.

[76] E. R. Setiawan and S. D. Heister. Nonlinear modeling of an infinite electrified jet. *J. Electrostatics*, 42(3):243–257, 1997.

[77] R. V. Southwell. *Relaxation methods in theoretical physics*. Oxford Clarendon Press, 1946.

[78] G. G. Stokes. On the theory of oscillatory waves. *Trans. Camb. Phil. Soc.*, 8, 01 1847.

[79] S. Turenne and M. Fiset. Modeling of abrasive particle trajectories during erosion by a slurry jet. *Wear*, 162:679–687, 1993.

[80] J. M. Vanden-Broeck. Bubbles rising in a tube and jets falling from a nozzle. *Phys. Fluids*, 27(5):1090–1093, 1984a.

[81] J.-M. Vanden-Broeck. Rising bubbles in a two-dimensional tube with surface tension. *Phys. Fluids*, 27(11):2604–2607, 1984b.

[82] J.-M. Vanden-Broeck. Pointed bubbles rising in a two-dimensional tube. *Phys. Fluids*, 29:1343–1344, 1986.

[83] J.-M. Vanden-Broeck. Axisymmetric jet falling from a vertical nozzle and bubble rising in a tube of circular cross section. *Phys. Fluids A*, 3(2):258–262, 1991.

[84] J. M. Vanden-Broeck. Elevation solitary waves with surface tension. *Phys. Fluids A*, 3(11):2659–2663, 1991.

[85] J.-M. Vanden-Broeck. Rising bubble in a two-dimensional tube: Asymptotic behavior for small values of the surface tension. *Phys. Fluids A*, 4(11):2332–2334, 1992.

[86] J.-M. Vanden-Broeck. Two-dimensional jet aimed vertically upwards. *ANZIAM J.*, 34(4):393–400, 1993.

[87] J.-M. Vanden-Broeck. *Gravity-capillary free-surface flows.* Cambridge University Press, 2010.

[88] J.-M. Vanden-Broeck and F. Dias. Gravity-capillary solitary waves in water of infinite depth and related free-surface flows. *J. Fluid Mech.*, 240:549–557, 1992.

[89] J.-M. Vanden-Broeck and J. B. Keller. A new family of capillary waves. *J. Fluid Mech.*, 98(1):161–169, 1980.

[90] J. M. Vanden-Broeck, T. Miloh, and B. Spivack. Axisymmetric capillary waves. *Wave motion*, 27(3):245–256, 1998.

[91] F. Viana, R. Pardo, R. Yanez, J. L. Trallero, and D. D. Joseph. Universal correlation for the rise velocity of long gas bubbles in round pipes. *J. Fluid Mech.*, 494:379–398, 2003.

[92] Q. Wang, D. T. Papageorgiou, and J.-M. Vanden-Broeck. Korteweg–de Vries solitons on electrified liquid jets. *Phy. Rev. E*, 91(6):063012, 2015.

[93] J. R. Wilton. Lxxii. on ripples. *The London, Edinburgh, Dublin Phil. Mag. J. Science*, 29(173):688–700, 1915.

[94] L. C. Woods. A new relaxation treatment of flow with axial symmetry. *Q. J. Mech. Appl. Maths*, 4(3):358–370, 1951.

[95] L. C. Woods. The relaxation treatment of singular points in Poisson's equation. *Q. J. Mech. Appl. Maths*, 6(2):163–185, 1953.

[96] N. Y. Zhukovsky. Über die konturen der tragflächen der drachenflieger. *Zeitschrift für Flugtechnik und Motorluftschiffahrt*, 1:281–284, 1910.

[97] E. E. Zukoski. Influence of viscosity, surface tension, and inclination angle on motion of long bubbles in closed tubes. *J. Fluid Mech.*, 25(04):821–837, 1966.